On Aspects of Magnetic Signature Source Modelling using Near-Field Measurements

Using Multipolar Bases and Bayesian Inference on Complex Ship Geometries

Odessa Schokker

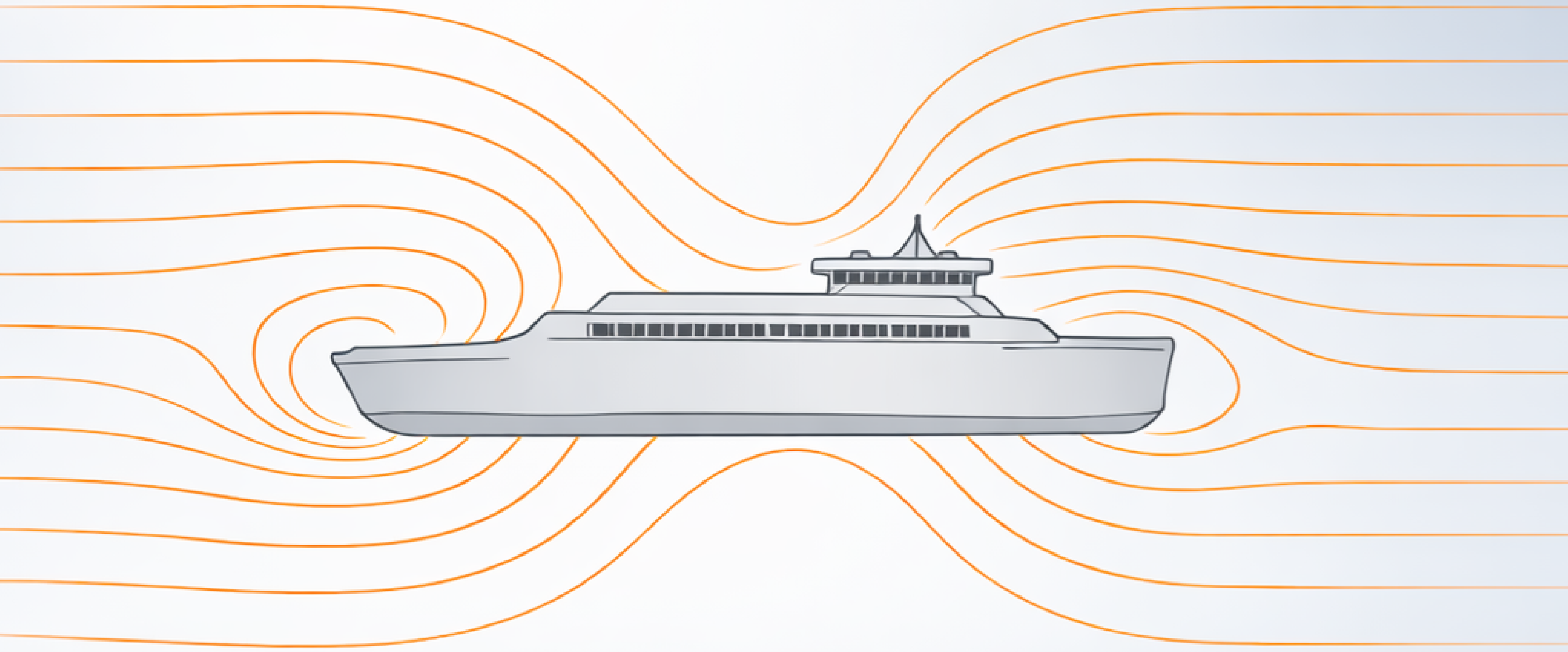

On Aspects of Magnetic Signature Source Modelling using Near-Field Measurements

Using Multipolar Bases and Bayesian Inference on Complex Ship Geometries

by

Odessa Schokker

Project Duration:	July 21, 2025 - March 27, 2026
Supervisors:	Dr. ir. J.L.A. Dubbeldam (TU Delft)
	Dr. ir. A.R.P.J. Vijn (TNO)
Thesis committee:	Dr. ir. N.V. Budko (TU Delft)

Cover: Generated with ChatGPT, modified by the author.

TU Delft

Preface

This thesis is the final product of my time at TU Delft, and with it I complete my Master's degree in Applied Mathematics. I enjoyed my studies a lot, but as I left high school in 2017, I am excited to start a job and earn some money.

First, I would like to thank my daily supervisor Aad Vijn. We met during one of my last courses, when I still had shorter hair than him. Aad had many ideas about where we could take the research, and was always enthusiastic when I came up with my own. Besides his many ideas, there was always time for a personal chat, which made TNO feel very welcoming.

I would also like to thank Johan Dubbeldam for giving me a lot of positive feedback throughout the process and helping me figure out some mathematical challenges. In the last part of my thesis, he helped me a lot by proofreading the final drafts of my chapters and pinpointing parts that needed improving.

Lastly, I would like to thank my friends and family. My mental health has gone up and down over the years of my bachelor's and master's. I always got a lot of support from my friends and family, and on top of that, the last two years have been great. I would like to start by thanking my boyfriend, who has only seen the last year of the process, but has helped me tonnes. To support me during my thesis, he cooked me many meals, gave me a lot of hugs, and asked me cool and challenging questions that got me thinking about my thesis in new ways. I would like to thank my parents and siblings for always being available for a call or meetup when I was feeling down or wanted to chill at someone else's house. Finally, I would like to thank my friends for getting me to relax through a workout at the gym, cups of tea or coffee, glasses of wine, some good and some bad movies, a few parties, and many dinners.

Odessa Schokker
Delft, March 2026

Abstract

This thesis investigates the modelling of a ship's magnetic field, by means of an equivalent source model defined on an arbitrarily shaped surface enclosing the source. This setup allows for the use of measurements close to the enclosing surface, such as on the seabed in shallow waters. A multipolar basis is introduced to reduce the dimensionality of the problem, which allows for a convenient mapping to the Decreasing Spherical Harmonic Expansion to describe the far field with low computational costs. It is found that the method performs well in determining a source model and predicting the magnetic field in new locations, provided that enough well-distributed measurements are available. The method remains accurate in the presence of noise, although measurements very close to the enclosing surface reduce performance, a reduction attributed to an approximation that may be improved.

Bayesian inference is used to stabilise the method when a low number, badly distributed and/or noisy measurements are available. We find that this regularisation indeed enables the use of the method in such situations. In addition, it is investigated whether orthogonality of the basis is required. It is found that it is not, and that a non-orthogonal basis can yield slightly better results. This suggests that the discretisation of the surface and the choice of solution space of the equivalent source are the main limiting factors in improving the solutions.

Contents

Nomenclature

Abbreviations

Abbreviation	Definition
BS	Brillouin Sphere
CD	Charge Distribution
DSHE	Decreasing Spherical Harmonic Expansion
MAP	Maximum A Posteriori
MoM	Method of Moments
NDD	Normal Dipole Distribution

Symbols

Symbol	Definition	Unit
$\mathbf{B}$	Magnetic field	T
$\mathbf{B}_0$	Background magnetic field	T
$\mathbf{B}_{\text{ind}}$	Induced magnetic field	T
$\mathbf{B}_{\text{perm}}$	Permanent magnetic field	T
$\mathbf{H}$	Auxiliary magnetic field	A/m
$\mathbf{J}$	Electric current density	A/m^2
$\mathbf{J}_b$	Bounded electric current density	A/m^2
$\mathbf{J}_f$	Free electric current density	A/m^2
$\mathbf{M}$	Magnetisation	A/m
$\mathbf{M}_{\text{ind}}$	Induced magnetisation	A/m
$\mathbf{M}_{\text{perm}}$	Permanent magnetisation	A/m
$\mathbf{m}$	Magnetic dipole moment	Am^2
G	Green's function	-
Y_k^m	Spherical Harmonic function (order k, degree m)	-
δ	Dirac Delta function	-
σ	Surface charge distribution	A/m
σ_{km}^0	Initial basis function of σ (order k, degree m)	A/m
σ_{km}	Orthonormalised or normalised version of σ_{km}^0	A/m
τ	Normal dipole distribution	A
τ_{km}^0	Initial basis function of τ (order k, degree m)	A
τ_{km}	Orthonormalised or normalised version of τ_{km}^0	A
ϕ	Scalar magnetic potential	A
χ_{e_j}	Characteristic function on the element e_j	-
α	Scaling constant of the inner product $\langle \sigma_1 \vert \sigma_2 \rangle$	-
μ_0	Vacuum magnetic permeability	Tm/A
μ_r	Relative magnetic permeability	-
σ_{meas}	Standard deviation of measurement noise	A/m
χ_m	Magnetic susceptibility	-

1

Introduction

Modern ships are largely constructed from ferromagnetic steel, which becomes magnetised in the presence of the Earth's magnetic field. This magnetisation consists of both a permanent component, originating from the construction process and onboard systems, and an induced component that depends on the ship's orientation with respect to the Earth's magnetic field. As a result, a ship generates disturbances in the surrounding magnetic field, commonly referred to as its magnetic signature.

In maritime environments, these signatures play an important role in safety and security applications. In particular, for harbour protection and monitoring of coastal infrastructure, magnetic measurements can be used to detect, classify, and track vessels and underwater drones. This makes accurate modelling and interpretation of magnetic signatures essential for reliable detection systems. Such measurements can, for example, be obtained by deploying sensor arrays on the seabed in shallow waters, such as at the entrance of major ports like the Port of Rotterdam.

In addition to the magnetic field, a ship has a signature in other measurable domains, such as acoustic signals, pressure waves, and electric fields. Acoustic signals, are the most frequently used signals for detection surveillance. In shallow waters like the ports, these signals are only usable on very short distances, due to reflections and ambient noise. Electric signals have been proposed as an alternative to detect sources in such settings [18].

To contribute to this idea, this thesis focusses on magnetic signals, by modelling the magnetic field and solving its inverse problem to find a source model for magnetic detection. Before we introduce the methods typically used for this problem, we give a bit more context on the example application.

1.1. Detection and Classification

As mentioned above, the magnetic signature of a ship can be used for detection and classification purposes. This requires solving an inverse problem based on measurements of the magnetic field. In practice, such measurements can be obtained by placing a sensor array on the seabed at the entrance of a port, perpendicular to the sailing direction, or by deploying a distributed sensor network across the seabed. When a ship passes over such an array, a large surface of measurements beneath the ship can be collected and used to solve the inverse problem.

An inverse problem with measurements on only one side of the object, is very unstable. This means that the solutions are likely to overfit on the data, resulting in bad predictions of the magnetic field in other directions. Therefore it is of importance to use a good basis to express the source and use a regularisation method, both to prevent this overfitting on the data. In shallow waters, many of the measurements will be too close to the ship to use standard modelling principles in literature. The method investigated in this thesis, solves all of these issues.

1.2. Magnetic Field Modelling Methods

There are multiple well known methods for modelling the magnetic field. Typical numerical methods are the Finite Element Method (FEM), the Method of Moments (MoM), and methods using the Decreasing Spherical Harmonic Expansion (DSHE). Finally, we introduce the method that is investigated in this thesis, an Arbitrary-Surface Harmonic Expansion. In some specific cases, analytical expressions are known.

1.2.1. Finite Element Method

The Finite Element Method is a very flexible method for computing magnetic fields. It can cope well with complex geometries and material inhomogeneity through meshing. It is also compatible with problems in which multiple domains are of importance. For example in non-static electromagnetic problems, of problems where thermal, or fluid dynamics are of importance.

One negative aspect of FEM is its high computational cost. They occur since the entire domain needs to be meshed, and the field is computed at each element (including points that we are not interested in). The resulting system that needs to be solved becomes large very quickly, though it becomes sparse as well. The size of the matrix is an issue for forward computations, but even more for inverse computations. Furthermore, the domain needs to be finite, and thus boundary conditions need to be imposed on the edges of the domain that do not occur in reality.

1.2.2. Method of Moments

In the Method of Moments [1] a magnetic material is meshed, and for each element an approximation of its magnetization is computed. This computation is based on the magnetic background field and the interaction between all elements. The approximations are built up of basis functions, and yield a simplified magnetic model of the complete object. This magnetic model can then be used to compute the magnetic field at any point outside the magnetic material.

The MoM is similar to FEM in some ways. As stated above, the MoM also meshes a volume and defines basis functions per element. However, it only meshes the magnetic material, and therefore one expects the matrix that is to be inverted, is smaller than the one in FEM. On the other hand, the matrix becomes denser as each element has en interaction with all others. Therefore it is not immediately clear which system is easier to invert or has lower computational costs. Especially when one wants an accurate computation of the magnetic field near to the object, as this requires a finer mesh. A clear positive aspect of the MoM, is that is does not need to approximate the outside domain by a finite domain, as the outside domain is not meshed.

1.2.3. Decreasing Spherical Harmonic Expansion

The Decreasing Spherical Harmonic Expansion is a widely used expansion to model magnetic fields. For example, the World Magnetic Model (WMM) and its extended version WMM-High Resolution (WMMHR) are built of a spherical harmonic expansion up to orders 15 and 133 respectively [4, p. 9]. The WMM and the first 15 orders of the WMMHR represent the earths core magnetic field, and the other orders of the WMMHR represent crustal magnetic field. This example shows the expansion can be used for very detailed spherical functions.

Measurements are used to find the DSHE coefficients. These coefficients represent a set of multipoles located at the centre of the spherical expansion. The multipoles are ordered in a decreasing manner, that is, a higher order multipole decreases faster for increasing r, than a lower order multipole does.

Using these coefficients, the magnetic field can be easily computed for any point outside the Brillouin Sphere (BS), which is the smallest sphere containing all sources. Also, because of the decreasing ordering, the general shape of the magnetic field is very clear from the found coefficients.

The DSHE coefficients can be found in two ways. For the first, measurements on a spherical surface outside of the BS are needed. Then one only needs to take an inner product between the measurements and the predefined basis functions, to find the coefficients of the DSHE. Because of this, no meshing of the 3-dimensional magnetic object is needed. Meshing of the 2-dimensional spherical surface on which the inner product is taken is enough.

The second method also uses measurements outside of the BS. One can then build a matrix that contains the contribution of each basis function Y_k^m to each of the measurement locations. The RHS vector contains the measurements, and the vector $\mathbf{x}$ the coefficients of the DSHE. Solving the matrix vector system, thus yields the coefficients. For this method, no meshing is needed at all. However, if the measurements are distributed badly, the system will be ill-conditioned and difficult to invert.

The downside of this method, is that the input to find the coefficients needs to be outside the BS, and that the found magnetic field only holds in the same region. In both of our applications, the measurements occur (partially) within the BS, so the DSHE is not usable.

1.2.4. Arbitrary-Surface Harmonic Expansion

The method investigated in this thesis, solves the issues of the previously described methods. In our application, we are interested in the magnetic field both close to, and far from the source. However, we do not want to define and mesh a large domain in which we compute the magnetic field at once.

The method is introduced in [6]. We call it the Arbitrary-Surface Harmonic Expansion, as it can be easily mapped to the DSHE, but also gives us information on the volume within the BS and outside of an arbitrarily shaped surface surrounding all sources. This way we can use measurements within the BS, to compute a source model. Using this source model, we can compute the magnetic field anywhere within the BS, and easily map to the DSHE, to describe the general shape and decay of the magnetic field.

The source model is built up of convenient basis functions. To compute the coefficients of the expansion, we perform a similar matrix inversion as we described for the DSHE. We use measurements, anywhere outside of the arbitrary surface, and store them in the RHS vector. Then we solve the system, where the matrix A consists of the contributions per basis function to each of the measurement points.

1.3. Research Questions

The method introduced in [6] and [7] has only been applied in particular settings, and still contains some ambiguities.

- Up until now, the method has only been applied to geometries with ”simple” shapes. In [6] the method is applied to a shape consisting of two boxes, and it uses approximately 5000 measurements of the magnetic scalar potential distributed well across its surface. In [7] the method is applied to a cylinder, and it uses 14 measurements slightly outside the cylinder on the side and top. They use Bayesian inference to regularise the heavily underdetermined system. In our thesis, we apply the method to a more complex shape: a simplified geometry of the Albatros ferry. Furthermore, we check if Bayesian inference allows us to use only a few, badly distributed and/or noisy measurements.
- The second ambiguity regards the mapping from the expansion to the DSHE. In [6] the coefficients of the DSHE are computed up to some order, and validated with the analytical coefficients. However, the error in the magnetic field outside the BS is never computed or shown. In this thesis we will investigate how well the found DSHE actually performs.
- Finally, we focus on the question of why an orthogonal basis is uesd to describe the equivalent source in [6]. The orthogonal basis leads to some properties that are convenient, but it is unclear if any of them are necessary. In both [6] and [7] orthogonalisation issues are described as the limiting factor of getting smaller errors. We will check whether the orthogonalisation is necessary, and if not, how well the method performs with a non-orthogonal basis.

In this thesis we apply the method to a new context, and try to clarify these ambiguities. We answer the following research question:

Can we find an alternative magnetic source model of a ship that is defined on the ships outer surface, using a basis that is convenient to map to the DSHE?

To answer this question, we answer the following sub-questions:

1. How well does the method introduced in [6] perform on finding a source model on more complex shapes like the ferry ship Albatros?

2. Does Bayesian inference, as introduced in [7], make the method usable in cases where there are only a few, badly distributed, and/or noisy measurements available?
3. How well does the mapping from the coefficients of the source model expansion to the coefficients of the DSHE outside of the BS perform?
4. Why do we use orthogonal basis functions for the source model on the arbitrary surface, and how does the method perform if we use another non-orthogonal basis?

Finally, we give some more details on the Albatros ferry ship.

1.3.1. The Albatros

Later in 2026, a measurement campaign will be held to investigate the magnetic field of the ferry ship Albatros. A sensor array will be placed on the seabed, on the ferry's route, perpendicular to its sailing direction.

As the Albatros is a ferry, it will sail across the sensors many times, and a lot of data can be collected. By focussing this thesis on the geometry of the Albatros, this thesis could be extended in future research by comparing the results with the measurements made later in 2026.

1.4. Outline

After this introduction, Chapter 2 gives a derivation of the used magnetostatics theory. Chapter 3 introduces a benchmark problem, which is used in the following chapters to validate new methods. After the definition of the benchmark problem, the Decreasing Spherical Harmonic Expansion is introduced in Chapter 4.

Next two equivalent magnetic sources are introduced in Chapter 5: the equivalent charge distribution (CD) and normal dipole distribution (NDD). We find the CD for the benchmark case, and look into some limitations of the equivalent sources.

The definition of the equivalent CD and NDD are then used to find a Multipolar Basis on an arbitrary surface surrounding all sources. This derivation is performed in Chapter 6. In Chapter 7 we describe how to compute the coefficients of the basis, and how to map the basis functions to the DSHE, answering sub-questions 1 and 3. The multipolar basis solves some of the issues of the general CD and NDD, but runs into a couple of new issues as well. These issues are caused by the introduction of noise, and the use of few or badly distributed measurements. Furthermore, we investigate whether orthogonalising the initial basis is necessary to start answering sub-question 4, and find that this is not the case.

Next, Bayesian inference is introduced in Chapter 8, to solve the issues of the expansion on the arbitrary surface. We apply the regularisation method to the orthogonal basis to answer sub-question 2, and find that it solves the issues. Finally we test it on the non-orthogonal basis to finish the answer to sub-question 4, and find that this brings up some new issues, but performs better than the orthogonal basis overall.

Chapter 9 revises the answers to all sub-questions and addresses the main research question. Furthermore, recommendations for future work are given, and the thesis is concluded.

2

Magnetostatics

In this thesis, we only consider static systems. Therefore, in this chapter we introduce Maxwell's equations simplified for static systems, and derive some important relations. We introduce the scalar magnetic potential, as it can be more convenient to work with than the magnetic field. Furthermore we construct a magnetic dipole, as it forms the basis for the higher order multipoles that are of importance in this thesis. Lastly we clarify the difference between the induced and permanent magnetisation of an object.

2.1. Maxwell's Equations for Static Systems

To derive the basis principles used in this thesis we start from Maxwell's equations, simplified for a magnetostatics system. The four equations then reduce to Gauss' law for magnetic fields, and the static (i.e. neglecting all time dependencies) version of Ampère's law [14, p. 180]:

$$\nabla \cdot \mathbf{B} = 0, \tag{2.1}$$

$$\nabla \times \mathbf{B} = \mu_0 \mathbf{J}. \tag{2.2}$$

Here $\mathbf{B}\,[\mathrm{T}]$ is the magnetic field, $\mathbf{J}\,[\mathrm{A/m^2}]$ is the electric current density, and $\mu_0\,[\mathrm{Tm/A}]$ the vacuum magnetic permeability.

Depending on the material in the magnetic field, magnetisation might occur. Magnetisation, denoted by $\mathbf{M}\,[\mathrm{A/m}]$, is the magnetic dipole moment per unit volume of a material [14, p. 192]. It causes a bounded current $\mathbf{J}_b$ according to

$$\mathbf{J}_b = \nabla \times \mathbf{M}. \tag{2.3}$$

To get back to the electric current density,

$$\mathbf{J} = \mathbf{J}_b + \mathbf{J}_f, \tag{2.4}$$

can always be written. Here $\mathbf{J}_f$ is the free current density. We now substitute Equations (2.3) and (2.4) into Equation (2.2), we get

$$\begin{aligned} \nabla \times \mathbf{B} &= \mu_0 \left(\mathbf{J}_f + \mathbf{J}_b\right) \\ &= \mu_0 \left(\mathbf{J}_f + \nabla \times \mathbf{M}\right). \end{aligned} \tag{2.5}$$

We now use $\mathbf{B}$ and $\mathbf{M}$ to define a new auxiliary field $\mathbf{H}\,[\mathrm{A/m}]$ [14, p. 192]:

$$\mathbf{H} := \frac{1}{\mu_0}\mathbf{B} - \mathbf{M}, \tag{2.6}$$

we can substitute Equation (2.6) into Equation (2.5). This allows us to write Ampère's law in terms of $\mathbf{H}$:

$$\nabla \times \mathbf{H} = \mathbf{J}_f. \tag{2.7}$$

In our setting we assume there is no free current present. Together with repeating Gauss' law, and rewriting the definition of $\mathbf{H}$, this yields

$$\nabla \cdot \mathbf{B} = 0, \tag{2.8}$$
$$\nabla \times \mathbf{H} = \mathbf{0}, \tag{2.9}$$
$$\mathbf{B} = \mu_0(\mathbf{H} + \mathbf{M}). \tag{2.10}$$

In Chapter 8 of this thesis, Bayesian inference is introduced and applied as a regularization method. In this method, one needs samples of the magnetic field. We create these samples with the MoM, where we assume the magnetised material to be linear, isotropic, and homogeneous.

A material is said to be isotropic when its properties are the same in all directions, and homogeneous if the properties are the same at each point within the material [13, pp. 189-190].

When the magnetised material satisfies these conditions, a linear relation occurs between the magnetisation and auxiliary field $\mathbf{H}$:

$$\mathbf{M} = \chi_m \mathbf{H}, \tag{2.11}$$

where χ_m [-] is the magnetic susceptibility. We substitute this relation into Equation (2.10), and get:

$$\mathbf{B} = \mu_0(\mathbf{H} + \chi_m \mathbf{H}) = \mu_0(1 + \chi_m)\mathbf{H} = \mu_0\mu_r\mathbf{H} = \mu\mathbf{H}. \tag{2.12}$$

Here, μ_r [-] is the relative magnetic permeability of the material, and $\mu = \mu_0\mu_r = \mu_0(1 + \chi_m)$ [Tm/A] the material its permeability. In Chapter 8, we vary μ_r (or χ_m) as input to the MoM, to obtain more diverse samples. A more extensive explanation of this is given in Chapter 8.

After using the MoM's output as input for the methods discussed in this thesis, we do not consider the magnetic field within the magnetised object. In this free space, we have $\mathbf{M} = \mathbf{0}$, and thus we get [14, p. 193]:

$$\mathbf{B} = \mu_0\mathbf{H}. \tag{2.13}$$

Thus, in free space (and within a linear, isotropic and homogeneous material) the fields $\mathbf{B}$ and $\mathbf{H}$ are equal up to a constant. The auxiliary magnetic field $\mathbf{H}$ is a convenient mathematical quantity, while the $\mathbf{B}$-field can be measured with a magnetometer. In this thesis we mostly refer to the auxiliary field $\mathbf{H}$ when talking about the magnetic field. However, as we only consider magnetic fields in free space, the two can be interchanged at any time according to Equation (2.13).

2.2. Magnetic Potentials

As stated before, in this thesis we assume no free current is present. Therefore we have $\nabla \times \mathbf{H} = 0$, and we can define a scalar magnetic potential $\phi\,[\mathrm{A}]$ such that [14, p. 195]:

$$\mathbf{H} = -\nabla\phi. \tag{2.14}$$

Now when there are no sources present, we have $\mathbf{B} = \mu_0 \mathbf{H}$. In this case $\nabla \cdot \mathbf{H} = 0$, as $\nabla \cdot \mathbf{B} = 0$ always holds. This yields the Laplace equation that the scalar potential ϕ needs to solve:

$$\nabla^2\phi = 0. \tag{2.15}$$

2.2.1. Green's Function for the Laplace Equation

Some derivations in this thesis are based on scalar potentials solving the Laplace equation, and use Green's second identity for Green's functions. Therefore we derive the Green's function for the Laplace equation. The Green's function solves

$$\nabla^2 G(\mathbf{r}) = -\delta(\mathbf{r}), \tag{2.16}$$

where the Dirac Delta function can also be off centred.

As the Laplace operator is invariant to rotation, we expect the solution to only depend on the distance r to the origin. We thus write $G(\mathbf{r}) = G(r)$ and $\nabla G(r) = \partial_r G(r)$. Next, we integrate both sides of the equation over the ball $B_a(\mathbf{0})$ of radius a with the origin as centre. We get

$$\int_{B_a(\mathbf{0})} \nabla^2 G(r)\mathrm{d}V = -1. \tag{2.17}$$

Now by applying the divergence theorem to $\nabla^2 G(r)$ over the volume $B_a(\mathbf{0})$, we get:

$$\int_{\partial B_a(\mathbf{0})} \nabla G(r) \cdot \hat{\mathbf{r}}\,\mathrm{d}S = -1, \tag{2.18}$$

as the normal vector on $\partial B_a(\mathbf{0})$ is $\hat{\mathbf{r}}$. Note that

$$\nabla G(r) = \partial_r G(r)\hat{\mathbf{r}} + \frac{1}{r}\partial_\theta G(r)\hat{\theta} + \frac{1}{r\sin\theta}\partial_\varphi G(r)\hat{\varphi} = \partial_r G(r)\hat{\mathbf{r}} \tag{2.19}$$

is constant on $\partial B_a(\mathbf{0})$. Therefore Equation (2.18) simplifies to this constant value multiplied by the surface area of $\partial B_a(\mathbf{0})$:

$$-1 = 4\pi a^2 \partial_r G(r)|_{r=a}. \tag{2.20}$$

Rewriting gives

$$\partial_r G(r) = -\frac{1}{4\pi r^2}. \tag{2.21}$$

We integrate, and put the integration constant to zero, as we want a zero potential at infinity. For clarity, we also write G as a function of $\mathbf{r}$ again. This yields

$$G(\mathbf{r}) = \frac{1}{4\pi}\frac{1}{||\mathbf{r}||_2}. \tag{2.22}$$

Now we suppose that the source in Equation (2.16) is not located at the origin, but at $\tilde{\mathbf{r}}$. We can shift the solution to get

$$G(\mathbf{r}, \tilde{\mathbf{r}}) = \frac{1}{4\pi} \frac{1}{||\mathbf{r} - \tilde{\mathbf{r}}||_2}. \tag{2.23}$$

2.3. Construction of a Magnetic Dipole

In this report we study an alternative source model for magnetic fields. The new model is based on the Decreasing Spherical Harmonic Expansion (DSHE), which represents a set of magnetic multipoles located at the centre of the expansion. To get a better grasp of what multipoles are, we derive the magnetic monopole and dipole in this section. In Chapter 4 the higher order multipoles are introduced and the DSHE is derived. In Chapter 6 the new model is described.

Parallel to electrostatics

In electrostatics, a monopole would be a point charge like an electron. A magnetostatics equivalent does not exist. The difference between Maxwell's equations for an electrostatic system, and for a magnetostatic system also reflect this.

Recall that if there are no free currents, from the equations $\nabla \times \mathbf{B} = 0$ and $\nabla \cdot \mathbf{B} = 0$ we could derive that a magnetic scalar potential exists that solves the Laplace equation $\nabla^2 \phi = 0$. Similar equations can be found for an electrostatic system. We have $\nabla \cdot \mathbf{E} = \frac{\rho}{\epsilon_0}$, where ρ is the electric charge density, which can consist of such monopoles. Furthermore we have $\nabla \times \mathbf{E} = \mathbf{0}$, so there exists an electric potential $\phi_{\mathbf{E}}$ such that $\nabla \phi_{\mathbf{E}} = \mathbf{E}$. From this we find that $\phi_{\mathbf{E}}$ solves the Poisson equation $\nabla^2 \phi_{\mathbf{E}} = \frac{\rho}{\epsilon_0}$.

An electric monopole has a charge distribution shaped like a Dirac delta function $\delta(\mathbf{r})$, and a potential proportional to $f(\mathbf{r}) = \frac{1}{||\mathbf{r}||_2}$. Such a monopole does solve the Poisson equation, but not the Laplace equation.

Although magnetic monopoles do not exist physically, or solve the Laplace equation, it sometimes appears convenient to model magnetic sources as monopoles and multipoles. To do this, we slightly alter the Laplace equation. For a magnetic monopole of magnitude n in the origin, we say that the Laplace equation holds for all $\mathbf{r} \neq \mathbf{0}$. However, in the origin we have

$$\nabla \phi^{(0)}(\mathbf{r}) = -n\, \delta(\mathbf{r}). \tag{2.24}$$

Note that a new notation is introduced. The scalar magnetic potential at location $\mathbf{r}$, caused by a multipole of order $k = 0, 1, 2, \ldots$, is denoted by $\phi^{(k)}(\mathbf{r})$.

Equation (2.24) is very similar to the one we solved in Section 2.2.1 to find the Green's function of the Laplace equation. In a similar manner we get the solution [13, p. 154]:

$$\phi^{(0)}(\mathbf{r}) = \frac{1}{4\pi} \frac{n}{||\mathbf{r}||_2}. \tag{2.25}$$

Placing two monopoles close to each other

In this section we derive the magnetic scalar potential of a magnetic dipole. We follow the structure of [13, pp. 151-155]. We put one monopole of magnitude $+n$ at position $\mathbf{r} = +\frac{1}{2}\mathbf{a}$ and one monopole of magnitude $-n$ at $\mathbf{r} = -\frac{1}{2}\mathbf{a}$. We define the dipole moment as $\mathbf{m} \equiv n\mathbf{a}$ [Am^2]. See Figure 2.1 for a sketch of the situation. Our magnetic potential [13, p. 151]:

$$\phi(\mathbf{r}) = \frac{1}{4\pi} n \left(\frac{1}{||\mathbf{r} - \frac{\mathbf{a}}{2}||_2} - \frac{1}{||\mathbf{r} + \frac{\mathbf{a}}{2}||_2} \right). \tag{2.26}$$

We now let $\mathbf{m}$ be constant, and want to let $||\mathbf{a}||_2 \to 0$ (and with that $n \to \infty$). To do this, consider the Taylor expansion of $\frac{1}{||\mathbf{r} \pm \mathbf{a}/2||_2}$ about $\frac{\mathbf{a}}{2} = \mathbf{0}$. We get

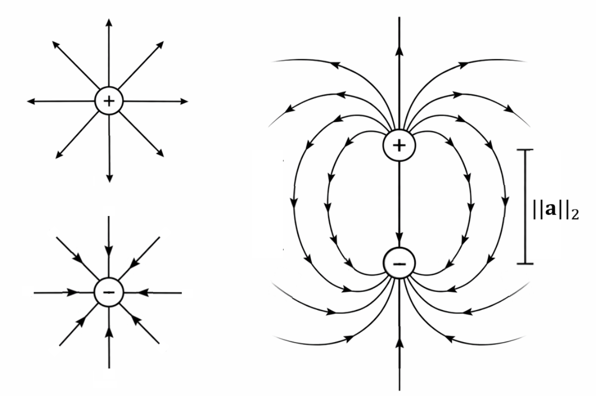

Figure 2.1: A positive and negative magnetic monopole, and their interaction when placed at a distance $||\mathbf{a}||_2$ from each other.

$$\frac{1}{||\mathbf{r} \pm \frac{\mathbf{a}}{2}||_2} = \frac{1}{r} + \frac{\mathbf{a}}{2} \cdot \left[\nabla_{\frac{\mathbf{a}}{2}} \frac{1}{||r \pm \frac{\mathbf{a}}{2}||_2} \right]_{\frac{\mathbf{a}}{2} = \mathbf{0}} + \mathcal{O}\left(\left|\left| \frac{\mathbf{a}}{2} \right|\right|_2^2 \right) \tag{2.27}$$

$$= \frac{1}{r} + \frac{\mathbf{a}}{2} \cdot \left[\frac{\mp \mathbf{r} - \frac{\mathbf{a}}{2}}{||\mathbf{r} \pm \frac{\mathbf{a}}{2}||_2^3} \right]_{\frac{\mathbf{a}}{2} = \mathbf{0}} + \mathcal{O}(||\mathbf{a}||_2^2) \tag{2.28}$$

$$= \frac{1}{r} \mp \frac{1}{2} \frac{\mathbf{a} \cdot \mathbf{r}}{||\mathbf{r}||_2^3} + \mathcal{O}(||\mathbf{a}||_2^2). \tag{2.29}$$

We can now rewrite Equation (2.26) to

$$\phi(\mathbf{r}) = \frac{1}{4\pi} n \left(\frac{\mathbf{a} \cdot \mathbf{r}}{r^3} + \mathcal{O}(||\mathbf{a}||_2^2) \right) = \frac{1}{4\pi} \frac{\mathbf{m} \cdot \mathbf{r}}{r^3} + \mathcal{O}(n||\mathbf{a}||_2^2) \tag{2.30}$$

$$= \frac{1}{4\pi} \frac{\mathbf{m} \cdot \mathbf{r}}{r^3} + \mathcal{O}(||\mathbf{m}||_2 ||\mathbf{a}||_2) = \frac{1}{4\pi} \frac{\mathbf{m} \cdot \mathbf{r}}{r^3} + \mathcal{O}(||\mathbf{a}||_2). \tag{2.31}$$

We can now let $||\mathbf{a}||_2 \to 0$. This gives us the scalar magnetic potential of a magnetic dipole of magnitude $\mathbf{m}$ [13, p. 155]:

$$\phi^{(1)}(\mathbf{r}) = \frac{1}{4\pi} \frac{\mathbf{m} \cdot \mathbf{r}}{r^3}. \tag{2.32}$$

Suppose the monopole, and dipole are not in the origin, but at a location $\mathbf{r}_q$. We replace $\mathbf{r}$ by $\mathbf{r} - \mathbf{r}_q$ to get

$$\phi^{(0)}(\mathbf{r}, \mathbf{r}_q) = \frac{1}{4\pi} \frac{n}{||\mathbf{r} - \mathbf{r}_q||_2}, \tag{2.33}$$

and

$$\phi^{(1)}(\mathbf{r}, \mathbf{r}_q) = \frac{1}{4\pi} \frac{\mathbf{m} \cdot (\mathbf{r} - \mathbf{r}_q)}{||\mathbf{r} - \mathbf{r}_q||_2^3}. \tag{2.34}$$

We now note that

$$\phi^{(1)}(\mathbf{r}, \mathbf{r}_q) = \mathbf{m} \cdot \nabla_{\mathbf{r}_q} \frac{1}{n} \phi^{(0)}(\mathbf{r}, \mathbf{r}_q). \tag{2.35}$$

This relation is necessary for the derivation of the DSHE in Chapter 4.

Deriving the magnetic field of a dipole from its magnetic scalar potential

Furthermore, from the magnetic scalar potential, we can also derive the magnetic field $\mathbf{H}$ of a magnetic dipole. We first derive it for $\mathbf{r}_q = \mathbf{0}$:

$$\begin{aligned}\mathbf{H}^{(1)}(\mathbf{r}, \mathbf{0}) &= -\nabla_{\mathbf{r}}\, \phi^{(1)}(\mathbf{r}, \mathbf{0}) \\ &= -\nabla_{\mathbf{r}} \frac{1}{4\pi} \frac{\mathbf{m} \cdot \mathbf{r}}{||\mathbf{r}||_2^3} \\ &= -\frac{1}{4\pi ||\mathbf{r}||_2^3} \nabla_{\mathbf{r}}\, \mathbf{m} \cdot \mathbf{r} - \frac{\mathbf{m} \cdot \mathbf{r}}{4\pi} \nabla_{\mathbf{r}}\, ||\mathbf{r}||_2^{-3} \\ &= -\frac{\mathbf{m}}{4\pi ||\mathbf{r}||_2^3} - \frac{\mathbf{m} \cdot \mathbf{r}}{4\pi} (-3\mathbf{r}||\mathbf{r}||^{-5}) \\ &= \frac{1}{4\pi} \frac{3\mathbf{r}(\mathbf{m} \cdot \mathbf{r}) - \mathbf{m}\, ||\mathbf{r}||_2^2}{||\mathbf{r}||_2^5}. \end{aligned} \tag{2.36}$$

Now we again replace $\mathbf{r}$ by $\mathbf{r} - \mathbf{r}_q$:

$$\mathbf{H}^{(1)}(\mathbf{r}, \mathbf{r}_q) = \frac{1}{4\pi} \frac{3(\mathbf{r} - \mathbf{r}_q)(\mathbf{m} \cdot (\mathbf{r} - \mathbf{r}_q)) - \mathbf{m}\, ||\mathbf{r} - \mathbf{r}_q||_2^2}{||\mathbf{r} - \mathbf{r}_q||_2^5}. \tag{2.37}$$

We now evaluate this magnetic field for an off centred dipole at position $\mathbf{r}_q = (2, 1, 0)$ m and of magnitude $\mathbf{m} = (0, 0, 1)$ Am^2. The result is given in Figure 2.2.

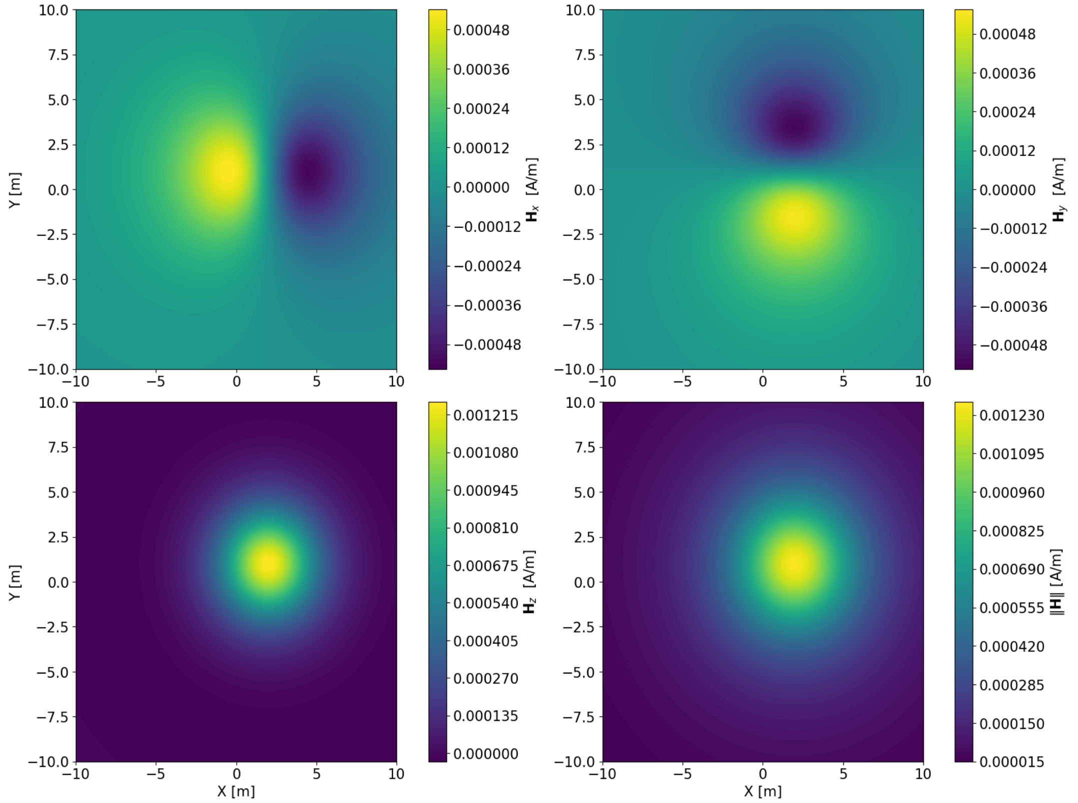

Figure 2.2: The magnetic auxiliary field $\mathbf{H}$ of an off centred dipole at location $\mathbf{r}_q = (2, 1, 0)$ m and of magnitude $\mathbf{m} = (0, 0, 1)$ Am^2. The field is evaluated on a 20 m × 20 m surface on $z = -5$ m.

In Chapter 4, this derivation is extended to higher order multipoles, and eventually the DSHE.

2.4. Induced and Permanent Magnetisation

In magnetostatics, the magnetisation of an object can be split into an induced part, and a permanent part [22, Section 3.3.1]. This section clarifies the difference between the induced and permanent part. Furthermore it introduces how the permanent magnetisation is modelled in this thesis.

When a ferromagnetic object is placed in a magnetic background field $\mathbf{B}_0$, the object obtains an induced magnetisation $\mathbf{M}_{\text{ind}}$ and this magnetisation then alters the magnetic field around it. The total magnetic field can then be described as

$$\mathbf{B} = \mathbf{B}_0 + \mathbf{B}_{\text{ind}}. \tag{2.38}$$

The induced magnetic field $\mathbf{B}_{\text{ind}}$ and the induced magnetisation $\mathbf{M}_{\text{ind}}$, instantly go to zero when the background field $\mathbf{B}_0$ is put to zero. Furthermore, if the objects orientation changes within the background field, the induced magnetisation and magnetic field also change.

Besides the induced magnetisation, a ferromagnetic object can obtain a permanent magnetisation. The permanent magnetisation can form or change due to many factors. An example of those factors is hysteresis, where a past magnetic field and its induced magnetisation leave behind a permanent magnetisation [13, p.290].

The permanent magnetisation also alters the magnetic field around the object, however it does not go to zero when the background field is put to zero, or change when the objects orientation changes. We get

$$\mathbf{M} = \mathbf{M}_{\text{ind}} + \mathbf{M}_{\text{perm}}, \tag{2.39}$$

$$\mathbf{B} = \mathbf{B}_0 + \mathbf{B}_{\text{ind}} + \mathbf{B}_{\text{perm}}. \tag{2.40}$$

The permanent magnetisation of an object is hard to model and hard to determine in reality. However, its contribution to the magnetic field is significant, and therefore it is important to test whether a method can deal with such contributions. In this thesis we first focus on testing our method on generated measurements containing just the induced magnetic field. Later in the thesis, we try to test the method on generated measurements consisting of both an induced and permanent part. The way the permanent part of the measurements is generated is described in Section 8.2.3.

3

Introduction of Benchmark Problems

Throughout this thesis, the magnetic field of the Albatros is used as the main benchmark problem. Measurements of the magnetic field are generated using the Albatros' simplified geometry and the Method of Moments (MoM). These simulations are then used to apply the methods discussed in this thesis, and to perform comparisons with the resulting fields. This benchmark is introduced in this chapter and reappears throughout the body of this thesis.

In addition, the problem presented in [6] was reproduced to verify the correctness of the numerical implementation. The obtained results were consistent with those reported in the literature. As this exercise serves solely as a validation step, the setup and results are not included in this report.

3.1. Albatros Benchmark Problem

As stated in the introduction, a measurement campaign will be held later in 2026, to collect magnetic field data around the Albatros. Although the measurements are not ready to be used in this thesis, the geometry can be used to compute numerical 'measurements' as an alternative. The measurements will be performed both on the seabed, as well as at other points around the ship. Therefore, we do not solely focus on the measurements on the seabed within this thesis. From now on, we refer to these 'measurements' as simulations as well. The locations of these simulations are discussed in Section 3.1.2.

3.1.1. Simplified Geometry

The simplification of the geometry consists of the lack of the plates within the ship. Only the outer surface of the ship is included in the geometry. Furthermore, the thickness and magnetic permeability of all 2D mesh elements are taken equal. As stated in Chapter 1, the MoM can then determine the induced magnetic field of the ferromagnetic geometry. The details of this method are outside of the scope of this thesis, but can be found in [19] and [10].

Regarding the missing inner plates, we note that this simplification might make the Albatros its magnetisation easier to model with a surface charge distribution (or normal dipole distribution), as introduced in Chapter 5. The magnetisation of the Albatros computed by the MoM, is completely defined on, or very close to its outer surface. Intuitively it seems easier to find an alternative source on the outer surface for such a magnetisation, than an object with a magnetised core. Determining whether this intuition is correct, is out of the scope of this thesis. However, it is recommended to keep it in mind in future work.

3.1.2. Simulation Locations

The simulation data is needed at multiple points within the methods described in this thesis. In general, we are trying to find a source model for a given set of measurements. Therefore, the first set of simulation data, is used to build the measurement vector $\mathbf{b}$ from $A\mathbf{x} = \mathbf{b}$. The definitions of A and $\mathbf{x}$ differ throughout the chapters, based on the type of source model that is used. The vector $\mathbf{b}$ is built up of simulation data on either, a box shaped surface close to the ship, or a rectangular surface below the ship at a depth of 13.7 m resembling the seabed on the route of the Albatros. Figure 3.1 gives an illustration of these simulation points:

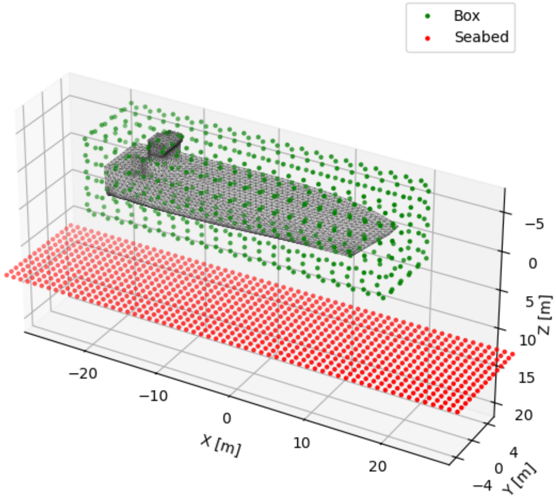

Figure 3.1: The simplified geometry of the Albatros, and the simulation points used to find a source model of the ship. The green points are on a box, that is at least at a distance 1 m of the ship in all directions. The red dots are on a surface of 60×14 m^2 large, at a depth of 13.7 m.

After determining the source model, the found source model also needs to be validated. For that, we introduce two error planes. Throughout this thesis, it is of importance whether measurements within or outside of the Brillouin Sphere (BS). (Recall from Section 1.2.3 that the BS is the smallest sphere containing all sources.) Therefore one error plane is completely outside of the BS at a depth of 20 m, and the other is partially within the BS at a depth of 10 m.

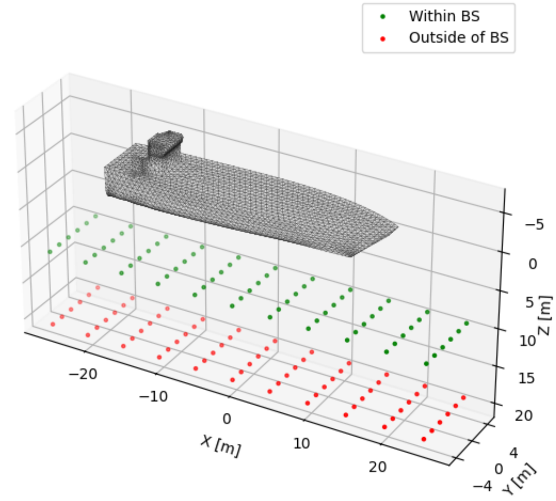

Figure 3.2: The simplified geometry of the Albatros, and the simulation points used to validate the found source model of the ship. The green points are on an error plane partially within the Brillouin Sphere (BS) at a depth of 10 m, and the other is completely outside of the BS at a depth of 20 m. Both error planes are 50×10 m^2 large.

3.1.3. Dipole Model of Albatros

Besides the measurements computed with the MoM code, a simplified dipole model is available for the ship in a specific background field. The model consists of five dipoles, located within the ships shell. The dipoles have been found, using the method described in [23]. The background field is $\mathbf{B}_0 = (23.360, 0, 41.234)\,\mu$T or $\mathbf{H}_0 = \mathbf{B}_0/\mu_0 = (18.589, 0, 32.813)$ A/m. The dipole locations and moments are given in Table 3.1:

Dipole	x [m]	y [m]	z [m]	m_x [Am^2]	m_y [Am^2]	m_z [Am^2]
1	-14.3559	0.0876	-0.5824	3766.93	-976.49	8750.60
2	7.0241	0.0171	0.5262	-7832.04	-20107.66	42891.07
3	9.0208	-1.0627	0.9887	91083.55	140092.60	-126678.91
4	9.1714	-1.2340	1.1687	-64636.27	-120264.23	96493.34
5	-8.3636	-0.4116	-1.8160	22450.54	1185.12	3964.39

Table 3.1: Locations and magnetic moments of the five-dipole model. The locations are rounded to four decimals, and the moments are rounded to two decimals. The dipole locations and moments were computed according to [24].

This alternative dipole model has not been tested thoroughly, unlike the MoM code. Therefore we are careful in how we use the model. It does however give us an extra way to check the quality of the coefficients of the DSHE found with the methods discussed in Chapters 4 and 6. For this we use an equation that yields the coefficients for an off-centred dipole that is derived in section 4.2.1.

Figure 3.3 depicts the Albatros and the alternative dipole model:

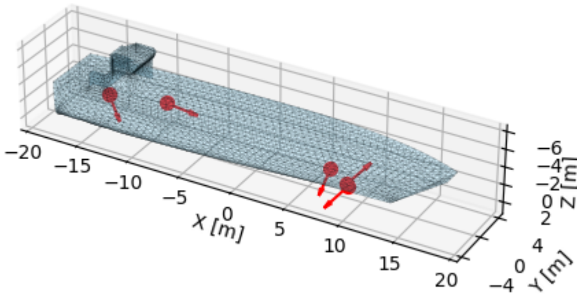

Figure 3.3: The simplified geometry of the Albatros, and its approximately equivalent dipole model. The dipoles moments and locations are given in Table 3.1. The directions and locations of the dipoles in the figure are accurate, however the magnitudes are normalized.

Lastly we plot the magnetic field $\mathbf{H}$ on the error plane within the BS, found using the dipole model. We compare it to the simulation data (computed with the MoM using $\mathbf{H}_0 = (18.589, 0, 32.813)$ A/m), and plot a safe error. The safe error of the i-'th component of the magnetic field, is defined as

$$e(\mathbf{x}) = \frac{(\mathbf{H}_{\mathrm{sim},i}(\mathbf{x}) - \mathbf{H}_{\mathrm{approx},i}(\mathbf{x}))^2}{(|\mathbf{H}_{\mathrm{sim},i}(\mathbf{x})| + |\mathbf{H}_{\mathrm{approx},i}(\mathbf{x})| + \epsilon)^2}, \tag{3.1}$$

where we choose $\epsilon = 10^{-8}$, and the i'th component can be in the x, y, z-direction, or the norm of the magnetic field. The safe error prevents the error from blowing up when $||\mathbf{H}(\mathbf{x})||_2 \approx 0$. The results are given in Figures 3.4 and 3.5.

In Figure 3.4, we see that the induced magnetic field within the BS, cannot be approximated very well with the alternative dipole model. This can be seen quickly by comparing the plots in the left two columns.

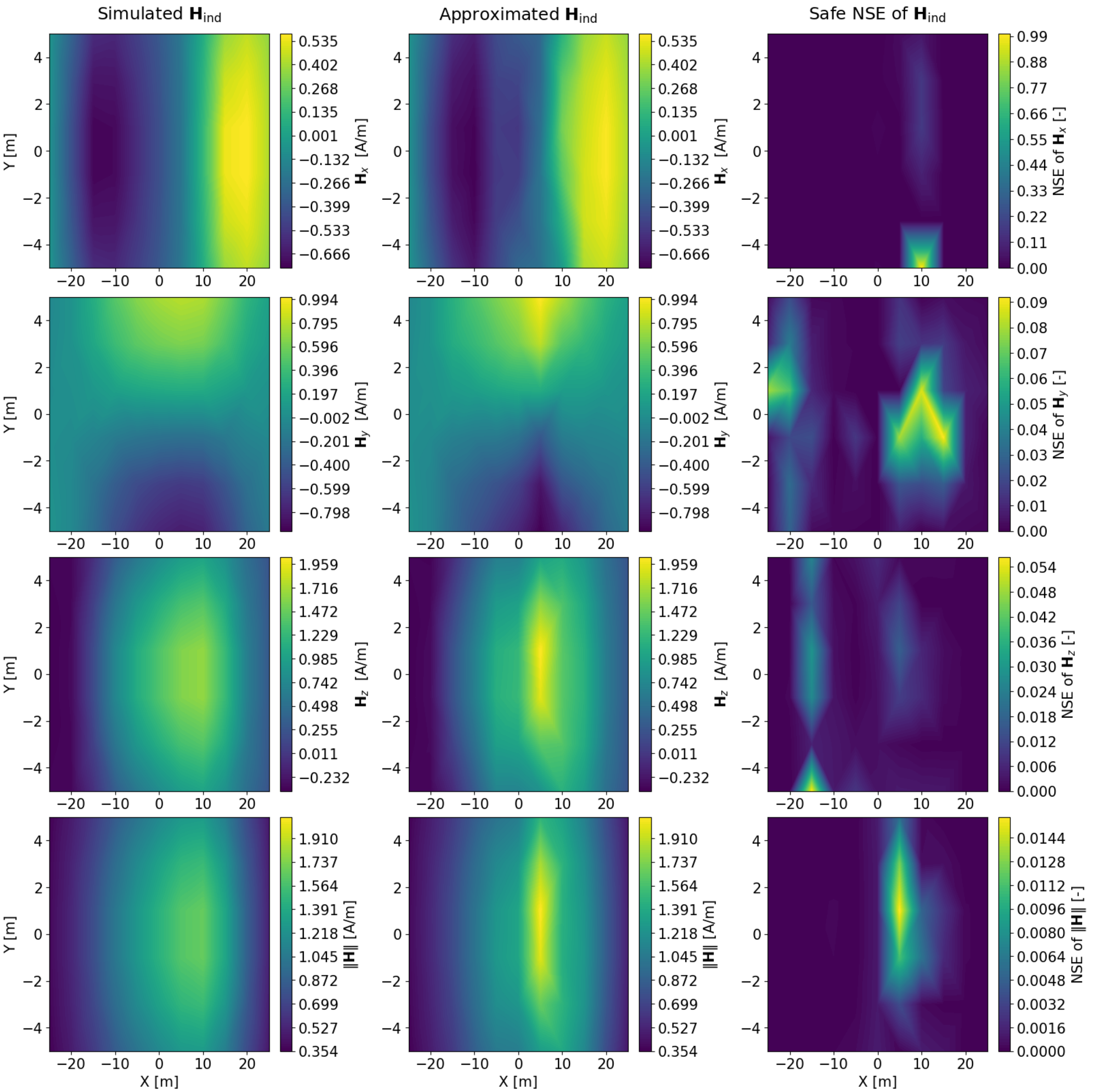

Figure 3.4: The induced magnetic field $\mathbf{H}_{\mathrm{ind}}$ of the alternative dipole model, compared to the simulated data computed with the MoM and a safe squared error defined in Equation (3.1). The rows show the different components of $\mathbf{H}_{\mathrm{ind}}$, and its norm. The magnetic background field is defined by $\mathbf{H}_0 = (18.589, 0, 32.813)$ A/m. The used magnetic background field was $\mathbf{B}_0 = (23.360, 0, 41.234)\,\mu\mathrm{T}$. The magnetic field and error were evaluated on the error plane partially within the BS and below the ship like in Figure 3.2.

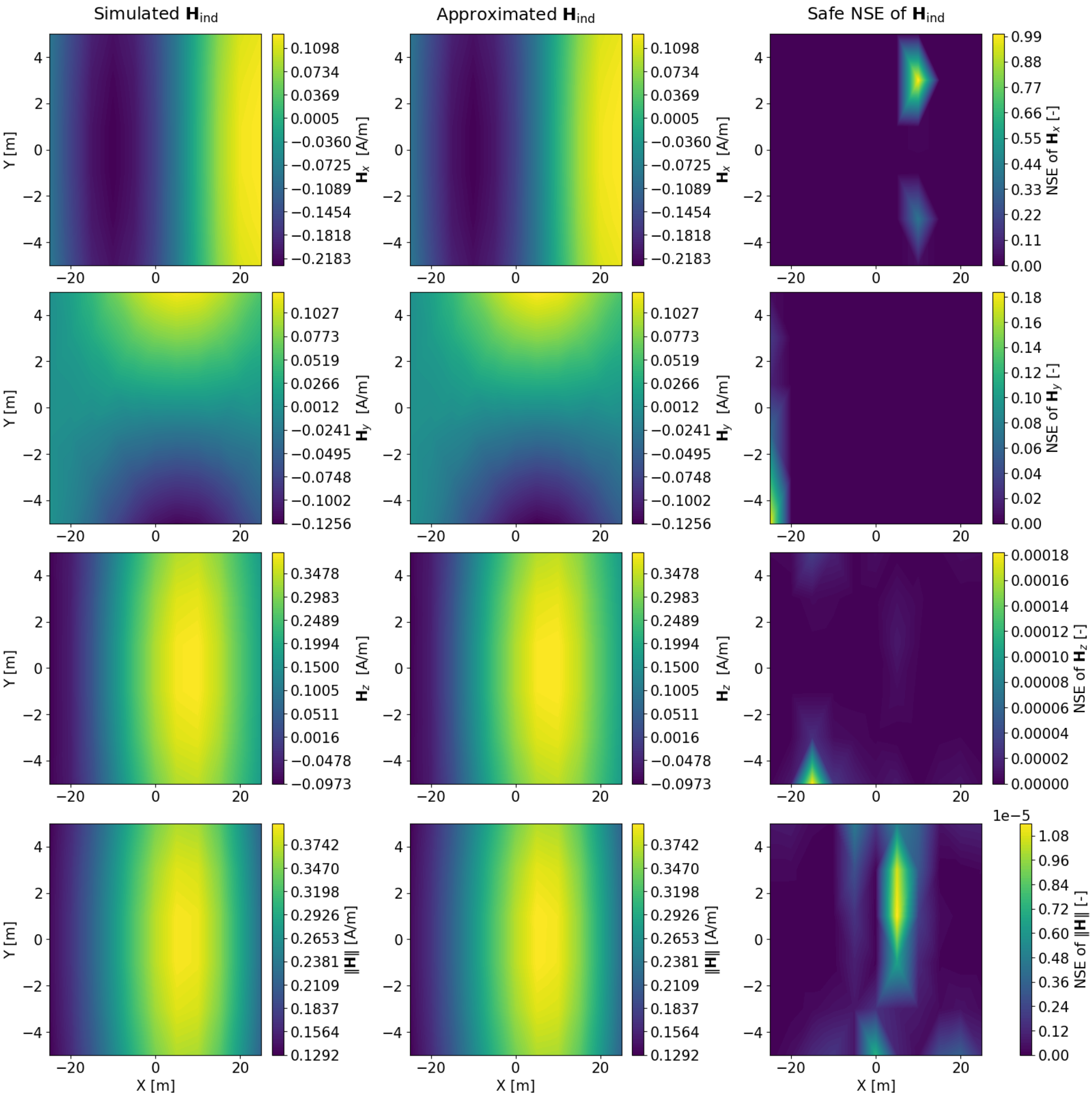

Figure 3.5: The induced magnetic field $\mathbf{H}_{\text{ind}}$ of the alternative dipole model, compared to the simulated data computed with the MoM and a safe squared error defined in Equation (3.1). The rows show the different components of $\mathbf{H}_{\text{ind}}$, and its norm. The magnetic background field is defined by $\mathbf{H}_0 = (18.589, 0, 32.813)$ A/m. The used magnetic background field was $\mathbf{B}_0 = (23.360, 0, 41.234)\ \mu\text{T}$. The magnetic field and error were evaluated on the error plane outside of the BS and below the ship like in Figure 3.2.

In Figure 3.5, we see that the induced magnetic field outside of the BS, can be reasonably approximated by the alternative dipole model. The general shape of the plots in the left two columns look equivalent. Furthermore, the only places where the error plot yields large values, are where $||\mathbf{H}_{\text{ind}}||_2 \approx 0$ and the safe error still has issues preventing the blow-up.

3.1.4. Reappearance in Thesis

The Albatros benchmark problem reappears many times in this thesis. It is used in every chapter, to validate the method described in that chapter.

In Chapter 4 the Decreasing Spherical Harmonic Expansion (DSHE) is introduced. Multiple ways of determining the corresponding coefficients are explained, including a direct relation between the location and moment of a dipole, and the DSHE coefficients. Furthermore, in Section 4.3 it is confirmed that the DSHE only holds outside of the BS. Therefore, the alternative dipole model helps us validate the DSHE coefficients found using simulation data.

The DSHE coefficients also form a link between all chapters. Therefore, we choose to use the same background field ($\mathbf{H}_0 = (18.589, 0, 32.813)$ A/m) in all chapters.

In Chapters 5 and 6, a new source model and two possible bases are introduced. In Chapter 7 the computation of the coefficients of the basis from Chapter 6 is explained. In Chapters 5 and 7, we use the found models to forwardly compute an approximation of the induced field on the error planes, following the structure of the benchmark problem.

Lastly, in Chapter 8, Bayesian inference is introduced as regularisation to deal with noisy measurements while finding the coefficients of the basis introduced in Chapter 6. At this point, the benchmark problem is not extensive enough to fully evaluate the capabilities of the model and regularisation method. The components added to the benchmark problem, are discussed in that chapter.

4

Decreasing Spherical Harmonic Expansion and its Limitations

A broadly used method to model magnetic or electric sources, is the Decreasing Spherical Harmonic Expansion (DSHE). The DSHE is a very efficient source model, as once the coefficients are known, the magnetic field at any point in space (outside of the Brillouin sphere) can be computed with very low costs. It also lies at the basis of the Arbitrary-Surface Harmonic Expansion that is introduced in Chapter 6, as we want to be able to smoothly switch between the two bases of the expansions.

In this chapter we introduce the DSHE by first giving a sketch of the derivation of the expansion. Next we discuss three ways to determine the coefficients of the expansion, the first being an analytical method for off-centred dipoles. Finally we discuss the convergence behaviour of the DSHE, and why this leads to the need of an extra source model within the Brillouin sphere (BS).

4.1. Derivation of Decreasing Spherical Harmonic Expansion

A sketch of the derivation of the Decreasing Spherical Harmonic Expansion is now given. This is done by induction, following the structure of [20, sec. 3.12].

For $k = 0, 1, 2, \dots$, let $\phi^{(k)}(\mathbf{r}) = \frac{p^{(k)}}{4\pi} f_i(\mathbf{r})$ be the potential at point $\mathbf{r}$ caused by a magnetic multipole of order k and magnitude $-p^{(k)}$. Now put one such multipole at $\mathbf{r} = +\frac{1}{2}\mathbf{a}^{(k)}$, and another of opposite sign at $\mathbf{r} = -\frac{1}{2}\mathbf{a}^{(k)}$. Recall Figure 2.1 for a sketch of the situation when $k = 0$. The potential due to both points becomes

$$\phi^{(k+1)}(\mathbf{r}) = \frac{p^{(k)}}{4\pi}\left(f_i\left(\mathbf{r} - \frac{\mathbf{a}^{(k)}}{2}\right) - f_i\left(\mathbf{r} + \frac{\mathbf{a}^{(k)}}{2}\right)\right). \tag{4.1}$$

If we now consider the Taylor expansions of $f_i\left(\mathbf{r} - \frac{\mathbf{a}^{(k)}}{2}\right)$ and $f_i\left(\mathbf{r} + \frac{\mathbf{a}^{(k)}}{2}\right)$ about $\frac{\mathbf{a}^{(k)}}{2} = \mathbf{0}$, we get

$$f_i\left(\mathbf{r} \pm \frac{\mathbf{a}^{(k)}}{2}\right) = f_i(\mathbf{r}) \mp \frac{\mathbf{a}^{(k)}}{2} \cdot \nabla f_i(\mathbf{r}) + \mathcal{O}(||\mathbf{a}^{(k)}||_2^2). \tag{4.2}$$

This yields:

$$\phi^{(k+1)} = -\frac{p^{(k)}}{4\pi}\mathbf{a}^{(k)} \cdot \nabla f_i(\mathbf{r}) + \mathcal{O}(p^{(k)}||\mathbf{a}^{(k)}||_2^2). \tag{4.3}$$

We now define the magnitude of the multipole of order $k+1$ as $p^{(k+1)} = (k+1)p^{(k)}||\mathbf{a}^{(k)}||_2$, and keep it constant while we let $p^{(k)} \to 0$. We get

$$\phi^{(k+1)} = -\frac{1}{4\pi}\frac{p^{(k+1)}}{k+1}\hat{\mathbf{a}}^{(k)} \cdot \nabla f_i(\mathbf{r}) = -\frac{1}{4\pi}\frac{p^{(k+1)}}{k+1}\partial_{\hat{\mathbf{a}}^{(k)}} f_i(\mathbf{r}), \tag{4.4}$$

where $\hat{\mathbf{a}}^{(k)} = \frac{\mathbf{a}^{(k)}}{||\mathbf{a}^{(k)}||_2}$.

Now for a monopole, with $k = 0$, we have

$$\phi^{(0)} = \frac{p^{(0)}}{4\pi}\frac{1}{r}, \quad f_0 = \frac{1}{r}. \tag{4.5}$$

Indeed, for $k = 1$, the magnetic dipole satisfies the recursive formula, as

$$\phi^{(1)} = -\frac{p^{(1)}}{4\pi}\frac{\hat{\mathbf{a}}^{(0)} \cdot \mathbf{r}}{r^3} = -\frac{p^{(1)}}{4\pi}\partial_{\hat{\mathbf{a}}^{(0)}}\left(\frac{1}{r}\right). \tag{4.6}$$

From the recursive formula, we find

$$\phi^{(k)} = \frac{(-1)^k}{4\pi}\frac{p^{(k)}}{k!}\partial_{\hat{\mathbf{a}}^{(0)}}...\partial_{\hat{\mathbf{a}}^{(k-1)}}\left(\frac{1}{r}\right). \tag{4.7}$$

We now define Y_k as a function of cosines and sines of the angles between $\mathbf{r}$ and the k axes $\hat{\mathbf{a}}^{(k)}$. We then get

$$\phi^{(k)}(\mathbf{r}) = \frac{p^{(k)}}{4\pi}\frac{Y_k(\mathbf{r}, \mathbf{a}^{(0)}, ..., \hat{\mathbf{a}}^{(k-1)})}{r^{k+1}}. \tag{4.8}$$

The potential defined above, solves the Laplace equation for all $p^{(k)}$, and all $\hat{\mathbf{a}}^{(0)}, ..., \hat{\mathbf{a}}^{(k-1)}$. Since we have $||\hat{\mathbf{a}}^{(k)}|| = 1$, there are two variables to be chosen per $\hat{\mathbf{a}}^{(k)}$ vector. So in total, for the potential $\phi^{(k)}(\mathbf{r})$ we have $2k + 1$ free variables.

Any sum, of $\phi^{(k)}$'s satisfying these conditions, solves the Laplace equation. By [20, pp. 181-182], we find that we can rewrite this $p^{(k)}Y_k$ to:

$$p^{(k)}Y_k(\mathbf{r}, \hat{\mathbf{a}}^{(0)}, ..., \hat{\mathbf{a}}^{(k-1)}) = \sum_{m=-k}^{k} a_{km}Y_k^m(\theta, \varphi), \tag{4.9}$$

where we used $\mathbf{r} = (r, \theta, \varphi)$. We also used $Y_k^m(\theta, \varphi)$, which is the Spherical Harmonic function of order k and degree m, and is constructed with the associated Legendre polynomial $P_k^{|m|}$ of order $|m|$ and degree k. These functions are defined as

$$Y_k^m(\theta, \varphi) = \sqrt{\frac{(k-|m|)!}{(k+|m|)!}}P_k^{|m|}(\cos\theta)\begin{cases} \sqrt{2}\cos(m\varphi) & \text{if } m > 0, \\ 1 & \text{if } m = 0, \\ \sqrt{2}\sin(|m|\varphi) & \text{if } m < 0, \end{cases} \tag{4.10}$$

and

$$P_k^m(x) = (1-x^2)^{m/2}\frac{d^m}{dx^m}P_k(x), \tag{4.11}$$

with

$$P_k(x) = \frac{1}{2^k k!}\frac{d^k}{dx^k}(x^2-1)^k. \tag{4.12}$$

We have now defined $\phi^{(k)}$ for $k = 0, 1, 2, \ldots$. By summing over all $\phi^{(k)}$'s, we get the Decreasing Spherical Harmonic Functions (DSHF):

$$\phi(r,\theta,\varphi) = \frac{1}{4\pi}\sum_{k=0}^{\infty}\sum_{m=-k}^{k} a_{km}\frac{Y_k^m(\theta,\varphi)}{r^{k+1}}, \tag{4.13}$$

$$H(r,\theta,\varphi) = \frac{-1}{4\pi}\sum_{k=0}^{\infty}\sum_{m=-k}^{k} a_{km}\nabla\left(\frac{Y_k^m(\theta,\varphi)}{r^{k+1}}\right). \tag{4.14}$$

Equation (4.13) solves the Laplace equation for all a_{km}. On top of that, for any charge distribution that is contained within a sphere of finite radius, the potential outside that sphere can be described by the DSHF [20, p. 182]. The coefficients can be found using boundary conditions if the charge distribution is not known.

4.2. Determining Coefficients

The coefficients of the DSHE can be determined in multiple ways. If the source of the magnetic field is defined by a collection of multipoles contained within a sphere of finite radius, the coefficients can be determined analytically. In Section 4.2.1 this relation is derived for an off-centred dipole.

If the source is too complex for this method, or unknown, the coefficients can be determined by taking an inner product over a spherical surface, or by inverting a linear equation that determines the contribution of each basis function to a number of measurement points. These methods are discussed in Sections 4.2.2 and 4.2.3.

4.2.1. Analytically for an Off-Centred Dipole

For an off-centred dipole, or any finite number of dipoles, the DSHE coefficients can be determined analytically. This analytical expression can be used to check the quality of a numerical method to find these coefficients, like the methods described in Section 4.2.2 and Chapter 6.

We start by finding the coefficients for a magnetic monopole. In [14, sec. 3.6] an expansion of the Greens function $G(\mathbf{r},\tilde{\mathbf{r}}) = \frac{1}{4\pi}\frac{1}{||\mathbf{r}-\tilde{\mathbf{r}}||_2}$ is given, using $\mathbf{r} = (r,\theta,\varphi)$ and $\tilde{\mathbf{r}} = (\tilde{r},\tilde{\theta},\tilde{\varphi})$. (Note that the $\frac{4\pi}{2k+1}$ term in [14] drops out, because of the difference in definition of Y_k^m.)

$$G(\mathbf{r},\tilde{\mathbf{r}}) = \frac{1}{4\pi}\frac{1}{||\mathbf{r}-\tilde{\mathbf{r}}||_2} = \frac{1}{4\pi}\sum_{k=0}^{\infty}\sum_{m=-k}^{k}\frac{\tilde{r}^k}{r^{k+1}}Y_k^m(\tilde{\theta},\tilde{\varphi})Y_k^m(\theta,\varphi). \tag{4.15}$$

Now for the potential of a magnetic monopole of strength q at location $\tilde{\mathbf{r}}$ we get

$$\begin{aligned}\phi(r,\theta,\varphi) &= \frac{1}{4\pi}\frac{q}{||\mathbf{r}-\tilde{\mathbf{r}}||_2} && (4.16)\\ &= \frac{1}{4\pi}\sum_{k=0}^{\infty}\sum_{m=-k}^{k} q\frac{\tilde{r}^k}{r^{k+1}}Y_k^m(\tilde{\theta},\tilde{\varphi})Y_k^m(\theta,\varphi) && (4.17)\\ &= \frac{1}{4\pi}\sum_{k=0}^{\infty}\sum_{m=-k}^{k}\left(q\,\tilde{r}^k\,Y_k^m(\tilde{\theta},\tilde{\varphi})\right)\frac{Y_k^m(\theta,\varphi)}{r^{k+1}}. && (4.18)\end{aligned}$$

So for a magnetic monopole of strength q at location $\tilde{\mathbf{r}}$ we get $a_{km}^{(0)} = q\,\tilde{r}^k\,Y_k^m(\tilde{\theta},\tilde{\varphi})$

Now by Equation (2.35) we get that for a dipole of strength $\mathbf{m}$ at location $\tilde{\mathbf{r}}$:

$$\phi(r,\theta,\varphi) = \frac{1}{4\pi}\sum_{k=0}^{\infty}\sum_{m=-k}^{k} \mathbf{m}\cdot\nabla_{\tilde{\mathbf{r}}}\,\frac{1}{q}a_{km}^{(0)}(\tilde{\mathbf{r}})\frac{Y_k^m(\theta,\varphi)}{r^{k+1}}. \tag{4.19}$$

We can now define the coefficients for one off-centred dipole by:

$$a_{km}^{(1)} = \mathbf{m}\cdot\nabla_{\tilde{\mathbf{r}}}\frac{1}{q}a_{km}^{(0)}(\tilde{\mathbf{r}}) = \mathbf{m}\cdot\nabla_{\tilde{\mathbf{r}}}(\tilde{r}^k\,Y_k^m(\tilde{\theta},\tilde{\varphi})). \tag{4.20}$$

This allows us to write the potential as:

$$\phi(r,\theta,\varphi) = \frac{1}{4\pi}\sum_{k=0}^{\infty}\sum_{m=-k}^{k} a_{km}^{(1)}\frac{Y_k^m(\theta,\varphi)}{r^{k+1}}. \tag{4.21}$$

So for n dipoles of magnitude $\mathbf{m}_1,...,\mathbf{m}_n$ at locations $\tilde{\mathbf{r}}_1,...,\tilde{\mathbf{r}}_n$ with $\tilde{\mathbf{r}}_i = (\tilde{r}_i,\tilde{\theta}_i,\tilde{\varphi}_i)$, the DSHE coefficients are defined as:

$$a_{km} = \sum_{i=1}^{n}\mathbf{m}_i\cdot\nabla_{\tilde{\mathbf{r}}_i}(\tilde{r}_i^k\,Y_k^m(\tilde{\theta}_i,\tilde{\varphi}_i)). \tag{4.22}$$

4.2.2. By Taking an Inner Product over a Spherical Surface

Both for a known (or measurable) magnetic scalar potential ϕ and a known (or measureable) magnetic field $\mathbf{H}$, one can find the coefficients of the DSHE by taking inner products over a spherical surface surrounding the sources. We now give a derivation for the case of ϕ.

Recall Equation (4.13), multiply it by $Y_{k'}^{m'}$, and integrate over a sphere of radius r:

$$\int_{\partial B_r(\mathbf{0})}\phi(r,\theta,\varphi)Y_{k'}^{m'}(\theta,\varphi)\mathrm{d}A = \int_{\partial B_r(\mathbf{0})}\frac{1}{4\pi}\sum_{k=0}^{\infty}\sum_{m=-k}^{k} a_{km}\frac{Y_k^m(\theta,\varphi)}{r^{k+1}}Y_{k'}^{m'}(\theta,\varphi)\mathrm{d}A \tag{4.23}$$

$$= \frac{1}{4\pi}\sum_{k=0}^{\infty}\sum_{m=-k}^{k}\frac{a_{km}}{r^{k+1}}\int_{\partial B_r(\mathbf{0})}Y_k^m(\theta,\varphi)Y_{k'}^{m'}(\theta,\varphi)\mathrm{d}A. \tag{4.24}$$

We now use the fact that the Spherical Harmonic functions are orthogonal on spheres, and therefore

$$\int_{\partial B_r(\mathbf{0})}Y_k^m(\theta,\varphi)Y_{k'}^{m'}(\theta,\varphi)\mathrm{d}A = r^2C_{km}\delta_{kk'}\delta_{mm'}, \tag{4.25}$$

with $r^2C_{km} = \int_{\partial B_r(\mathbf{0})}(Y_k^m(\theta,\varphi))^2\mathrm{d}A$. For a_{km} we now get:

$$a_{km} = \frac{4\pi\,r^{k-1}}{C_{km}}\int_{\partial B_r(\mathbf{0})}\phi(r,\theta,\varphi)Y_k^m(\theta,\varphi)\mathrm{d}A. \tag{4.26}$$

A similar derivation can be performed for $\mathbf{H}$. However, as taking measurements on a spherical surface outside the sources can be challenging in reality, we focus on how to use measurements at arbitrary places outside de Brillouin sphere.

4.2.3. By Inverting a System of Contributions per Basis Function

The method described in Section 4.2.2 needs measurements of ϕ (or $\mathbf{H}$) on many points of a spherical surface surrounding the sources. A more convenient method, is now introduced. The measurements still need to be outside of the Brillouin sphere, but they do not need to be well distributed or on a sphere.

We know that the magnetic field at location $\mathbf{r_i} = (r_i, \theta_i, \varphi_i)$ outside the BS is defined by Equation (4.14). Suppose we want to approximate the field up to order $k_{\max}$, we can then truncate the equation to get

$$H(\mathbf{r}_i) = \frac{-1}{4\pi} \sum_{k=0}^{k_{\max}} \sum_{m=-k}^{k} a_{km} \nabla \left(\frac{Y_k^m(\theta_i, \varphi_i)}{r_i^{k+1}} \right). \tag{4.27}$$

We now construct a matrix A, that contains the contribution of the j'th basis vector to the i'th location in the $i'th$ direction $\hat{\mathbf{n}}_i$. The entries of A become:

$$A_{ij} = \frac{-1}{4\pi} \nabla \left(\frac{Y_{k(j)}^{m(j)}(\theta_i, \varphi_i)}{r_i^{k(j)+1}} \right) \cdot \hat{\mathbf{n}}_i. \tag{4.28}$$

We now define $\mathbf{x}$ as the vector containing the $k_{\max}(2 + k_{\max})$ coefficients a_{km}, and $\mathbf{b}$ as the vector containing the N measurements at locations $\mathbf{r}$ in directions $\hat{\mathbf{n}}_i$:

$$\mathbf{x} = \begin{pmatrix} a_{1,-1} \\ a_{1,0} \\ a_{1,1} \\ \vdots \\ a_{k_{\max},k_{\max}} \end{pmatrix}, \qquad \mathbf{b} = \begin{pmatrix} \mathbf{H}(\mathbf{r}_1) \cdot \hat{\mathbf{n}}_1 \\ \mathbf{H}(\mathbf{r}_2) \cdot \hat{\mathbf{n}}_2 \\ \mathbf{H}(\mathbf{r}_3) \cdot \hat{\mathbf{n}}_3 \\ \vdots \\ \mathbf{H}(\mathbf{r}_N) \cdot \hat{\mathbf{n}}_N \end{pmatrix}. \tag{4.29}$$

We can now invert $A\mathbf{x} = \mathbf{b}$ to find the DSHE coefficients. A similar system can be set up to find the coefficients with measurements of ϕ.

In this section it has been stated that the measurements of the magnetic field, need to be performed outside of the Brillouin sphere. In Section 4.3 it is discussed why.

4.3. Convergence Behaviour

Convergence of the Decreasing Spherical Harmonic Expansion is not self-evident everywhere. The Brillouin sphere has been mentioned earlier in this thesis, but to discuss the region of convergence, we introduce it more formally.

Suppose we have an arbitrary distribution of magnetic sources, that is contained within a bounded region. Then the Brillouin sphere is the smallest sphere surrounding all sources. Figure 4.1 gives an illustration of the situation. S is the outer surface of such a bounded region, and the dashed line surrounding the red zone is the Brillouin sphere.

It is a well known result that the DSHE does converge outside the Brillouin sphere [14, p. 145]. What happens inside the Brillouin sphere is discussed in Section 4.3.1. During this thesis, a numerical analysis has been performed that confirmed the convergence of the DSHE outside the BS and its divergence within the BS. As these results merely confirm established theory, they are not included in this report.

4.3.1. Inside Brillouin Sphere

[5] investigates the convergence within the Brillouin sphere of planets and their mass density. It finds that for an infinite dimensional part of the set of all possible mass distributions within the Brillouin sphere V, the DSHE converges at no point within the Brillouin sphere. The only exceptions are contained in a subset of infinite codimension W, which indeed means $\dim(V/W) = \infty$. This subset W can still be of large or infinite dimension, but clearly one cannot assume that an arbitrary mass distribution is contained in it. Therefore it is safest to assume convergence does not occur within the Brillouin sphere.

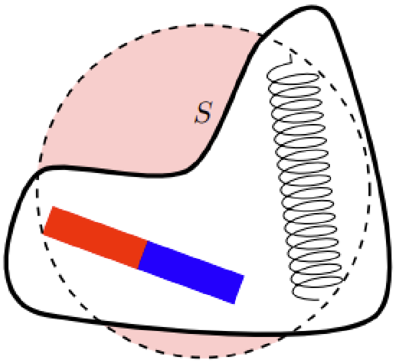

Figure 4.1: Illustration of an arbitrary surface S enclosing all magnetic sources. The red zone is the domain outside of S that is within the Brillouin sphere [6].

The above conclusion is drawn about mass distribution and gravitational potential. As the governing mathematical equations are the same in magnetostatics, we can replace the mass density by a positive (or negative) magnetic charge distribution. Lastly we can use superposition to draw the same conclusion about magnetic charge and dipole distributions.

This divergence can appear in two ways. First, coefficients found using information from outside the Brillouin sphere, that construct a converging solution outside the Brillouin sphere, result in divergence when used to describe the potential within the Brillouin sphere. Secondly, if DSHE coefficients are constructed by using information from within the Brillouin sphere, the constructed solution diverges both within and outside of the Brillouin sphere.

4.4. Issues with the DSHE

In practice, the Brillouin sphere of a source distribution can be quite large, and contain a large volume in which no sources are present. This causes issues when one wants to measure, or compute the magnetic field close to the magnetised object.

An example of this are the measurements taken on the seabed below the Albatros ship. The Brillouin sphere has a radius of approximately 18 m, while the seabed is at a depth of 13.7 m. This means some of the measurements are within the BS, and incompatible with the DSHE.

In Chapter 5 a new source model is introduced to deal with this issue. This new source model is not as efficient as the DSHE model is in computing the magnetic field, as a surface integral needs to be computed for each new point in space. In Chapter 6 a new basis for the source model is introduced, that allows us to quickly switch between the models. This means that computing the magnetic field is only costly at points within the BS.

5

Equivalent Charge or Normal Dipole Distribution on an Arbitrary Surface

In this section we derive that any distribution of sources can be replaced by a charge distribution σ, or normal dipole distribution τ on an arbitrary surface S that surrounds all sources. We do this by applying Green's second identity to the scalar magnetic ϕ and the found Green's function, for measurement points $\mathbf{r}$ outside of the surface S. We then rewrite these equations to a form that matches the magnetic scalar potential of a charge or normal dipole distribution [20, sec. 3.15].

The same derivation is then performed for points on the surface S, as the expressions derived in both in the previous and this case can be used to derive σ or τ from measurements.

After deriving the relations between the potential and σ and τ, we alter them such that we have similar expressions for $\mathbf{H}$ instead of ϕ, as we can only measure the magnetic field in reality.

Finally, the numerical implementation is discussed, and results are given. The inversion turns out to be more stable when computing σ than τ, so this part of the chapter focusses on finding σ and using it to compute $\mathbf{H}$ on the error planes from the Benchmark.

The derivations in this chapter are typical derivations using Green's identities. The equations we work towards, are from [6].

5.1. Equivalent Charge and Normal Dipole Distribution: σ and τ

The focus of this thesis, is to find an equivalent source, that leads to the same magnetic field $\mathbf{H}$ as the real magnetic source. This alternative source should be easier to find, and ideally convenient to work with. In Chapter 4 we introduced the DSHE. The DSHE offers a collection of multipoles at the centre of the expansion, as an alternative source. The issue with the DSHE though, is that it cannot be determined with measurements within the BS, or do any predictions on the magnetic field within the BS.

The equivalent sources introduced in this section, a charge distribution (CD) and a normal dipole distribution (NDD), solve this issue. Using Green's identities, one can always find the Neumann boundary conditions of the magnetic scalar potential, from the Dirichlet boundary conditions, and vice versa (up to a constant). Both the CD and NDD also capture this boundary information of the magnetic scalar potential on an arbitrary surface S surrounding all sources.

If the CD and NDD are not introduced, one would have to determine all the boundary conditions to be able to perform forward computations. The equation needed for that is derived in Section 5.2. This equation needs to be inverted to find the boundary conditions, and is used for forward computations to find the magnetic field at new points after substituting the boundary conditions in.

While performing the inversion, one should note that the magnetic scalar potential, and its normal derivative are linked together by Green's third identity, when the evaluation point is also on the arbitrary surface. So one does not need double the measurements when determining both ϕ and $\partial_{\mathbf{n}}\phi$ on S, compared to determining just ϕ.

Both the CD and NDD cleverly combine the boundary conditions and the connection between the scalar potential and its normal derivative, to form an alternative source. This source is more intuitive to work with, and allows for easier implementation of approximation methods like the multipolar expansion introduced in Chapter 6.

As the name gives away, the CD is an alternative source that consists of magnetic monopoles distributed over the arbitrary surface. These monopoles do not exist in reality, but are a convenient mathematical tool. The NDD consists of a distribution of magnetic dipoles oriented orthogonal to the surface. A physical interpretation of such a distribution does exist. Note that this makes it counter intuitive that we choose to work mostly with σ throughout this thesis. We repeat that this is due to the numerical stability of the equations that need to be inverted.

5.1.1. Introduction Example of Equivalent Sources

It may not be obvious, why we can model the ships magnetisation with an alternative source. It might feel, like we will loose information while doing this. In this section an example is given, that intuitively shows that we are able to do this, and that the information that is lost, is not essential in most cases.

For the example, we compare the magnetic field of a magnetised spherical shell, and that of a solid sphere. [14, Section 5.11] finds that the magnetic field of a solid sphere, placed in a background field $\mathbf{B}_0$ can be described by a magnetic dipole with the moment:

$$\mathbf{m}_1 = \frac{4\pi a^3}{\mu_0}\frac{\mu-\mu_0}{\mu+2\mu_0}\mathbf{B}_0, \tag{5.1}$$

where a is the radius of the sphere.

Similarly, [14, Section 5.12] finds that the magnetic field of a spherical shell, placed in a background field $\mathbf{B}_0$ can be described by a magnetic dipole with the moment:

$$\mathbf{m}_2 = \frac{4\pi(b^3-c^3)}{\mu_0}\frac{(2\mu+\mu_0)(\mu-\mu_0)}{(2\mu-\mu_0)(\mu+2\mu_0)-2\frac{c^3}{b^3}(\mu-\mu_0)^2}\mathbf{B}_0, \tag{5.2}$$

where b is the outer radius, and c is the inner radius of the spherical shell.

By varying the radii, or the magnetic permeability of the material, both spheres' magnetic field can be described by the same magnetic dipole. That is, they have the same magnetic field, if we are at a location outside of both spheres.

These now pose as alternative sources to each other. The only information we have lost is within the region of the spheres.

5.2. Green's Second Identity on S

We start by deriving a relation between the scalar magnetic potential ϕ at any point outside of the surface S, and the boundary conditions of the potential on this surface. This is done using the Green's function and Green's second identity. Recall Figure 4.1 for an illustration of the situation.

As we are still solving the Laplace equation $\nabla^2\phi = 0$, we reuse the Green's function described in Equation (2.23):

$$G(\mathbf{r},\tilde{\mathbf{r}}) = \frac{1}{4\pi}\frac{1}{||\mathbf{r}-\tilde{\mathbf{r}}||_2}. \tag{5.3}$$

In addition, we find its derivative:

$$\begin{aligned}
\partial_{\mathbf{n}(\tilde{\mathbf{r}})} G(\mathbf{r}, \tilde{\mathbf{r}}) &= \mathbf{n}(\tilde{\mathbf{r}}) \cdot \nabla_{\tilde{\mathbf{r}}} G(\mathbf{r}, \tilde{\mathbf{r}}) \\
&= \mathbf{n}(\tilde{\mathbf{r}}) \cdot -\frac{1}{4\pi} \frac{1}{||\mathbf{r} - \tilde{\mathbf{r}}||_2^2} \nabla_{\tilde{\mathbf{r}}} ||\mathbf{r} - \tilde{\mathbf{r}}||_2 \\
&= -\frac{1}{4\pi} \frac{\mathbf{n}(\tilde{\mathbf{r}})}{||\mathbf{r} - \tilde{\mathbf{r}}||_2^2} \cdot \frac{\tilde{\mathbf{r}} - \mathbf{r}}{||\mathbf{r} - \tilde{\mathbf{r}}||_2} \\
&= \frac{1}{4\pi} \frac{\mathbf{n}(\tilde{\mathbf{r}}) \cdot (\mathbf{r} - \tilde{\mathbf{r}})}{||\mathbf{r} - \tilde{\mathbf{r}}||_2^3}
\end{aligned} \tag{5.4}$$

where $\mathbf{n}(\tilde{\mathbf{r}})$ is the inward normal vector with respect to the volume containing sources.

If we now choose a volume V, around the surface S, with an exterior surface S_2, and a small spherical surface S_1 with radius r_1 to exclude the point $\mathbf{r}$ from the volume. A 2D sketch is given in Figure 5.1.

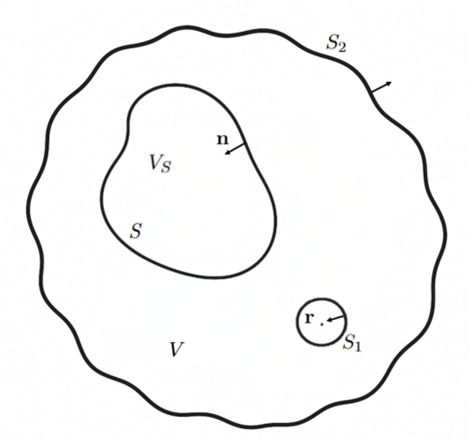

Figure 5.1: Volume V over which Green's second identity is applied. Surface S is the arbitrary surface around all source points. Surface S_1 is a spherical surface of radius r_1 around point $\mathbf{r}$. The definition of volume V_S is used in Section 5.3.

We then apply Green's second identity to the function ϕ and $G(\mathbf{r}, \tilde{\mathbf{r}})$ on volume V. We get

$$\begin{aligned}
&\int_{\tilde{\mathbf{r}} \in V} \left[G(\mathbf{r}, \tilde{\mathbf{r}}) \nabla^2 \phi(\tilde{\mathbf{r}}) - \phi(\tilde{\mathbf{r}}) \nabla^2 G(\mathbf{r}, \tilde{\mathbf{r}}) \right] \mathrm{d}V \\
&\qquad = \int_{\tilde{\mathbf{r}} \in S \cup S_1 \cup S_2} \left[G(\mathbf{r}, \tilde{\mathbf{r}}) \partial_{\mathbf{n}(\tilde{\mathbf{r}})} \phi(\tilde{\mathbf{r}}) - \phi(\tilde{\mathbf{r}}) \partial_{\mathbf{n}(\tilde{\mathbf{r}})} G(\mathbf{r}, \tilde{\mathbf{r}}) \right] \mathrm{d}S.
\end{aligned} \tag{5.5}$$

By definition, $\forall\, \tilde{\mathbf{r}} \neq \mathbf{r}$, we have $\nabla^2 G(\mathbf{r}, \tilde{\mathbf{r}}) = 0$. Also, we know $\nabla^2 \phi(\tilde{\mathbf{r}}) = 0$ holds $\forall \tilde{\mathbf{r}} \in V$. This leads to

$$\int_{\tilde{\mathbf{r}} \in S \cup S_1 \cup S_2} \left[G(\mathbf{r}, \tilde{\mathbf{r}}) \partial_{\mathbf{n}(\tilde{\mathbf{r}})} \phi(\tilde{\mathbf{r}}) - \phi(\tilde{\mathbf{r}}) \partial_{\mathbf{n}(\tilde{\mathbf{r}})} G(\mathbf{r}, \tilde{\mathbf{r}}) \right] \mathrm{d}S = 0. \tag{5.6}$$

We now let S_2 go to infinity. As all sources are within S, we know $\partial_{\mathbf{n}} \phi_\infty = 0$ and we can choose $\phi_\infty = 0$. Therefore, the integral part over S_2 has no contribution.

To solve the integral over S_1, we realise that for $\tilde{\mathbf{r}} \in S_1$, $\mathbf{n}(\tilde{\mathbf{r}}) = \frac{\mathbf{r} - \tilde{\mathbf{r}}}{||\mathbf{r} - \tilde{\mathbf{r}}||_2}$. Furthermore, we know $||\mathbf{r} - \tilde{\mathbf{r}}||_2 = r_1$. So therefore Equations (5.3) and (5.4) reduce to

$$G(\mathbf{r}, \tilde{\mathbf{r}}) = \frac{1}{4\pi} \frac{1}{r_1}, \tag{5.7}$$

$$\partial_{\mathbf{n}(\tilde{\mathbf{r}})} G(\mathbf{r}, \tilde{\mathbf{r}}) = \frac{1}{4\pi} \frac{1}{r_1^2}. \tag{5.8}$$

We get:

$$\begin{aligned}\int_{\tilde{\mathbf{r}}\in S_1} &\left[G(\mathbf{r},\tilde{\mathbf{r}})\partial_{\mathbf{n}(\tilde{\mathbf{r}})}\phi(\tilde{\mathbf{r}}) - \phi(\tilde{\mathbf{r}})\partial_{\mathbf{n}(\tilde{\mathbf{r}})}G(\mathbf{r},\tilde{\mathbf{r}})\right]\mathrm{d}S \\ &= \int_{\tilde{\mathbf{r}}\in S_1}\left[\frac{1}{4\pi}\frac{1}{r_1}\partial_{\mathbf{n}(\tilde{\mathbf{r}})}\phi(\tilde{\mathbf{r}}) - \phi(\tilde{\mathbf{r}})\frac{1}{4\pi}\frac{1}{r_1^2}\right]\mathrm{d}S. \end{aligned} \tag{5.9}$$

Now define $\overline{\phi}$ and $\overline{\partial_{\mathbf{n}}\phi}$ as the average value of ϕ and $\partial_{\mathbf{n}}\phi$ over S_1, and let $r_1 \to 0$. Then we get:

$$\begin{aligned}\lim_{r_1\to 0}\int_{\tilde{\mathbf{r}}\in S_1} &\left[\frac{1}{4\pi}\frac{1}{r_1}\partial_{\mathbf{n}(\tilde{\mathbf{r}})}\phi(\tilde{\mathbf{r}}) - \phi(\tilde{\mathbf{r}})\frac{1}{4\pi}\frac{1}{r_1^2}\right]\mathrm{d}S \\ &= \lim_{r_1\to 0}\left[\frac{1}{4\pi}\frac{1}{r_1}4\pi r_1^2\,\overline{\partial_{\mathbf{n}(\tilde{\mathbf{r}})}\phi} - \frac{1}{4\pi}\frac{1}{r_1^2}4\pi r_1^2\,\overline{\phi}\right] = -\phi(\mathbf{r}). \end{aligned} \tag{5.10}$$

Taking the above limit is allowed, as all sources are within V_S, and thus $\phi(\mathbf{r})$ and $\partial_{\mathbf{n}}\phi(\mathbf{r})$ are finite. We now use that the surface integral over S_2 has no contribution, and substitute Equation (5.10) into Equation (5.6). Similar to [6], this yields

$$\phi(\mathbf{r}) = \int_{\tilde{\mathbf{r}}\in S}\left[G(\mathbf{r},\tilde{\mathbf{r}})\partial_{\mathbf{n}(\tilde{\mathbf{r}})}\phi(\tilde{\mathbf{r}}) - \phi(\tilde{\mathbf{r}})\partial_{\mathbf{n}(\tilde{\mathbf{r}})}G(\mathbf{r},\tilde{\mathbf{r}})\right]\mathrm{d}S. \tag{5.11}$$

5.3. Defining σ and τ

The goal of this section is to show that an equivalent charge distribution $\sigma\,[\mathrm{A/m}]$, or normal dipole distribution $\tau\,[\mathrm{A}]$ can be found on the surface S, that results in the same magnetic potential outside of this surface. The magnetic potential on the inside of the surface S can be chosen freely, to help us define the alternative source. We call this potential ϕ_{in}, and as the alternative sources replace the original source it solves the Laplace equation on V_S. Therefore we now repeat the derivation from Section 5.2, but for the volume V_S within the surface S, while still keeping the point $\mathbf{r}$ within the volume V.

We again start by applying Green's second identity to $G(\mathbf{r},\tilde{\mathbf{r}})$ and $\phi_{\text{in}}(\tilde{\mathbf{r}})$. Note that we keep the direction of the normal vector $\mathbf{n}$ on S in the same inward direction, so the signs in the RHS are flipped:

$$\begin{aligned}\int_{\tilde{\mathbf{r}}\in V_S} &\left[G(\mathbf{r},\tilde{\mathbf{r}})\nabla^2\phi_{\text{in}}(\tilde{\mathbf{r}}) - \phi_{\text{in}}(\tilde{\mathbf{r}})\nabla^2 G(\mathbf{r},\tilde{\mathbf{r}})\right]\mathrm{d}V_S \\ &= \int_{\tilde{\mathbf{r}}\in S}\left[-G(\mathbf{r},\tilde{\mathbf{r}})\partial_{\mathbf{n}(\tilde{\mathbf{r}})}\phi_{\text{in}}(\tilde{\mathbf{r}}) + \phi_{\text{in}}(\tilde{\mathbf{r}})\partial_{\mathbf{n}(\tilde{\mathbf{r}})}G(\mathbf{r},\tilde{\mathbf{r}})\right]\mathrm{d}S. \end{aligned} \tag{5.12}$$

Now as $\mathbf{r}$ is outside of V_S, we know $\nabla^2 G(\mathbf{r},\tilde{\mathbf{r}}) = 0$ for $\tilde{\mathbf{r}} \in V_S$. Furthermore, as we assume that there are no sources in V_S, we have $\nabla^2\phi_{\text{in}} = 0$. We multiply by -1 and get:

$$0 = \int_{\tilde{\mathbf{r}}\in S}\left[G(\mathbf{r},\tilde{\mathbf{r}})\partial_{\mathbf{n}(\tilde{\mathbf{r}})}\phi_{\text{in}}(\tilde{\mathbf{r}}) - \phi_{\text{in}}(\tilde{\mathbf{r}})\partial_{\mathbf{n}(\tilde{\mathbf{r}})}G(\mathbf{r},\tilde{\mathbf{r}})\right]\mathrm{d}S. \tag{5.13}$$

If we now substract Equation (5.13) from Equation (5.11), we get:

$$\phi(\mathbf{r}) = \int_{\tilde{\mathbf{r}}\in S}\left[\left(\partial_{\mathbf{n}(\tilde{\mathbf{r}})}\phi(\tilde{\mathbf{r}}) - \partial_{\mathbf{n}(\tilde{\mathbf{r}})}\phi_{\text{in}}(\tilde{\mathbf{r}})\right)G(\mathbf{r},\tilde{\mathbf{r}}) - \left(\phi(\tilde{\mathbf{r}}) - \phi_{\text{in}}(\tilde{\mathbf{r}})\right)\partial_{\mathbf{n}(\tilde{\mathbf{r}})}G(\mathbf{r},\tilde{\mathbf{r}})\right]\mathrm{d}S. \tag{5.14}$$

We now try to find a CD and NDD that can create the same outside magnetic potential. This is done by choosing a boundary condition for ϕ_{in} that enforces continuity on either the potential ϕ or its normal derivative $\partial_{\mathbf{n}}$ across the surface S. Using one of these BC's, we can find the value of the undefined part (so $\partial_{\mathbf{n}}\phi$ or ϕ respectively) of ϕ_{in}.[1] Starting with the potential as a BC, we get $\phi^{\sigma}_{\text{in}}(\tilde{\mathbf{r}}) = \phi(\tilde{\mathbf{r}})$ for $\tilde{\mathbf{r}} \in S$. We can therefore simplify Equation (5.14) to:

$$\phi(\mathbf{r}) = \int_{\tilde{\mathbf{r}}\in S} \left(\partial_{\mathbf{n}}\phi(\tilde{\mathbf{r}}) - \partial_{\mathbf{n}}\phi^{\sigma}_{\text{in}}(\tilde{\mathbf{r}})\right) G(\mathbf{r},\tilde{\mathbf{r}})\mathrm{d}S. \tag{5.15}$$

As we assumed that there are no sources in the interior of V and V_s, we need to introduce sources on the surface S to satisfy the integral representation. [20, sec. 3.15] shows that this equation matches the form of the magnetic potential of a charge distribution on a surface. This CD is defined by

$$\sigma(\tilde{\mathbf{r}}) = \partial_{\mathbf{n}}\phi(\tilde{\mathbf{r}}) - \partial_{\mathbf{n}}\phi^{\sigma}_{\text{in}}(\tilde{\mathbf{r}}). \tag{5.16}$$

Similarly, if we keep the normal derivative of the potential continuous, we get $\partial_{\mathbf{n}}\phi(\tilde{\mathbf{r}}) = \partial_{\mathbf{n}}\phi^{\tau}_{\text{in}}(\tilde{\mathbf{r}})$. We can now define a normal dipole distribution as

$$\tau(\tilde{\mathbf{r}}) = \phi(\tilde{\mathbf{r}}) - \phi^{\tau}_{\text{in}}(\tilde{\mathbf{r}}) \tag{5.17}$$

to simplify the integral Equation (5.14). Here, $\phi^{\tau}_{\text{in}}(\tilde{\mathbf{r}})$ is determined up to a constant, and this constant is chosen such that $\int_{\tilde{\mathbf{r}}\in S} \tau \mathrm{d}S = 0$. We end up with two expressions for the magnetic potential in a point $\mathbf{r}$ outside the surface S [6]:

$$\phi(\mathbf{r}) = \int_{\tilde{\mathbf{r}}\in S} \sigma(\tilde{\mathbf{r}})G(\mathbf{r},\tilde{\mathbf{r}})\mathrm{d}S, \tag{5.18}$$

$$\phi(\mathbf{r}) = \int_{\tilde{\mathbf{r}}\in S} \tau(\tilde{\mathbf{r}})\partial_{\mathbf{n}(\tilde{\mathbf{r}})}G(\mathbf{r},\tilde{\mathbf{r}})\mathrm{d}S. \tag{5.19}$$

5.3.1. Resulting Magnetic Field

The derivations performed in this chapter, are easier to perform for the magnetic scalar potential. In reality, we can only measure the magnetic field $\mathbf{B}$, and indirectly $\mathbf{H}$. In this thesis, we choose to work with the Auxiliary field $\mathbf{H}$, so in this section, we derive the relations between the magnetic field outside of the arbitrary surface S, and the CD and NDD.

Recall from Equation (2.14) that $\mathbf{H} = -\nabla\phi$. If we apply this to Equations (5.18) and (5.18), we get

$$\mathbf{H}(\mathbf{r}) = -\nabla_{\mathbf{r}} \int_{\tilde{\mathbf{r}}\in S} \sigma(\tilde{\mathbf{r}})G(\mathbf{r},\tilde{\mathbf{r}})\mathrm{d}S, \tag{5.20}$$

$$\mathbf{H}(\mathbf{r}) = -\nabla_{\mathbf{r}} \int_{\tilde{\mathbf{r}}\in S} \tau(\tilde{\mathbf{r}})\partial_{\mathbf{n}(\tilde{\mathbf{r}})}G(\mathbf{r},\tilde{\mathbf{r}})\mathrm{d}S. \tag{5.21}$$

5.3.2. Existence, Unicity and Smoothness of σ and τ

To proof the existence and unicity of σ and τ, we first proof these properties for ϕ.

Existence and unicity of ϕ

In reality, for any ferromagnetic object in a magnetic background field $\mathbf{H}_0$, a unique magnetic field $\mathbf{H}$ exists on the arbitrary surface S surrounding it. Say we are able to measure the component normal to the surface S. We then have the boundary condition $\mathbf{H}(\mathbf{r}) \cdot \mathbf{n} = f(\mathbf{r})$ for the Laplace equation.

Recall that $\mathbf{H} = -\nabla\phi$, so $\mathbf{H} \cdot \mathbf{n} = -\nabla\phi \cdot \mathbf{n} = -\partial_{\mathbf{n}}\phi$. If we now pull the $-$ sign into the function f, we get the following problem:

---

[1] This can be done, as ϕ is continuous on S, $\partial_{\mathbf{n}}\phi$ is piecewise continuous on S, $\int_{\tilde{\mathbf{r}}\in S} \partial_{\mathbf{n}}\phi \mathrm{d}S = 0$ follows from Gauss' law for magnetic fields, and since S is a closed Lipschitz surface.

$$\begin{cases} \nabla^2\phi(\mathbf{r}) = 0 & \text{for } \mathbf{r} \in V, \\ \partial_{\mathbf{n}}\phi(\mathbf{r}) = f(\mathbf{r}) & \text{for } \mathbf{r} \in S = \partial V. \end{cases} \tag{5.22}$$

As $f(\mathbf{r})$ are measurements of the normal magnetic field $\mathbf{H} \cdot \mathbf{n}$, we know that $\int_S f \,\mathrm{d}S = \int_S \mathbf{H} \cdot \mathbf{n} \,\mathrm{d}S = \int_V \nabla \cdot \mathbf{H} \,\mathrm{d}V = 0$ by the Divergence theorem and Gauss' law. Therefore, by [16, Thm. 6.29] there exists a solution to problem (5.22).

We are now setup to proof that this solution is unique, up to a constant. Let u and v both solve problem (5.22). Define

$$w = u - v. \tag{5.23}$$

Then

$$\begin{cases} \nabla^2 w(\mathbf{r}) = 0 & \text{for } \mathbf{r} \in V, \\ \partial_{\mathbf{n}} w(\mathbf{r}) = 0 & \text{for } \mathbf{r} \in S = \partial V. \end{cases} \tag{5.24}$$

We now compute the energy of the difference between the solutions, and apply Green's first identity:

$$\int_V |\nabla w|^2 \,\mathrm{d}V = \int_S w \,\partial_{\mathbf{n}} w \,\mathrm{d}S - \int_V w \,\nabla^2 w \,\mathrm{d}V. \tag{5.25}$$

Now, as $\nabla^2 w(\mathbf{r}) = 0$ on V, and as $\partial_{\mathbf{n}} w(\mathbf{r}) = 0$ on S, we have $\int_V |\nabla w|^2 \,\mathrm{d}V = 0$. As $|\nabla w|^2$ is non-negative, we get

$$|\nabla w| = 0, \tag{5.26}$$

$$\iff \nabla w = 0, \tag{5.27}$$

$$\iff w = c \quad \text{for } c \in \mathbb{R}. \tag{5.28}$$

So, $u(\mathbf{r}) = v(\mathbf{r}) + c$, and indeed the solution ϕ is unique up to a constant.

When, instead of Neumann, we have Dirichlet boundary conditions, ϕ is completely unique. The existence (and uniqueness) of such a solution follows directly from [16, Thm. 6.25] without any extra conditions. The Dirichlet boundary conditions of ϕ cannot be measured in reality, and can always be shifted by a constant. The solution is then shifted by the same constant.

Existence and unicity of σ

As σ and τ, are alternative sources for the real source, we can claim there are no sources within V_S, and thus ϕ_{in} solves the Laplace equation. For σ we have that $\phi^{\sigma}_{\text{in}}(\mathbf{r}) = \phi(\mathbf{r})$ for $\mathbf{r} \in S$. Recall that the solution ϕ was known up to a constant, so the same holds for $\phi^{\sigma}_{\text{in}}$ on S.

If we now set the constant to any $c \in \mathbb{R}$ for the boundary condition of $\phi^{\sigma}_{\text{in}}$, we can solve the Laplace equation within V_S to find $\phi^{\sigma}_{\text{in}}$ on the entire region [16, Thm. 6.23]. We can now find the unique value of $\partial_{\mathbf{n}}\phi^{\sigma}_{\text{in}}$ on S, as the arbitrary constant c drops out in the differentiation.

Now, as $\partial_{\mathbf{n}}\phi^{\sigma}_{\text{in}}$ and $\partial_{\mathbf{n}}\phi$ are unique on S, we know that $\sigma = \partial_{\mathbf{n}}\phi - \partial_{\mathbf{n}}\phi^{\sigma}_{\text{in}}$ is unique as well.

Existence and unicity of τ

For τ we choose the boundary condition $\partial_{\mathbf{n}}\phi^{\tau}_{\text{in}}(\mathbf{r}) = \partial_{\mathbf{n}}\phi(\mathbf{r})$ for $\mathbf{r} \in S$. We can then find the solution ϕ^{τ}_{in} to the Laplace equation on V_S, that is unique up to a constant [16, Thm. 6.27].

We now know that ϕ^{τ}_{in} and ϕ are unique on S, up to a constant, and thus, $\tau = \phi - \phi^{\tau}_{\text{in}}$ is also unique up to a constant.

Smoothness of σ and τ

Proving smoothness properties of σ and τ in depth, is outside the scope of this thesis. However, some claims can be made.

First we define the volume V_{Alb} as the volume contained by the Albatros. Then, suppose S surrounds V_{Alb}, but does not touch it. We now choose S to be (piece-wise) smooth (for example an ellipsoid surrounding the Albatros, but not touching it). Then we know that ϕ and $\partial_{\mathbf{n}}\phi$ are (piece-wise) smooth on S, as $\phi \in C^{\infty}(\mathbb{R}^3 \setminus V_{\mathrm{Alb}})$ [9, Thm. 6].

As $\phi^{\sigma}_{\mathrm{in}}(\mathbf{r}) = \phi(\mathbf{r})$, and $\partial_{\mathbf{n}}\phi^{\tau}_{\mathrm{in}}(\mathbf{r}) = \partial_{\mathbf{n}}\phi(\mathbf{r})$ on S, we know that they are piece-wise smooth as well. Now, by [11, p. 66] we know that $\phi^{\tau}_{\mathrm{in}}$ and $\partial_{\mathbf{n}}\phi^{\sigma}_{\mathrm{in}}$ are smooth to some degree as well. Thus the same holds for σ and τ.

This derivation only holds when S does not touch V_{Alb}. However, if we assume that ϕ and $\partial_{\mathbf{n}}\phi$ are piece-wise smooth to some degree on the ships hull, we can extend the derivation to that case as well. Resulting in a piece-wise smooth σ and τ on the ships hull. Lastly, we note that this assumption is reasonable, as physical fields are generally smooth when there are no geometric or material discontinuities.

5.4. Relation of σ and τ with Measurements on S

The previous section has shown that in the volume outside of the surface S, we can compute the scalar magnetic potential using an equivalent charge or normal dipole distribution. In this section we show that the same is true for points $\mathbf{r}_S$ on the surface S. During the application of this method, measurements might be performed on, or very close to, the surface S. Therefore determining σ and τ from these measurements, needs to be done via the relation that is derived in this section.

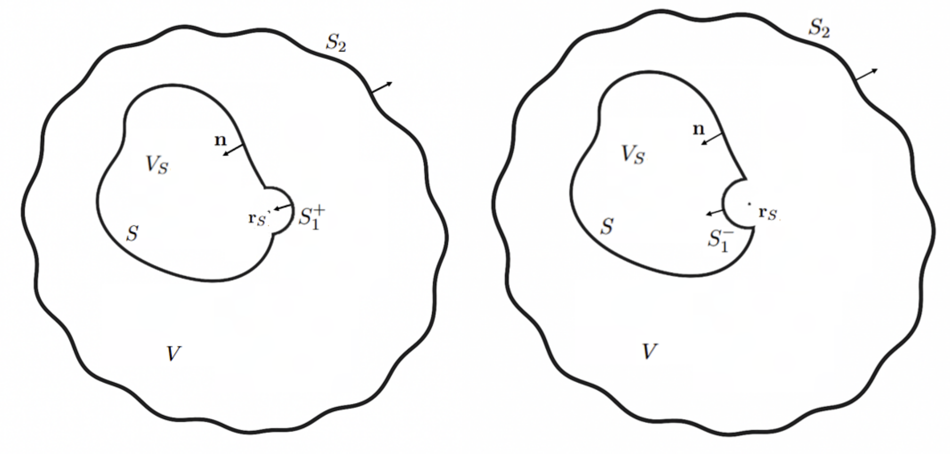

Figure 5.2: The volumes V and V_S over which Green's second identity is applied, when $\mathbf{r}_S$ is on the surface S. Surfaces S_1^+ and S_1^- are half spherical surfaces of radius r_1 around point $\mathbf{r}_S$.

We start by repeating the derivation of Section 5.2, with point $\mathbf{r}_S$ on the surface S. Again, we exclude point $\mathbf{r}_S$ from the volume. Therefore, a small circular part of the surface S is replaced by half of a spherical surface. See the left of Figure 5.2 for a 2D description.

By similar reasoning as in Section 5.2, we get to the following integral equation:

$$\int_{\tilde{\mathbf{r}} \in S \cup S_1^+} \left[G(\mathbf{r}_S, \tilde{\mathbf{r}}) \partial_{\mathbf{n}(\tilde{\mathbf{r}})} \phi(\tilde{\mathbf{r}}) - \phi(\tilde{\mathbf{r}}) \partial_{\mathbf{n}(\tilde{\mathbf{r}})} G(\mathbf{r}_S, \tilde{\mathbf{r}}) \right] \mathrm{d}S = 0. \tag{5.29}$$

Now as S_1^+ is only half of a sphere, this time, we can replace the integral over S_1^+ by the following expression:

$$\begin{aligned}\lim_{r_1\to 0}\int_{\tilde{\mathbf{r}}\in S_1^+}&\left[\frac{1}{4\pi}\frac{1}{r_1}\partial_{\mathbf{n}}\phi(\tilde{\mathbf{r}})-\phi(\tilde{\mathbf{r}})\frac{1}{4\pi}\frac{1}{r_1^2}\right]\mathrm{d}S\\ &=\lim_{r_1\to 0}\left[\frac{1}{4\pi}\frac{1}{r_1}\frac{1}{2}4\pi r_1^2\,\overline{\partial_{\mathbf{n}}\phi}-\frac{1}{4\pi}\frac{1}{r_1^2}\frac{1}{2}4\pi r_1^2\,\overline{\phi}\right]=-\frac{1}{2}\phi(\mathbf{r}_S).\end{aligned} \tag{5.30}$$

Taking the above limit is allowed if $\phi(\mathbf{r}_S)$ and $\partial_{\mathbf{n}}\phi(\mathbf{r}_S)$ are finite. Recall from Section 2.3 that in reality, ϕ solves the Laplace equation $\nabla^2\phi = 0$ everywhere. Therefore no singularities occur, and ϕ and $\partial_{\mathbf{n}}\phi$ are always finite.

Therefore, when measurements are used from real world examples, no issues occur. In our benchmark problem though, or in other mathematical examples containing singular points, we need to be mindful. The singular points are allowed to be close to the surface S, but they cannot be on it. If this is the case, ϕ and $\partial_{\mathbf{n}}\phi$ are still finite, as needed.

Assuming our system satisfies the above stated conditions, we can simplify Equation (5.29) to:

$$\frac{1}{2}\phi(\mathbf{r}_S)=\int_{\tilde{\mathbf{r}}\in S}\left[G(\mathbf{r}_S,\tilde{\mathbf{r}})\partial_{\mathbf{n}(\tilde{\mathbf{r}})}\phi(\tilde{\mathbf{r}})-\phi(\tilde{\mathbf{r}})\partial_{\mathbf{n}(\tilde{\mathbf{r}})}G(\mathbf{r}_S,\tilde{\mathbf{r}})\right]\mathrm{d}S. \tag{5.31}$$

To integrate over the volume V_S we replace the same small part of the surface S by half of a sphere in the opposite direction (which is called S_1^-). This way the point $\mathbf{r}_S$ is within the volume V and not in the surface and volume over which we integrate. See the right side of Figure 5.2 for a 2D illustration of the situation.

By similar reasoning, we get to the integral equation

$$0=\int_{\tilde{\mathbf{r}}\in S\cup S_1^-}\left[G(\mathbf{r}_S,\tilde{\mathbf{r}})\partial_{\mathbf{n}(\tilde{\mathbf{r}})}\phi_{\text{in}}(\tilde{\mathbf{r}})-\phi_{\text{in}}(\tilde{\mathbf{r}})\partial_{\mathbf{n}(\tilde{\mathbf{r}})}G(\mathbf{r}_S,\tilde{\mathbf{r}})\right]\mathrm{d}S. \tag{5.32}$$

We now focus on the part of the integral over surface S_1^-. We note that in this particular case, the normal vector $\mathbf{n}$ still points into V_S, but outward of the half sphere S_1^-, unlike the previous integrals over S_1 and S_1^+. Therefore we have

$$\partial_{\mathbf{n}(\tilde{\mathbf{r}})}G(\mathbf{r}_S,\tilde{\mathbf{r}})=-\frac{1}{4\pi}\frac{1}{r_1^2}. \tag{5.33}$$

Using the same conditions derived for the limit in Equation (5.30), we can thus replace the integral over S_1^- by:

$$\lim_{r_1\to 0}\int_{\tilde{\mathbf{r}}\in S_1^-}\left[\frac{1}{4\pi}\frac{1}{r_1}\partial_{\mathbf{n}}\phi_{\text{in}}(\tilde{\mathbf{r}})+\phi_{\text{in}}(\tilde{\mathbf{r}})\frac{1}{4\pi}\frac{1}{r_1^2}\right]\mathrm{d}S=0+\frac{1}{2}\phi_{\text{in}}(\mathbf{r}_S). \tag{5.34}$$

Which leads to

$$-\frac{1}{2}\phi_{\text{in}}(\mathbf{r}_S)=\int_{\tilde{\mathbf{r}}\in S}\left[G(\mathbf{r}_S,\tilde{\mathbf{r}})\partial_{\mathbf{n}(\tilde{\mathbf{r}})}\phi_{\text{in}}(\tilde{\mathbf{r}})-\phi_{\text{in}}(\tilde{\mathbf{r}})\partial_{\mathbf{n}(\tilde{\mathbf{r}})}G(\mathbf{r}_S,\tilde{\mathbf{r}})\right]\mathrm{d}S. \tag{5.35}$$

We now subtract Equation (5.35) from Equation (5.31), and get:

$$\frac{1}{2}(\phi(\mathbf{r}_S)+\phi_{\text{in}}(\mathbf{r}_S))=\int_{\tilde{\mathbf{r}}\in S}\left[\left(\partial_{\mathbf{n}(\tilde{\mathbf{r}})}\phi(\tilde{\mathbf{r}})-\partial_{\mathbf{n}(\tilde{\mathbf{r}})}\phi_{\text{in}}(\tilde{\mathbf{r}})\right)G(\mathbf{r}_S,\tilde{\mathbf{r}})-\left(\phi(\tilde{\mathbf{r}})-\phi_{\text{in}}(\tilde{\mathbf{r}})\right)\partial_{\mathbf{n}(\tilde{\mathbf{r}})}G(\mathbf{r}_S,\tilde{\mathbf{r}})\right]\mathrm{d}S. \tag{5.36}$$

Reusing the definition of $\sigma(\tilde{\mathbf{r}})$ we get

$$\phi(\mathbf{r}_S) = \int_{\tilde{\mathbf{r}} \in S} \sigma(\tilde{\mathbf{r}}) G(\mathbf{r}_S, \tilde{\mathbf{r}}) \mathrm{d}S, \tag{5.37}$$

just as [6]. Furthermore, by reusing the definition of $\tau(\tilde{\mathbf{r}})$ and adding $\frac{1}{2}\tau(\mathbf{r}_S) = \frac{1}{2}(\phi(\mathbf{r}_S) - \phi_{\text{in}}(\mathbf{r}_S))$ to each side of the equation, we get

$$\phi(\mathbf{r}_S) = \frac{1}{2}\tau(\mathbf{r}_S) + \int_{\tilde{\mathbf{r}} \in S} \tau(\tilde{\mathbf{r}}) \partial_{\mathbf{n}(\tilde{\mathbf{r}})} G(\mathbf{r}_S, \tilde{\mathbf{r}}) \mathrm{d}S. \tag{5.38}$$

In Chapter 7 we show how to use Equations (5.18), (5.19), (5.37), and (5.38) to find σ and τ from measurements of ϕ on or outside of the surface S.

5.4.1. Resulting Magnetic Field

We again apply $\mathbf{H} = -\nabla\phi$. This time, to Equations (5.37) and (5.38). We get:

$$\mathbf{H}(\mathbf{r}_S) = -\nabla_{\mathbf{r}_S} \int_{\tilde{\mathbf{r}} \in S} \sigma(\tilde{\mathbf{r}}) G(\mathbf{r}_S, \tilde{\mathbf{r}}) \mathrm{d}S, \tag{5.39}$$

$$\mathbf{H}(\mathbf{r}_S) = -\nabla_{\mathbf{r}_S} \left[\frac{1}{2}\tau(\mathbf{r}_S) + \int_{\tilde{\mathbf{r}} \in S} \tau(\tilde{\mathbf{r}}) \partial_{\mathbf{n}(\tilde{\mathbf{r}})} G(\mathbf{r}_S, \tilde{\mathbf{r}}) \mathrm{d}S \right]. \tag{5.40}$$

5.5. Numerical Implementation

In this section, the numerical implementation of the method discussed in this chapter, is explained. First we discuss the solution space of σ and τ is defined. We introduce that the system is underdetermined, and how this issue is solved.

Next, we explain how to compute σ on the surface S, using measurements of ϕ and measurements of $\mathbf{H}$. We also discuss whether these measurements can be on the surface S, or if they need to be outside of it. This is due to stability issues of the integrals we are inverting.

The reason we only look into σ, and not into τ, is that the integrals that need to be inverted, are even more unstable. This is due to the normal derivative of the Green's function, which contributes an extra $\frac{1}{||\mathbf{r}-\mathbf{r}_S||_2}$ term. (See Equations (5.19), (5.38), (5.21), and (5.40).)

5.5.1. Solution Space of σ and τ and Example Distributions

When solving Equations (5.18), (5.19), (5.37) or (5.38), one needs to choose in which solution space we allow σ and τ to be. A simple first choise, is to make them piecewise constant. That is, we mesh the surface S on which they are defined, and choose both σ and τ to be constant on each mesh element. Below, CD's and NDD's are plotted for the Albatros ferry. The plotted distributions are the first basis vectors for the bases that are derived in Chapter 6.

This solution space, has a very high dimension. As we are not making the measurement vector as long as this dimension, the system is underdetermined. This can lead to overfitting, and non-physical solutions of σ. Furthermore, the high dimension of the solution space, leads to high computational costs.

The fact that the system is underdetermined, is solved by finding the Least-Squares solution. That is, we find the solution:

$$\mathbf{x}_{LS} = \arg\min_{\mathbf{x}} ||A\mathbf{x} - \mathbf{b}||_2^2. \tag{5.41}$$

For now we ignore the other issues of the high dimension solutions space. We simply show how one would compute σ naively. In Section 5.6 the results of the methods in this section are given, and these issues reappear. Lastly, Section 5.6 introduces how to solve these issues.

(a) Charge distribution σ **(b)** Normal dipole distribution τ

Figure 5.3: A charge distribution and normal dipole distribution on the surface S, the outside of the Albatros ferry. The plotted distributions are the first basis vectors of the bases that are derived in Chapter 6.

5.5.2. Determining σ Using ϕ Measurements

As stated before, we choose σ to be piecewise constant. We can then write

$$\sigma(\mathbf{r}) = \sum_{j=1}^{N_e} \sigma_{e_j} \chi_{e_j}(\mathbf{r}), \tag{5.42}$$

where N_e is the number of elements on S, and

$$\chi_{e_j}(\mathbf{r}) = \begin{cases} 1 & \text{if } \mathbf{r} \in e_j, \\ 0 & \text{else,} \end{cases} \tag{5.43}$$

is the characteristic function. We interpret this as $\chi_{e_j}(\mathbf{r})$ being the N_e basis functions of which we want to find the coefficients σ_{e_j}. We are setting up a matrix vector equation to solve, and define the vector $\mathbf{x}$ as these coefficients.

The measurements of the magnetic scalar potential ϕ are at locations $\mathbf{r}_i$, that can be either on the basis surface S, or outside of it. These measurements $\phi(\mathbf{r}_i)$ form the RHS vector $\mathbf{b}$.

The entries of the matrix A now become the contribution of the basis vector $\chi_{e_j}(\mathbf{r})$ to the measurement $\phi(\mathbf{r}_i)$.

Recall that the equations that the measurements and CD need to satisfy when $\mathbf{r}_i \in S$, and when $\mathbf{r}_i \notin S$, look the same. Both Equation (5.18) and Equation (5.37) lead to the following contribution per basis vector $\chi_{e_j}(\mathbf{r})$ to the measurement $\phi(\mathbf{r}_i)$:

$$a_{ij} = \int_{\tilde{\mathbf{r}} \in S} \frac{1}{4\pi} \frac{1}{||\mathbf{r}_i - \tilde{\mathbf{r}}||_2} \chi_{e_j}(\tilde{\mathbf{r}}) \, \mathrm{d}S = \int_{\tilde{\mathbf{r}} \in e_j} \frac{1}{4\pi} \frac{1}{||\mathbf{r}_i - \tilde{\mathbf{r}}||_2} \, \mathrm{d}S. \tag{5.44}$$

Now if $\mathbf{r}_i \notin e_j$, this integral has no singular points, and can be solved or approximated in the following way:

$$a_{ij} = \frac{1}{4\pi} \frac{1}{||\mathbf{r}_i - \mathbf{r}_{e_j}||_2} w_j, \quad \text{if } \mathbf{r}_i \notin e_j, \tag{5.45}$$

where $\mathbf{r}_{e_j}$ is the centre of element e_j and w_j is its area. The analytical contribution of such a constant element can be determined [8, pp. 243-246], but has not been implemented in this thesis.

Now suppose $\mathbf{r}_i \in e_j$, then the integral in Equation (5.44) does contain a singular point. The integral still converges though, and we can use the following expression for the contribution of a square mesh-element with edge length $2a$ where $\mathbf{r} = \tilde{\mathbf{r}}$ (see Appendix A.1):

$$\int_{[-a,a]^2} \frac{1}{\sqrt{x^2+y^2}} \mathrm{d}x\mathrm{d}y = 4(2a)\ln(1+\sqrt{2}). \tag{5.46}$$

So if $\mathbf{r}_i = \mathbf{r}_{e_j}$ we get:

$$a_{ij} = 4\sqrt{w_j}\ln(1+\sqrt{2}), \quad \text{if } \mathbf{r}_i \in e_j. \tag{5.47}$$

This expression could also be used if $\mathbf{r}_{e_j} \neq \mathbf{r}_i \in e_j$, but in that case it would be an approximation. In general in this thesis, when we work with measurements on the surface S, we are able to choose $\mathbf{r}_i = \mathbf{r}_{e_j}$.

We can now find the CD, by solving $A\mathbf{x} = \mathbf{b}$ using a Least-Squares solver.

5.5.3. Determining σ Using $\mathbf{H}$ Measurements

The second method uses the measurable magnetic field $\mathbf{H}$ as input. We use the same basis vectors for σ in the matrix vector equation as in section 5.5.2. So again, our vector $\mathbf{x}$ is built up of the coefficients σ_{e_j} from Equation (5.42). Our measurement vector $\mathbf{b}$ is built up of measurements $\mathbf{H}(\mathbf{r}_i) \cdot \mathbf{e}_i$, where $\mathbf{e}_i$ are the sensor directions.

Recall from Equation (2.14) that $\mathbf{H} = -\nabla\phi$. We use this to find a relation between the $\mathbf{H}$-field and σ. By Equation (5.18) for $\mathbf{r} \notin S$ we have

$$\begin{aligned}\mathbf{H}(\mathbf{r}) = -\nabla\phi(\mathbf{r}) &= -\nabla_{\mathbf{r}} \int_{\tilde{\mathbf{r}}\in S} \sigma(\tilde{\mathbf{r}}) G(\mathbf{r},\tilde{\mathbf{r}})\,\mathrm{d}S \\ &= -\int_{\tilde{\mathbf{r}}\in S} \frac{\sigma(\tilde{\mathbf{r}})}{4\pi} \nabla_{\mathbf{r}} \frac{1}{||\mathbf{r}-\tilde{\mathbf{r}}||_2}\,\mathrm{d}S \\ &= \int_{\tilde{\mathbf{r}}\in S} \frac{\sigma(\tilde{\mathbf{r}})}{4\pi} \frac{\mathbf{r}-\tilde{\mathbf{r}}}{||\mathbf{r}-\tilde{\mathbf{r}}||_2^3}\,\mathrm{d}S. \end{aligned} \tag{5.48}$$

Similar to the relation in 5.5.2, we now define the matrix entries by the contribution per basis vector χ_{e_j} to the measurement $\mathbf{H}(\mathbf{r}_i) \cdot \mathbf{e}_i$:

$$a_{ij} = \int_{\tilde{\mathbf{r}}\in S} \frac{1}{4\pi} \frac{(\mathbf{r}_i-\tilde{\mathbf{r}})\cdot\mathbf{e}_i}{||\mathbf{r}_i-\tilde{\mathbf{r}}||_2^3} \chi_{e_j}(\tilde{\mathbf{r}})\,\mathrm{d}S = \int_{\tilde{\mathbf{r}}\in e_j} \frac{1}{4\pi} \frac{(\mathbf{r}_i-\tilde{\mathbf{r}})\cdot\mathbf{e}_i}{||\mathbf{r}_i-\tilde{\mathbf{r}}||_2^3}\,\mathrm{d}S. \tag{5.49}$$

We can again approximate this equation by

$$a_{ij} = \frac{1}{4\pi} \frac{(\mathbf{r}_i-\mathbf{r}_{e_j})\cdot\mathbf{e}_i}{||\mathbf{r}_i-\mathbf{r}_{e_j}||_2^3} w_j. \tag{5.50}$$

The equation above contains a $\frac{1}{||\mathbf{r}-\mathbf{r}_{e_j}||_2^2}$ term. So even though we have $\mathbf{r}_i \neq \mathbf{r}_{e_j} \quad \forall i,j$, inverting the integral equation is numerically less stable.

Recall that Equation (5.39) for $\mathbf{r} \in S$ is the exact same as Equation (5.20) for $\mathbf{r} \notin S$. So the same derivation can be performed for that case, and we would also end up with Equation (5.49) but for each $\mathbf{r}_i \in S$, there is one element e_j, such that $\mathbf{r}_i \in e_j$. So then the integral in Equation (5.49) contains a singular point. Instead of proving that this integral converges or diverges, we decide that for the scope of this thesis, the outcome would be too unstable to work with regardless. Therefore we avoid measurements of $\mathbf{H}$ on S in this thesis, and only consider measurements outside of S.

The CD σ is now again found by solving the matrix vector equation $A\mathbf{x} = \mathbf{b}$, using a Least-Squares solver.

5.6. Results

In this section, the results of the implementations explained in Section 5.5 are given. We first look at the results of finding σ using measurements outside of the surface S. Since we cannot measure ϕ in reality, we only use measurements of $\mathbf{H}$. We find that the method works well in predicting the magnetic field on the error-surfaces, but that overfitting can occur, leading to non-physical σ. We propose to solve this by reducing the solution space of σ. A method to do this, is introduced in Chapter 6.

Next, we look at the results of finding σ with measurements on S. Because of the $1/||\mathbf{r} - \mathbf{r}_S||_2$ terms within the integrals that are inverted, this poses larger numerical challenges. We only investigate this method using measurements of ϕ, as this makes these numerical challengers slightly easier. We find that using measurements on S is not feasible with our current implementation.

Therefore, from Chapter 6 onwards, we only use measurements outside of S. These measurements are also only of the magnetic field $\mathbf{H}$.

5.6.1. Using Measurements Outside of S

In reality, only the magnetic field can be measured, so for this section, we only plot the results of using the magnetic field as input to our RHS vector $\mathbf{b}$ as defined in Section 5.5.3. The measurements are taken on the box from Figure 3.1. We find σ according to Section 5.5.3, once using all of the 470 measurement locations, and once using only 50. At each measurement location we measure $\mathbf{H}$ in three directions, so N_{meas} is three times that number. The system remains underdetermined as the number of elements on S is 6002. This issue is resolved by using a Least-Squares solver. Figure 5.4 shows the found σ's:

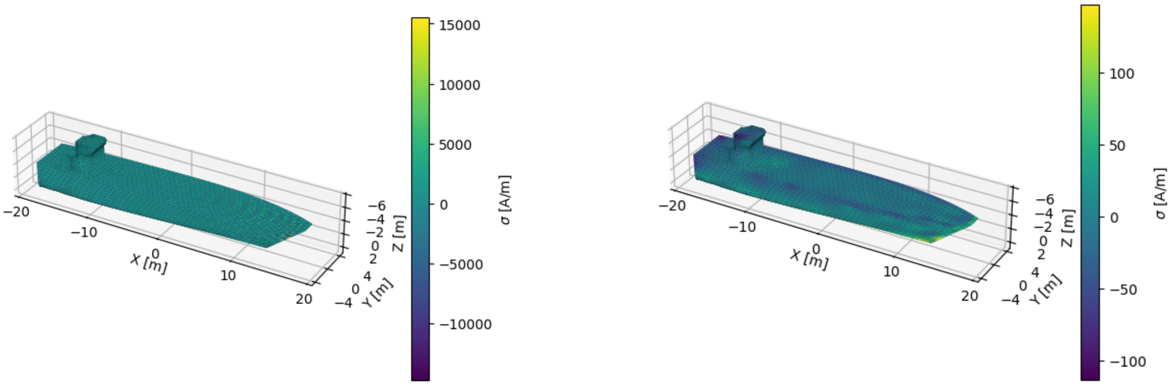

(a) $N_{\text{meas}} = 1410$

(b) $N_{\text{meas}} = 150$

Figure 5.4: equivalent charge distribution σ on the surface S, the outside of the Albatros ferry. The CD σ of both figures was found using the method described in Section 5.5.3. The N_{meas} measurements were taken on the box shaped surface of Figure 3.1. The used magnetic background field was $\mathbf{B}_0 = (23.360, 0, 41.234)\,\mu\text{T}$.

As the system is very underdetermined, overfitting can occur. Probably, this causes the high-variance behaviour on the corners of the ship in Figure 5.4a. Recall from Equation (5.16), that σ is based on the physical value $\partial_{\mathbf{n}}\phi = \mathbf{H} \cdot \mathbf{n}$ on S. Therefore we do not expect such a high-variance, and thus non-physical, solution.

If overfitting occurs in 5.4b, it is less visible, probably due to the measurement points being spread out well across the box from Figure 3.1. If the found σ is not realistic, and does overfit on the measurement data, the CD does not need to take as much extreme values to fit all the data. Therefore it looks more reasonable.

Using the found σ's, we can now compute the magnetic field on the error surfaces depicted in Figure 3.2. For this we use Equation (5.20). The result on the plane partially within the BS is given in Figure 5.5.

We see that both σ's yield good approximations of the magnetic field on the error plane. To zoom in on the effects of varying N_{meas}, we compute the NRMSE for varying N_{meas}. We do this on both error planes introduced in Section 3.1.2. The error that is plotted is a normed RMSE:

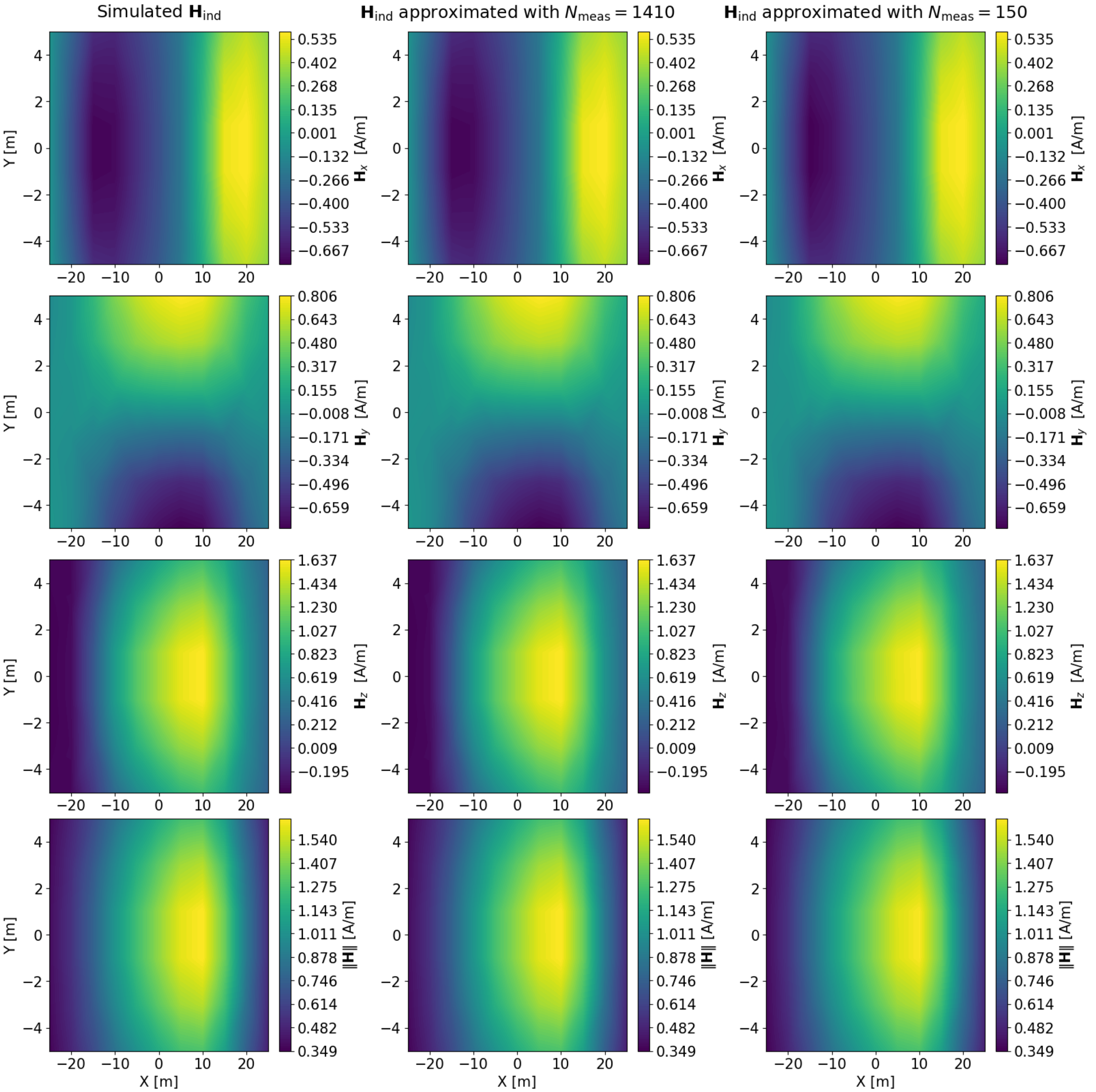

Figure 5.5: Induced magnetic field $\mathbf{H}_{\mathrm{ind}}$ computed with two different σ's, compared to the simulated data computed with the MoM. The CD σ of both columns was found using the method described in Section 5.5.2. For the second column, $N_{\mathrm{meas}} = 1410$ measurements were used, and for the third $N_{\mathrm{meas}} = 150$. The measurements were taken on the box shaped surface of Figure 3.1. The rows show the different components of $\mathbf{H}_{\mathrm{ind}}$, and its norm. The used magnetic background field was $\mathbf{B}_0 = (23.360, 0, 41.234)\,\mu\mathrm{T}$. The magnetic field was evaluated on the error plane partially within the BS and below the ship like in Figure 3.2.

$$\mathrm{NRMSE} = \sqrt{\frac{\frac{1}{N_e}\sum_{i=1}^{N_e} ||\mathbf{H}_i - \hat{\mathbf{H}}_i||_2^2}{\max_i ||\mathbf{H}_i||_2^2}}. \tag{5.51}$$

Here N_e is the number of points on which the error is computed. The results are given in Figure 5.6.

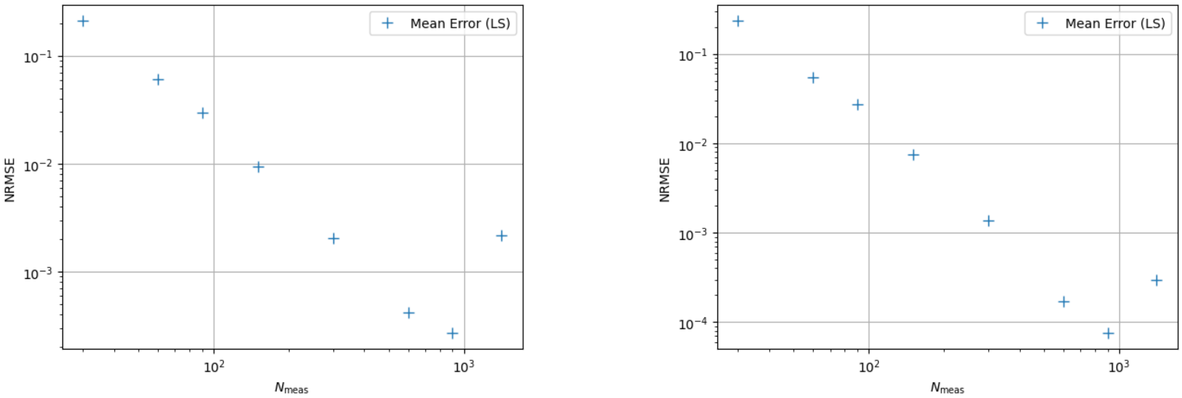

(a) NRMSE on the error plane partially within the BS.

(b) NRMSE on the error plane outside the BS.

Figure 5.6: The NRMSE of the magnetic field $\mathbf{H}_{\mathrm{ind}}$ according to Equation (5.51), plotted against the varied number of measurements N_{meas}. The CD σ was found using the method in Section 5.5.3. The N_{meas} measurements were taken on the box of Figure 3.1. The used magnetic background field was $\mathbf{B}_0 = (23.360, 0, 41.234)$ μT. The NRMSE was computed on the error planes below the ship like in Figure 3.2. We sample the measurement points and compute the NRMSE 30 times. The mean value is given in the figures.

A clear decrease in the NRMSE is visible when N_{meas} is increased. However, in Figure 5.4a we saw that a high N_{meas} can lead to overfitting and non-physical σ's. We want to be able to achieve better solutions by adding more measurements. A way to do this, and avoid the overfitting, is by decreasing the solution space of σ. Chapter 6 goes into how this can be done.

5.6.2. Using Measurements On S

As stated in Section 5.5.3, Equation (5.49) is hard to solve when the measurement points are on the surface S. In future research, one could try to find a numerically stable way to solve this integral equation. In this thesis however, we focus on measurements of $\mathbf{H}$ outside of the surface S.

For measurements of ϕ, we are able to invert the equation reasonably well. Recall that in Equation (5.47), we found an analytical expression for the contribution of a mesh element, to the measurement on that element. As the MoM does not return the magnetic potential, for this section we use the dipole model of the Albatros, introduced in Section 3.1.3.

As the dipoles are very close to the outer surface of the ship, measuring the potential on that surface leads to large numerical instabilities. Therefore, we shift the arbitrary surface, to the box-shaped measurement surface from Section 3.1.2. We let the surface consist of 6120 mesh elements, similar to the ships hull. We measure ϕ at 1410 locations on the box-shaped surface.

We now solve the system derived in Section 5.5.2, using a Least-Squares solver. Using the found σ we compute the induced magnetic field $\mathbf{H}_{\mathrm{ind}}$ on the evaluation surface within the BS. To be able to do a good comparison with the results in Section 5.6.1, we also compute $\mathbf{H}_{\mathrm{ind}}$ using the same measurements of ϕ, but using the ships hull as S. That is, the measurements for the are outside of S. The results are given in Figure 5.7.

In Section 3.1.3 we concluded that the dipole model is a good model for the Albatros, only outside of the BS. The reason we still evaluate the magnetic field within the BS in Figure 5.7, is that the method we are testing, should also work for the dipole model. Clearly, the tested method does not work well.

We check whether this issue might be resolved by using more measurement points, we compute the NRMSE for varying N_{meas}. We do this for measurements of ϕ on and outside of S (by changing the location of S), and for measurements of $\mathbf{H}$ outside of S. The result is given in Figure 5.8.

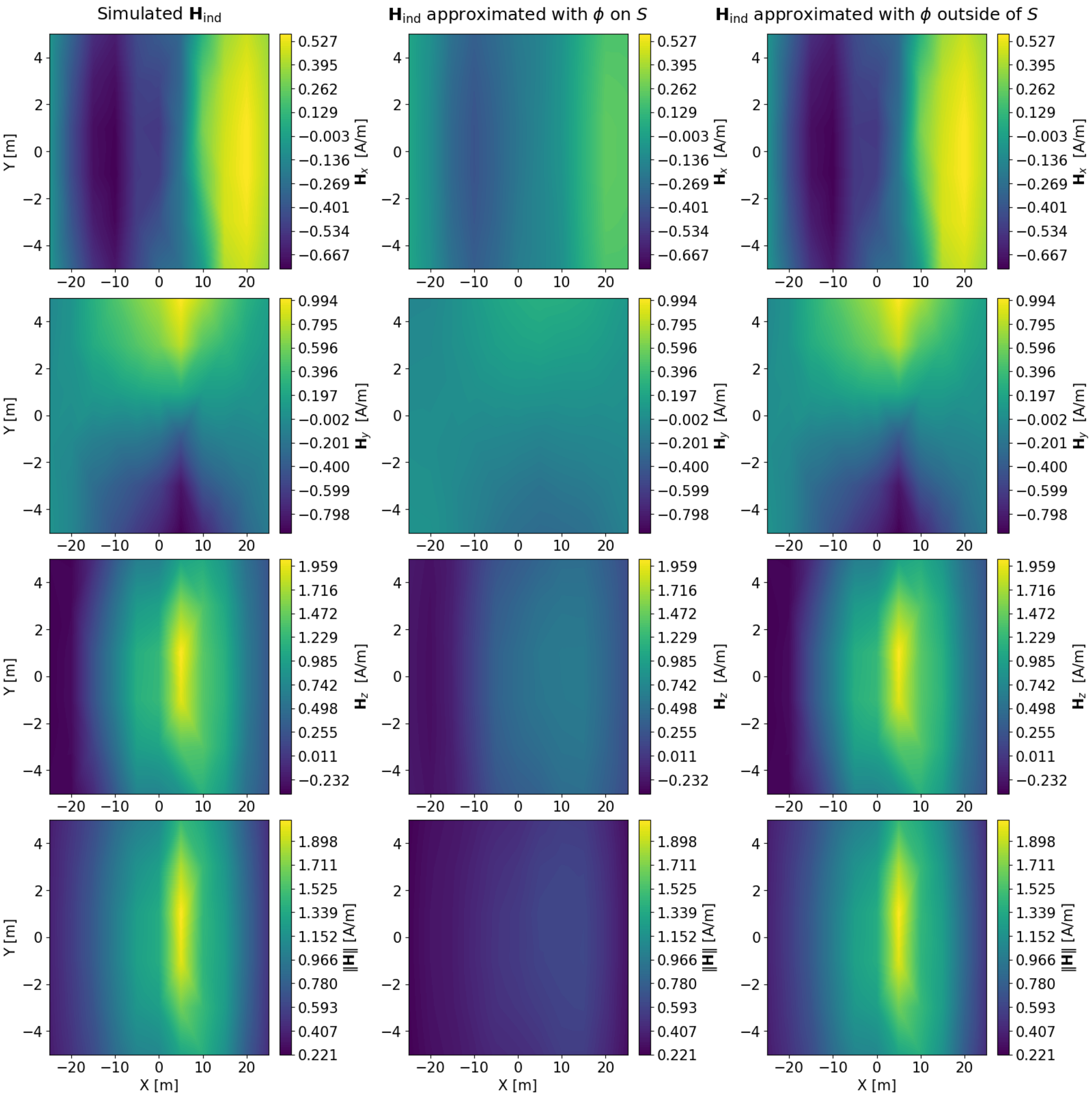

Figure 5.7: Induced magnetic field $\mathbf{H}_{\text{ind}}$ computed with two different σ's, compared with the dipole model from Section 3.1.3. The CD σ of both columns was found using the method described in Sections 5.5.2. For the second column, σ was defined on the box shaped surface on which all measurements are taken as well. For the third column, σ was defined on the outside of the ship. The $N_{\text{meas}} = 1410$ measurements were taken on the box shaped surface of Figure 3.1. The rows show the different components of $\mathbf{H}_{\text{ind}}$, and its norm. The used magnetic background field was $\mathbf{B}_0 = (23.360, 0, 41.234)\,\mu\text{T}$. The magnetic field was evaluated on the error plane partially within the BS and below the ship like in Figure 3.2.

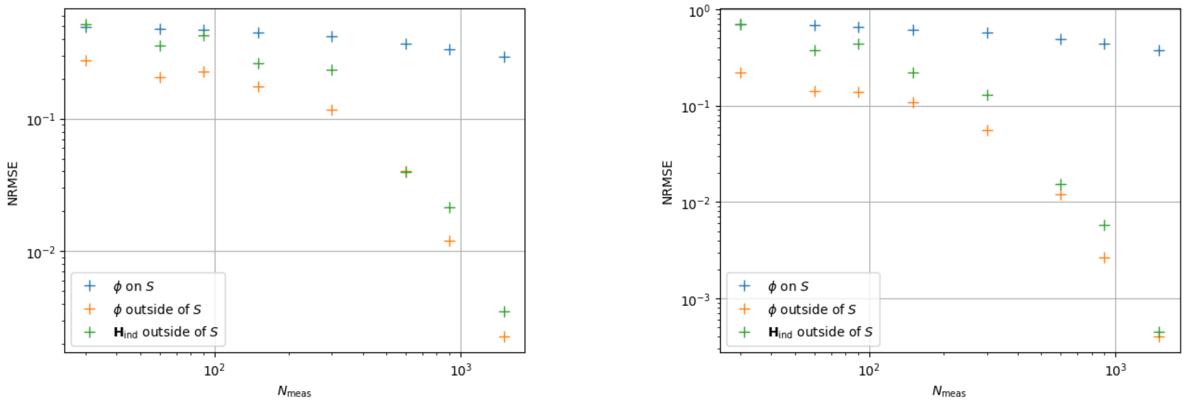

(a) NRMSE on the error plane partially within the BS.

(b) NRMSE on the error plane outside the BS.

Figure 5.8: The NRMSE of the magnetic field $\mathbf{H}_{\text{ind}}$ according to Equation (5.51), plotted against the varied number of measurements N_{meas}. The CD σ was found using the methods described in Sections 5.5.2 and 5.5.3. The surface S on which σ lives, is the outside of the ship for the orange and green points. For the blue points, it is the box on which the measurements were taken as well. The N_{meas} measurements were taken on the box of Figure 3.1. The used magnetic background field was $\mathbf{B}_0 = (23.360, 0, 41.234)\,\mu\text{T}$. The NRMSE was computed on the error planes below the ship like in Figure 3.2. We sample the measurement points and compute the NRMSE 30 times. The mean value is given in the figures.

By comparing the NRMSE of the σ computed on the ships hull, with $\mathbf{H}$ measurements, to that in Figure 5.6, we see that finding the correct σ is harder for the dipole model, than for the geometry put into the MoM. The NRMSE is namely larger for the dipole model. Recall that this result is in accordance with the hypothesis from Section 3.1.1. The hypothesis stated that finding an alternative source on S for a magnetisation close to S, might be easier than doing the same for a source within S, such as a magnetised core, or a dipole. Whether this result is indeed caused by the unproved hypothesis, is outside of the scope of this thesis.

If we compare the results within Figure 5.8, we clearly see that measurements of $\mathbf{H}$ outside of S, yield better results than measurements of ϕ on S. We also see, that using more measurements of ϕ on S, does not improve the results much. Therefore, increasing N_{meas} even more would probably not resolve the issue. Furthermore, we see that using ϕ measurements outside of S, performs even better than $\mathbf{H}$ measurements outside of S. This is as expected, due to extra $1/||\mathbf{r} - \mathbf{r}_S||_2$ term and its resulting numerical instabilities.

Investigating how to solve the issues with measurements of ϕ on S, is outside of the scope of this thesis. One could continue this research in future work, but this should not be a priority, as using measurements of ϕ is not possible in reality, and the numerical instabilities will only increase when one uses measurements of $\mathbf{H}$ on S.

From now on, we continue only using measurements of $\mathbf{H}$ outside of S. The measurements are allowed to be close to S, but one should be careful about the numerical instabilities that are caused by this.

5.7. Overfitting and Computational Costs

Besides the overfitting that occurs due to the high degree of freedom of σ, there is a high computational cost tied to the current solution space of σ. This is the case both when one computes σ, as well as when we use σ to compute the magnetic field at a new location.

Recall that we defined σ to be piecewise constant on S. Therefore, the solution space of σ has a dimension as large as the number of elements in S. This solution space also contains many non-physical solutions, as it pays no regards to the smoothness of σ. Lowering the dimension of the solution space in a way that cuts out many non-physical solutions, would be a great next step.

To determine the magnetic field at any point $\mathbf{r}$ outside of S, we need to evaluate Equation (5.20). Recall from Section 4.3, that the DSHE performs very well outside of the BS, and has low computational costs for computing $\mathbf{H}$ at a new point. Being able to link the basis of σ to the DSHE, would be a great next step to lower the computational cost in the forward computations.

Chapter 6 introduces a basis which satisfies both of these conditions.

6

Finding a Multipolar Basis on an Arbitrary Surface

Chapter 5 introduces two equivalent sources, and a solution space (or basis) to describe them in. We chose to let σ and τ live in the piecewise constant solution space. One can find good solutions within this solution space, however a lot of measurements are needed to find these solutions. Otherwise the system can be unstable and underdetermined.

Another downside of the solution space from Chapter 5, is that it has a high dimension. Therefore, finding the solutions, and using the solutions to perform further computations, have a high computational cost.

As the DSHE has a very low computational cost to compute the magnetic field at any point outside the BS, we want to find a relation between the CD or NDD solutions, and the DSHE coefficients. Therefore, in this chapter, we find a basis of a smaller size, that can easily be linked to the DSHE. This basis and method were proposed in [6]. We follow the structure of the paper closely, but adapt and extend where needed for this thesis.

We call the newly derived basis a multipolar basis on surface S, as it is a version of the multipolar basis of the DSHE that is mapped onto the surface S. The goal of this chapter is to derive bases of σ and τ that satisfy these conditions. With such bases, we get:

$$\sigma(\mathbf{r}) = \sum_{k=1}^{\infty} \sum_{m=-k}^{k} c_{km} \sigma_{km}(\mathbf{r}), \tag{6.1}$$

$$\tau(\mathbf{r}) = \sum_{k=1}^{\infty} \sum_{m=-k}^{k} c_{km} \tau_{km}(\mathbf{r}), \quad \text{for } \mathbf{r} \in S, \tag{6.2}$$

where the c_{km} are the coefficients of the multipolar basis on S. The basis functions σ_{km} and τ_{km} cause the same magnetic field, and thus use the same coefficients c_{km}. The double indexing is a result of the mapping from the double indexed DSHE.

As the basis is built from mapping the DSHE on the surface S, it turns out that by orthogonalising the basis in a clever way, the multipolar basis on S can have a similar ordering as the DSHE. This similar ordering means that the potential outside the BS, produced by the k'-th order basis vectors σ_{km} and τ_{km}, satisfies a decreasing law of at least $1/r^{k+1}$. Precisely as the k'-th order term of the DSHE in Equation (4.13). This condition can be written as:

$$a_{k'm'}[\sigma_{km}] = a_{k'm'}[\tau_{km}] = 0 \quad \text{if } k' < k, \tag{6.3}$$

following the construction proposed in [6]. This chapter derives the multipolar bases of the equivalent sources, that satisfy this condition.

Non-Orthogonal Bases

We note that orthogonalising the found basis is not necessary for many of the steps in this thesis. In [6] and [7] no clear reason is given for orthogonalisation. As these papers do use an orthogonalised basis, we follow this setup for the main part of this thesis. However, we do investigate the option of using a non-orthogonal basis. This chapter goes into finding a multipolar basis, and orthogonalising it. In Section 7.4 we repeat the relevant equations that still hold for a non-orthogonal basis. We then compare the results of the non-orthogonal basis to the results from that chapter. In Section 8.5 we compare the application of Bayesian inference on the non-orthogonal basis, with the application on the orthogonal basis.

6.1. Defining an Initial Basis and Inner Product

To reach the goal described above, we start by linking the Spherical Harmonics coefficients to any CD σ or NDD τ on the surface. We do this by expressing the Green's function in spherical coordinates, and filling it into Equations (5.18) and (5.19). Recall from Equation (4.15) that if we choose $\mathbf{r} = (r, \theta, \varphi)$ and $\tilde{\mathbf{r}} = (\tilde{r}, \tilde{\theta}, \tilde{\varphi})$ such that $r > \tilde{r}$, the Green's function becomes:

$$G(\mathbf{r}, \tilde{\mathbf{r}}) = \frac{1}{4\pi} \frac{1}{||\mathbf{r} - \tilde{\mathbf{r}}||_2} = \frac{1}{4\pi} \sum_{k=0}^{\infty} \sum_{m=-k}^{k} \frac{\tilde{r}^k}{r^{k+1}} Y_k^m(\tilde{\theta}, \tilde{\varphi}) Y_k^m(\theta, \varphi). \tag{6.4}$$

Inserting this into Equation (5.18) yields

$$\begin{aligned}\phi(\mathbf{r}) &= \int_{\tilde{\mathbf{r}} \in S} \sigma(\tilde{\mathbf{r}})\, G(\mathbf{r}, \tilde{\mathbf{r}})\, \mathrm{d}S \\ &= \frac{1}{4\pi} \sum_{k=0}^{\infty} \sum_{m=-k}^{k} \left[\int_{\tilde{\mathbf{r}} \in S} \tilde{r}^k Y_k^m(\tilde{\theta}, \tilde{\varphi})\, \sigma(\tilde{\mathbf{r}})\, \mathrm{d}S \right] \frac{Y_k^m(\theta, \varphi)}{r^{k+1}}.\end{aligned} \tag{6.5}$$

Recall that we want to find a relation between the basis on S and the DSHE. We can do this by writing the potential as a DSHE like in Equation (4.13). If we write

$$a_{km}[\sigma] = \int_S r^k Y_k^m(\theta, \varphi)\, \sigma(\mathbf{r})\, \mathrm{d}S, \tag{6.6}$$

this is exactly the case.

A similar result can be obtained for τ. We plug Equation (6.4) into Equation (5.19) to get:

$$\begin{aligned}\phi(\mathbf{r}) &= \int_{\tilde{\mathbf{r}} \in S} \tau(\tilde{\mathbf{r}})\, \partial_{\mathbf{n}(\tilde{\mathbf{r}})} G(\mathbf{r}, \tilde{\mathbf{r}})\, \mathrm{d}S \\ &= \frac{1}{4\pi} \sum_{k=0}^{\infty} \sum_{m=-k}^{k} \left[\int_{\tilde{\mathbf{r}} \in S} \partial_{\mathbf{n}(\tilde{\mathbf{r}})} \left(\tilde{r}^k Y_k^m(\tilde{\theta}, \tilde{\varphi}) \right) \tau(\tilde{\mathbf{r}})\, \mathrm{d}S \right] \frac{Y_k^m(\theta, \varphi)}{r^{k+1}}.\end{aligned} \tag{6.7}$$

So we find:

$$a_{km}[\tau] = \int_S \partial_{\mathbf{n}} \left(r^k Y_k^m(\theta, \varphi) \right) \tau(\mathbf{r})\, \mathrm{d}S. \tag{6.8}$$

Note, that Equations (6.6) and (6.8) hold for any CD and NDD, and thus also for any basis of σ and τ.

Since the integrals in (6.6) and (6.8) are taken over the closed surface S, it feels natural to interpret them as inner products on S. If the surface were spherical, and the potential ϕ on this surface was known, a similar inner product could be taken, as described in Section 4.2.2. In the setting of the arbitrary surface S, we are using the CD σ or NDD τ instead of the potential.

Furthermore, in the spherical case, the basis vectors Y_k^m occur within the inner product. In the arbitrary surface case, this term is replaced by the terms $r^k\,Y_k^m(\theta,\varphi)$ and its normal derivative. We therefore introduce these terms, following [6], as (non-orthogonal) initial bases for σ and τ:

$$\sigma^0_{km}(r,\theta,\varphi) = \partial_{\mathbf{n}}\left(r^k\,Y_k^m(\theta,\varphi)\right), \tag{6.9}$$

$$\tau^0_{km}(r,\theta,\varphi) = r^k\,Y_k^m(\theta,\varphi). \tag{6.10}$$

Plugging this back into Equations (6.6) and (6.8) yields:

$$a_{k'm'}[\sigma] = \int_S \tau^0_{k'm'}(\mathbf{r})\,\sigma(\mathbf{r})\,\mathrm{d}S, \tag{6.11}$$

$$a_{k'm'}[\tau] = \int_S \sigma^0_{k'm'}(\mathbf{r})\,\tau(\mathbf{r})\,\mathrm{d}S. \tag{6.12}$$

If we expand σ and τ as given in Equations (6.1) and (6.2), and zoom in on the σ_{km} and τ_{km} terms, we get:

$$a_{k'm'}[\sigma_{km}] = \int_S \tau^0_{k'm'}(\mathbf{r})\,\sigma_{km}(\mathbf{r})\,\mathrm{d}S, \tag{6.13}$$

$$a_{k'm'}[\tau_{km}] = \int_S \sigma^0_{k'm'}(\mathbf{r})\,\tau_{km}(\mathbf{r})\,\mathrm{d}S. \tag{6.14}$$

It now makes sense to define the inner products as introduced in [6]:

$$\langle\sigma_1|\sigma_2\rangle = \alpha\int_S \tau[\sigma_1](\mathbf{r})\sigma_2(\mathbf{r})\,\mathrm{d}S, \tag{6.15}$$

$$\langle\tau_1|\tau_2\rangle = \alpha\int_S \sigma[\tau_1](\mathbf{r})\tau_2(\mathbf{r})\,\mathrm{d}S, \tag{6.16}$$

where $\alpha \in \mathbb{R}_+$ can be chosen freely and we introduce the notation $\tau[\sigma]$. This notation represents the NDD τ that generates the same magnetic field as the given CD σ. The proof that the above definitions are inner products, is given in Appendix A.2.

As α can be chosen freely, one could just take $\alpha = 1$. A more intuitive α can be found though, that causes the first coefficient of the DSHE to be equal to the first coefficient of the multipolar basis derived in this chapter. To find this α we first need to derive the relation between the DSHE and multipolar basis on S. We also need to orthogonalise the basis. After this is done, the intuitive α is derived in Section 6.3.

With this inner product, a new norm is defined as well. For clarity, we give a definition of the three norms used in this thesis, and how each is denoted.

Definition 6.1. There are three norms used throughout this thesis.

(a) The norm of the CD σ, induced by the inner products in Equations (6.15) and (6.16) is defined and denoted by

$$||\sigma|| = (\langle\sigma|\sigma\rangle)^{1/2} = \left(\alpha \int_S \tau[\sigma](\mathbf{r})\,\sigma(\mathbf{r})\mathrm{d}S\right)^{1/2}. \tag{6.17}$$

Note that $||\sigma|| = ||\tau[\sigma]|| = ||\sigma\tau||$ both analytically and numerically.

(b) The euclidean norm of $\mathbf{x} \in \mathbb{R}^n$, is denoted by

$$||\mathbf{x}||_2 = \left(\sum_{i=1}^{n} |\mathbf{x}_i|^2\right)^{1/2}. \tag{6.18}$$

(c) The absolute value of a scalar $a \in \mathbb{R}$ is denoted by $|a|$.

6.1.1. Relation Between the DSHE and the Multipolar Basis on S

Choosing this inner product now indeed allows us to rewrite Equations (6.6) and (6.8) as inner products:

$$a_{km}[\sigma] = \frac{\langle\sigma^0_{km}|\,\sigma\rangle}{\alpha}, \tag{6.19}$$

$$a_{km}[\tau] = \frac{\langle\tau^0_{km}|\,\tau\rangle}{\alpha}. \tag{6.20}$$

As discussed in [6], by symmetry of the inner product we know

$$\begin{aligned}\langle\sigma_1|\sigma_2\rangle &= \langle\sigma_2|\sigma_1\rangle \\ &= \alpha \int_S \tau[\sigma_2](\mathbf{r})\sigma_1(\mathbf{r})\,\mathrm{d}S \\ &= \alpha \int_S \tau_2(\mathbf{r})\sigma[\tau_1](\mathbf{r})\,\mathrm{d}S = \langle\tau_1|\tau_2\rangle.\end{aligned} \tag{6.21}$$

Here we use that σ_1 and τ_1 cause the same magnetic field, and thus $\tau[\sigma_1] = \tau_1$ and $\sigma[\tau_1] = \sigma_1$. So therefore

$$a_{km}[\sigma] = a_{km}[\tau] = \frac{\langle\sigma^0_{km}|\,\sigma\rangle}{\alpha}, \tag{6.22}$$

and by again using the expansion of Equation (6.1) we get:

$$a_{k'm'}[\sigma] = a_{k'm'}[\tau] = \sum_{k=1}^{\infty}\sum_{m=-k}^{k} c_{km}\frac{\langle\sigma^0_{k'm'}|\,\sigma_{km}\rangle}{\alpha}. \tag{6.23}$$

Note, that this equation holds for all bases σ_{km}, including non-orthogonal ones.

Furthermore, we can take the mean of both inner products and denote it by the $\sigma\tau$ inner product. This inner product ensures numerical symmetry, but is analytically equal to the σ and τ inner products:

$$\langle\sigma\tau_1|\sigma\tau_2\rangle = \frac{\alpha}{2}\int_S \sigma_1(\mathbf{r})\tau_2(\mathbf{r}) + \sigma_2(\mathbf{r})\tau_1(\mathbf{r})\,\mathrm{d}S = \langle\sigma_1|\sigma_2\rangle. \tag{6.24}$$

By numerical symmetry, we mean that the inner products $\langle\sigma\tau_1|\sigma\tau_2\rangle$ and $\langle\sigma\tau_2|\sigma\tau_1\rangle$ yield the exact same result when computed numerically. Analytically, all three inner products are equal, but the numerical errors caused by any computation, or more specifically by making τ and σ piecewise constant and taking a Riemann integral, are not equal for the inner products. Therefore, numerically we have $\langle \sigma_1 | \sigma_2 \rangle \neq \langle \sigma_2 | \sigma_1 \rangle$. Taking a numerical symmetric inner product prevents these asymmetries, but might lead to other issues.

In Section 6.4.1 we delve into the effects of using the different inner products in the numerical application. As the inner products are analytically equivalent, we use them interchangeably for now.

By Equations (6.13) and (6.14), the condition stated in Equation (6.3) can now also be rewritten to:

$$\langle \sigma^0_{k'm'} | \sigma_{km} \rangle = 0 \quad \text{if} \quad k' < k. \tag{6.25}$$

Recall that this equation means that the basis function σ_{km} does not contribute to the DSHE coefficients $a_{k'm'}$ with $k' < k$. This is be proven in Section 6.2, but under the assumption that Equation (6.25) is true, we can truncate Equation (6.23) to get:

$$a_{k'm'}[\sigma] = a_{k'm'}[\tau] = \sum_{k=0}^{k'} \sum_{m=-k}^{k} c_{km} \frac{\langle \sigma^0_{k'm'} \,|\, \sigma_{km} \rangle}{\alpha}, \tag{6.26}$$

where the inner product can be replaced by any of the inner products defined in Equations (6.15), (6.16) and (6.24). Note that the truncation of this sum, makes the computation of a_{km} equivalent to a matrix vector multiplication, where the matrix is lower triangular.

6.2. Finding an Orthonormalised Basis

We now show how to find orthonormalised bases, starting with the initial bases described in Equations (6.9) and (6.10). We also show that the two bases still yield the exact same magnetic field. Lastly, we show that due to the orthonormalisation process, Equation (6.3) holds. This is all done following the structure of [6].

In this thesis (Modified) Gram-Schmidt is used to orthogonalise the initial bases. Another orthogonalisation method could also be used and might be more stable, but this is outside of our scope. We use the inner product as described in Equations (6.15) and (6.16). The km'-th iteration of Gram-Schmidt is as follows:

$$\tilde{\sigma}_{km} = \sigma^0_{km} - \sum_{k'=1}^{k-1} \sum_{m'=-k'}^{k'} \frac{\langle \sigma^0_{km} | \tilde{\sigma}_{k'm'} \rangle}{||\tilde{\sigma}_{k'm'}||^2} \tilde{\sigma}_{k'm'} - \sum_{m'=-k}^{m-1} \frac{\langle \sigma^0_{km} | \tilde{\sigma}_{km'} \rangle}{||\tilde{\sigma}_{km'}||^2} \tilde{\sigma}_{km'}, \tag{6.27}$$

$$\tilde{\tau}_{km} = \tau^0_{km} - \sum_{k'=1}^{k-1} \sum_{m'=-k'}^{k'} \frac{\langle \tau^0_{km} | \tilde{\tau}_{k'm'} \rangle}{||\tilde{\tau}_{k'm'}||^2} \tilde{\tau}_{k'm'} - \sum_{m'=-k}^{m-1} \frac{\langle \tau^0_{km} | \tilde{\tau}_{km'} \rangle}{||\tilde{\tau}_{km'}||^2} \tilde{\tau}_{km'}. \tag{6.28}$$

The above equations hold for both classical Gram-Schmidt (CGS) and modified Gram-Schmidt (MGS). As CGS is a bit more intuitive to follow, Figure 6.1 gives a schematic representation of the computation of $\tilde{\sigma}_{km}$ (or $\tilde{\tau}_{km}$) using CGS. It shows the $4, 2$'-th step of MGS, so we are determining $\tilde{\sigma}_{4,2}$. This is done by removing all the parts of $\sigma^0_{4,2}$ that are the projection onto the orthogonalised basis vectors $\tilde{\sigma}_{k'm'}$ before it. This summation of these parts is split up into two parts. The first contains the left three arrows in Figure 6.1, as they go from $-k'$, up to k', for $k' = 1, \ldots, k-1 = 1, 2, 3$. The second sum contains the right arrow in Figure 6.1, as it only goes up to $k' = k - 1 = 2 - 1 = 1$.

After the bases are orthogonalised, we can normalise them to find σ_{km} and τ_{km}:

$$\sigma_{km} = \frac{\tilde{\sigma}_{km}}{||\tilde{\sigma}_{km}||}, \tag{6.29}$$

$$\tau_{km} = \frac{\tilde{\tau}_{km}}{||\tilde{\tau}_{km}||}. \tag{6.30}$$

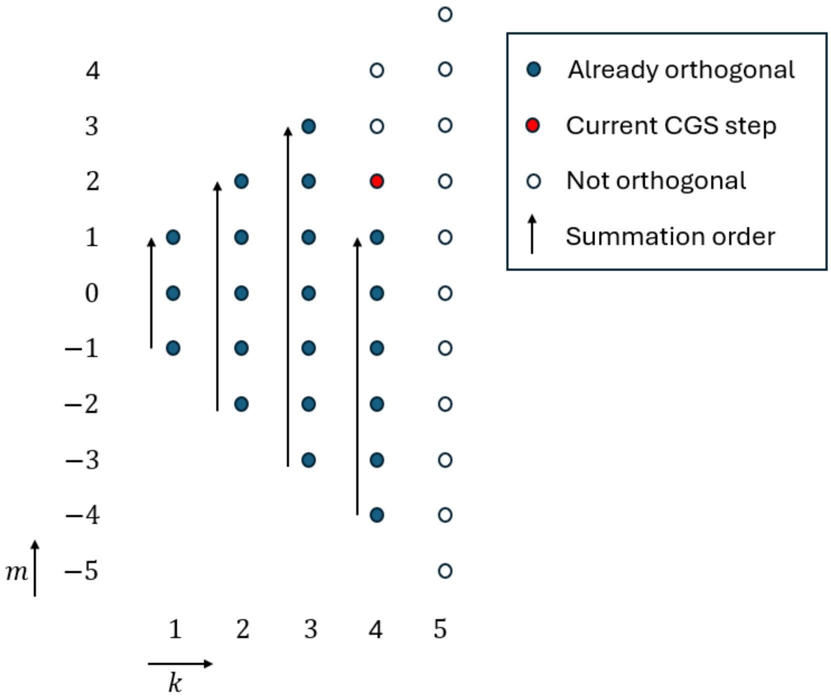

Figure 6.1: A schematic overview of the summation within the $4,2$-'th step of CGS. The basis vector that is currently orthogonalised, $\sigma^0_{4,2}$, is represented by the red dot. The blue dots represent the orthogonalised basis vectors $\tilde{\sigma}_{k'm'}$ from the CGS steps before this one. The white dots represent the non-orthogonal basis vectors $\sigma^0_{k'm'}$ that will be orthogonalised in later CGS steps.

The orthogonalisation process above, results in the following properties and have been proven in [6].

Theorem 6.2. *Suppose σ^0_{km} and τ^0_{km} produce the same magnetic field for all $k = 1, 2, \ldots, k_{\max}$ and $m = -k, -k+1, \ldots, k$. Then*

(a) $\tilde{\sigma}_{km}$ and $\tilde{\tau}_{km}$ from Equations (6.27) and (6.28) produce the same magnetic field for all $k = 1, 2, \ldots, k_{\max}$ and $m = -k, -k+1, \ldots, k$.

(b) the normalised σ_{km} and τ_{km} from Equations (7.6) and (6.30) produce the same magnetic field for all $k = 1, 2, \ldots, k_{\max}$ and $m = -k, -k+1, \ldots, k$.

(c) the coefficients c_{km} from Equations (6.1) and (6.2) are equal in both bases.

(d) $\langle \sigma^0_{k'm'} | \sigma_{km} \rangle = 0 \quad$ if $\; k' < k$, by Equation (6.25).

Proof. The proof of Theorem 6.2 is split into the same parts as the theorem is:

(a) We proof by induction. We know that σ^0_{km} and τ^0_{km} produce the same field. For the induction hypothesis, we assume $\tilde{\sigma}_{k'm'}$ and $\tilde{\tau}_{k'm'}$ produce the same field if $k' < k$, or if $m' < m$ when $k' = k$. In that case, we know that $\langle \sigma^0_{km} | \tilde{\sigma}_{k'm'} \rangle = \langle \tau^0_{km} | \tilde{\tau}_{k'm'} \rangle$, and $||\tilde{\sigma}_{k'm'}||^2 = ||\tilde{\tau}_{k'm'}||^2$. Therefore, $\tilde{\sigma}_{km}$ and $\tilde{\tau}_{km}$ are the sum of distributions that produce the same magnetic field, and thus they produce the same field themselves.

(b) As $\tilde{\sigma}_{km}$ and $\tilde{\tau}_{km}$ produce the same field, we know $||\tilde{\sigma}_{km}|| = ||\tilde{\tau}_{km}||$. So therefore indeed, σ_{km} and τ_{km} also produce the same magnetic field.

(c) σ and τ from Equations (6.1) and (6.2) produce the same magnetic field by design. As the σ_{km} and τ_{km} are orthogonal, by Equations (6.1) and (6.2) we know $c_{km} = \langle \sigma | \sigma_{km} \rangle$. By symmetry of the inner product, we get $c_{km} = \langle \sigma_{km} | \sigma \rangle$. Lastly, by symmetry and the definition of the inner product, we get $c_{km} = \langle \sigma | \sigma_{km} \rangle = \langle \tau_{km} | \tau \rangle$.

(d) We replace σ_{km} by $\tilde{\sigma}_{km}$, as this is just a scaled version of σ_{km}. Let $\tilde{k} < k$, and rewrite equation (6.27) to:

$$\sigma^0_{\tilde{k}\tilde{m}} = \tilde{\sigma}_{\tilde{k}\tilde{m}} + \sum_{k'=1}^{\tilde{k}-1} \sum_{m'=-k'}^{k'} \frac{\langle \sigma^0_{\tilde{k}\tilde{m}} | \tilde{\sigma}_{k'm'} \rangle}{||\tilde{\sigma}_{k'm'}||^2} \tilde{\sigma}_{k'm'} + \sum_{m'=-\tilde{k}}^{\tilde{m}-1} \frac{\langle \sigma^0_{\tilde{k}\tilde{m}} | \tilde{\sigma}_{\tilde{k}m'} \rangle}{||\tilde{\sigma}_{\tilde{k}m'}||^2} \tilde{\sigma}_{\tilde{k}m'}. \tag{6.31}$$

Then plug the above into the LHS of Equation (6.25):

$$\langle \sigma^0_{\tilde{k}\tilde{m}} | \tilde{\sigma}_{km} \rangle = \langle \tilde{\sigma}_{\tilde{k}\tilde{m}} | \tilde{\sigma}_{km} \rangle + \sum_{k'=1}^{\tilde{k}-1} \sum_{m'=-k'}^{k'} \frac{\langle \sigma^0_{\tilde{k}\tilde{m}} | \tilde{\sigma}_{k'm'} \rangle}{||\tilde{\sigma}_{k'm'}||^2} \langle \tilde{\sigma}_{k'm'} | \tilde{\sigma}_{km} \rangle + \sum_{m'=-\tilde{k}}^{\tilde{m}-1} \frac{\langle \sigma^0_{\tilde{k}\tilde{m}} | \tilde{\sigma}_{\tilde{k}m'} \rangle}{||\tilde{\sigma}_{\tilde{k}m'}||^2} \langle \tilde{\sigma}_{\tilde{k}m'} | \tilde{\sigma}_{km} \rangle. \tag{6.32}$$

We know that all $\tilde{\sigma}_{km}$ are orthogonal. So since $\tilde{k} < k$, we know $\langle \tilde{\sigma}_{\tilde{k}\tilde{m}} | \tilde{\sigma}_{km} \rangle = 0$. In the second term, we know $k' < \tilde{k} < k$ so $\langle \tilde{\sigma}_{k'm'} | \tilde{\sigma}_{km} \rangle = 0$, and for the third term, we know $\tilde{k} < k$, so therefore $\langle \tilde{\sigma}_{\tilde{k}m'} | \tilde{\sigma}_{km} \rangle = 0$. After scaling back to σ_{km} and replacing $\tilde{k}\tilde{m}$ by $k'm'$, we indeed get:

$$\langle \sigma^0_{k'm'} | \sigma_{km} \rangle = 0 \quad \text{if} \quad k' < k. \tag{6.33}$$

□

Modified Gram-Schmidt

For the numerical implementation of Gram-Schmidt, we use a modified version, as the classical version has quite large numerical instabilities [12, pp. 254-256]. Modified Gram-Schmidt (MGS) is analytically identical to Classical Gram-Schmidt (CGS), but the computation is done in such a way that numerical errors do not compound as much as in CGS. Instead of orthogonalising the current vector with respect to all previous vectors, we orthogonalise all remaining vectors with respect to the current vector. As described in Section 6.4.1, the orthonormalisation works best with the $\langle \tau_1 | \tau_2 \rangle$ inner product. Therefore we use this inner product in the following pseudo code:

Algorithm 1 Algorithm to find an orthonormal basis, using Modified Gram-Schmidt. For ease in notation, we replace km by one index i.

```
Data: $\sigma_i = \sigma_i^0$ and $\tau_i = \tau_i^0$ for $i = 1, \dots, k_{\text{max}}(k_{\text{max}} + 2)$
Result: $\sigma_i$ and $\tau_i$ for $i = 1, \dots, k_{\text{max}}(k_{\text{max}} + 2)$

for $i = 1, \dots, k_{\text{max}}(k_{\text{max}} + 2)$ do
    $\sigma_i \leftarrow \sigma_i / ||\tau_i||$
    $\tau_i \leftarrow \tau_i / ||\tau_i||$
    for $j = i + 1, \dots, k_{\text{max}}(k_{\text{max}} + 2)$ do
        $\sigma_j \leftarrow \sigma_j - \langle \tau_i | \tau_j \rangle \, \sigma_i$
        $\tau_j \leftarrow \tau_j - \langle \tau_i | \tau_j \rangle \, \tau_i$
    end for
end for
```

6.3. Choosing α

As stated before, α can be chosen freely, however following the argument of [6], we want to choose it such that the coefficients of the 'first' functions in the bases are equal, i.e., $a_{k,m} = c_{k.m}$ for $k = 1$ and $m = -1$. We start by taking the square norm of $\sigma\tau^0_{1,-1}$:

$$\begin{aligned}||\sigma\tau^0_{1,-1}||^2 &= \alpha\int_S \sigma^0_{1,-1}\tau^0_{1,-1}\mathrm{d}S\\ &= \alpha\int_S \partial_{\mathbf{n}}(rY_1^{-1})(rY_1^{-1})\mathrm{d}S\\ &= \alpha\int_S \left[\nabla(rY_1^{-1})\cdot\mathbf{n}\right](rY_1^{-1})\,\mathrm{d}S. \end{aligned} \tag{6.34}$$

If we now apply Green's first identity, we get

$$\begin{aligned}||\sigma\tau^0_{1,-1}||^2 &= \alpha\int_{V_S} \nabla(rY_1^{-1})\cdot\nabla(rY_1^{-1}) + (rY_1^{-1})\nabla^2(rY_1^{-1})\,\mathrm{d}V_S\\ &= \alpha\int_{V_S} \nabla(rY_1^{-1})\cdot\nabla(rY_1^{-1})\,\mathrm{d}V_S, \end{aligned} \tag{6.35}$$

where V_S is the volume surrounded by the surface S. Furthermore, the second term in the equation drops out, as rY_1^{-1} is a first order solid Harmonic, and thus solves the Laplace equation: $\nabla^2(rY_1^{-1}) = 0$.

To find α, we now use that $\nabla(rY_1^{-1})\cdot\nabla(rY_1^{-1}) = 1$. The proof of this is given in Appendix A.3. Using this property, we get:

$$||\sigma\tau^0_{1,-1}||^2 = \alpha V_S. \tag{6.36}$$

Now, we use the above, and the fact that $\sigma\tau_{1,-1} = \frac{\sigma\tau^0_{1,-1}}{||\sigma\tau^0_{1,-1}||}$, to rewrite Equation (6.26) for $k, m = 1, -1$:

$$\begin{aligned} a_{1,-1} &= c_{1,-1}\frac{\langle\sigma\tau^0_{1,-1}|\sigma\tau_{1,-1}\rangle}{\alpha} = c_{1,-1}\frac{\langle\sigma\tau^0_{1,-1}|\sigma\tau^0_{1,-1}\rangle}{\alpha||\sigma\tau^0_{1,-1}||}\\ &= c_{1,-1}\frac{||\sigma\tau^0_{1,-1}||}{\alpha} = c_{1,-1}\sqrt{\frac{V_S}{\alpha}}. \end{aligned} \tag{6.37}$$

Now to have $a_{1,-1} = c_{1,-1}$ we choose $\alpha = V_S$.

6.4. Basis Vectors and Orthonormalisation

Before finding the coefficients of the expansions in Chapter 7, we zoom in on the basis functions themselves. We look at the initial basis, the found orthonormal basis, and whether this basis is actually orthogonal. Furthermore we discuss some details of the numerical implementation.

We start with the initial basis and the orthonormal basis, for some combinations of k and m. We also plot the spherical harmonic function of the same degree and order. The result is given in Figure 6.2.

In Figure 6.2 we see that indeed $\sigma^0_{1,-1} = \sigma_{1,-1}$. Furthermore, we see that all orthonormal basis functions, look very similar to the spherical harmonic function of the same degree and order.

6.4.1. Numerics of Orthonormalisation

In the orthonormalisation process described in Algorithm 1, the inner product between σ_i and σ_j is taken. Recall from Equations (6.21) and (6.24), that there are three analytically equivalent ways to compute this inner product.

The numerical instabilities of CGS, still occur when using MGS if the initial basis is very non-orthogonal [12, pp. 254-256]. In our numerical implementation, these numerical instabilities occur faster when using the combined inner product $\langle\sigma\tau_i|\sigma\tau_j\rangle$, (and the σ inner product: $\langle\sigma_i|\sigma_j\rangle$,) than when we use $\langle\tau_i|\tau_j\rangle$. In this section we explain which numerical results lead us to this conclusion. We have not found a clear reason for why these numerical results occur.

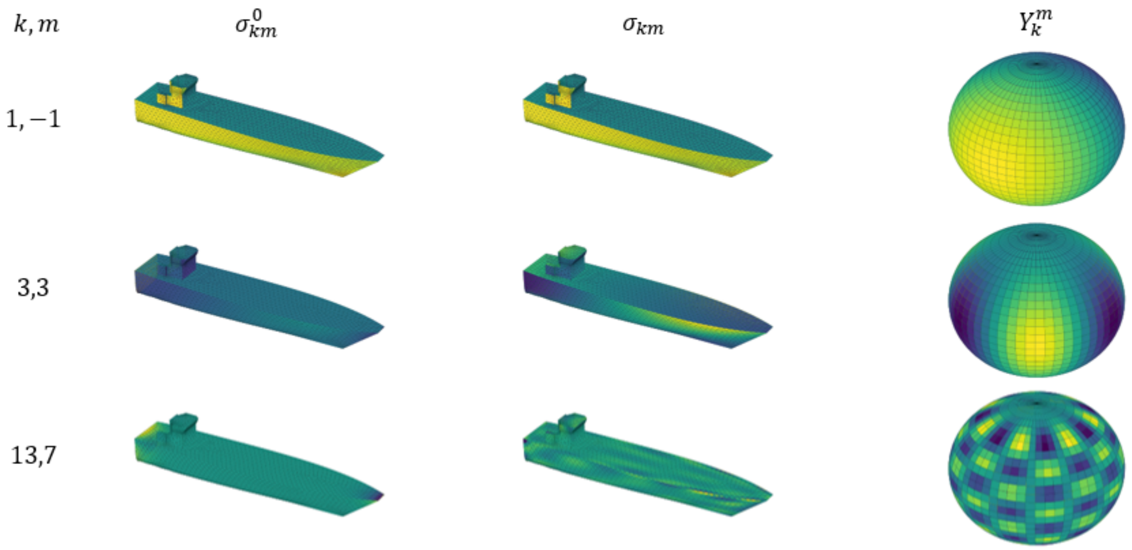

Figure 6.2: From left to right: The initial basis of the charge distribution σ^0_{km} on the surface of Albatros, the orthonormalised basis σ_{km}, and their corresponding spherical harmonic function Y^m_k on a sphere. From top to bottom, the basis functions are of degree and order $(k, m) = (1, -1), (3, 3), (13, 7)$. The magnitude of the plots is not given, as a basis can always be normalised.

Analytical vs. numerical equivalence

We first show that the analytically equivalent inner products do not yield the same result when computed numerically with piecewise constant functions. Figure 6.3 shows the three inner products applied to the normalised initial basis. We also plot the normed absolute difference. If we want to compare $\langle \tau^0_{150} | \tau^0_j \rangle$ and $\langle \sigma^0_{150} | \sigma^0_j \rangle$, this difference is defined by

$$\text{Normed absolute difference} = \frac{|\langle \tau^0_{150} | \tau^0_j \rangle - \langle \sigma^0_{150} | \sigma^0_j \rangle|}{|\langle \tau^0_{150} | \tau^0_j \rangle|}. \tag{6.38}$$

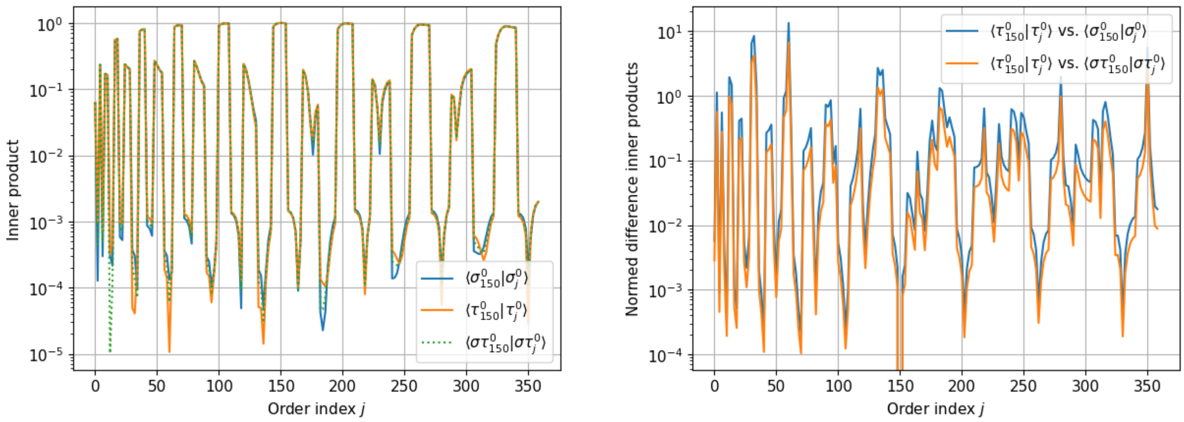

(a) Absolute value of the inner products.

(b) Normed absolute difference between the inner products.

Figure 6.3: A comparison of the analytically equivalent inner products. The inner product is taken between the normalised versions of the 150'th (so $k = 12$, and $m = -5$) and j'-th vectors of the initial bases σ^0_{km} and τ^0_{km}. In the figure we joined the km subscript together, to just a single index i or j.

In Figure 6.3 we see that although similar, there are significant differences between the inner products. Therefore, choosing a particular inner product within the computations, can have effect on the found basis, and on the computations performed using that basis. This raises the question whether all basis functions are actually orthogonal. Especially when the inner products $\langle \sigma_i | \sigma_j \rangle$ and $\langle \tau_i | \tau_j \rangle$ are used.

Effects on orthogonality of different inner products during MGS

To answer this question, we find the orthonormal bases according to Algorithm 1 using different inner products. One basis is found using the $\langle \tau_i | \tau_j \rangle$ inner product, and the other using the $\langle \sigma\tau_i | \sigma\tau_j \rangle$ inner product. Next, we compute the inner products for some basis vector τ_i, with all τ_j's. Figure 6.4 shows the inner products between a fixed basis function τ_i with all τ_j's, where the functions were orthonormalised with the $\langle \tau_i | \tau_j \rangle$ inner product:

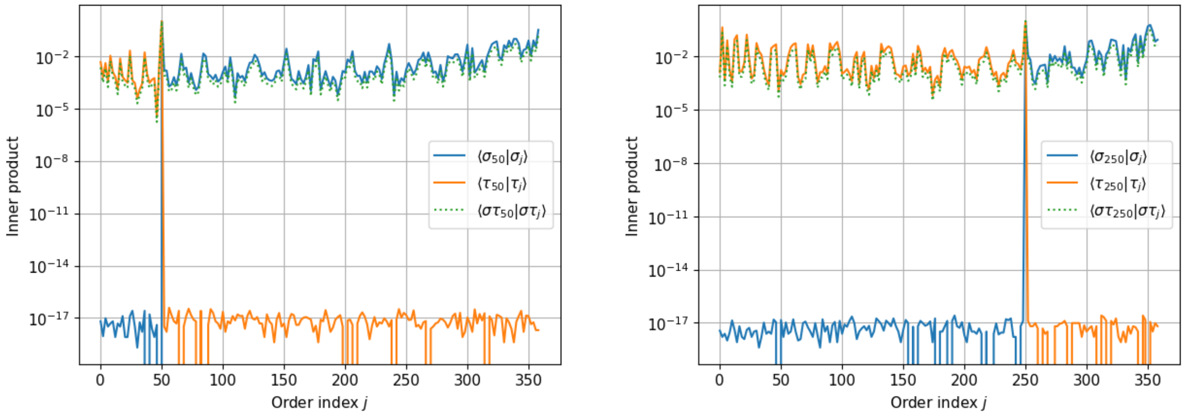

(a) $i = 50$

(b) $i = 250$

Figure 6.4: The inner products taken between a fixed τ_i and all τ_j. The functions were orthogonalised using the inner product: $\langle \tau_i | \tau_j \rangle$. In the figure we joined the km subscript together, to just a single index i or j.

Immediately, the big jump in the inner product is visible around $i = 50$ and $i = 250$. This jump makes sense, as when we apply MGS, we orthogonalise the vectors σ_i and τ_i with all σ_j and τ_j with $j > i$. This orthogonalisation happens using the $\langle \tau_i | \tau_j \rangle$ inner product, so for $j > i$, this inner product is put to zero during MGS. For $j < i$, the orthogonality is not as good.

Similarly, we have that numerically $\langle \sigma_i | \sigma_j \rangle$ is equal to $\langle \tau_j | \tau_i \rangle$ (analytically this is always the case). Therefore, for $j < i$, τ_j has been orthogonalised with τ_i according to the $\langle \tau_i | \tau_j \rangle$ inner product. So therefore the $\langle \sigma_i | \sigma_j \rangle$ inner product is put to zero when $j < i$, as depicted in the figure. Again, for the other section, $j > i$, the orthogonality is not good.

These results are not surprising, and consistent with the used inner product within MGS. This would make an argument, to use the combined inner product, $\langle \sigma\tau_i | \sigma\tau_j \rangle$, within MGS. Then, all basis functions are orthogonal to each other, while using the combined inner product. This is indeed clear from Figure 6.5.

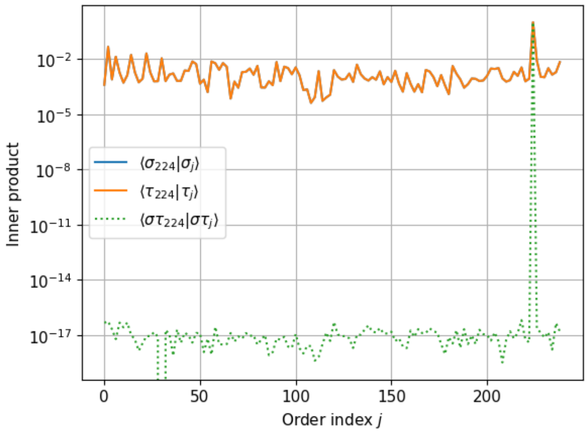

Figure 6.5: The inner products taken between a fixed σ_{224} and all σ_j. The functions were orthogonalised using the combined inner product: $\langle \sigma\tau_i | \sigma\tau_j \rangle$. In the figure we joined the km subscript together, to just a single index i or j.

Choosing an inner product

A first thought might be to then use the combined inner product. However, due to the numerical instabilities in our code, at some point negative squared norms occur in Algorithm 1 (during the computation of the norms in lines 5 and 6). Figure 6.6 shows these squared norms.

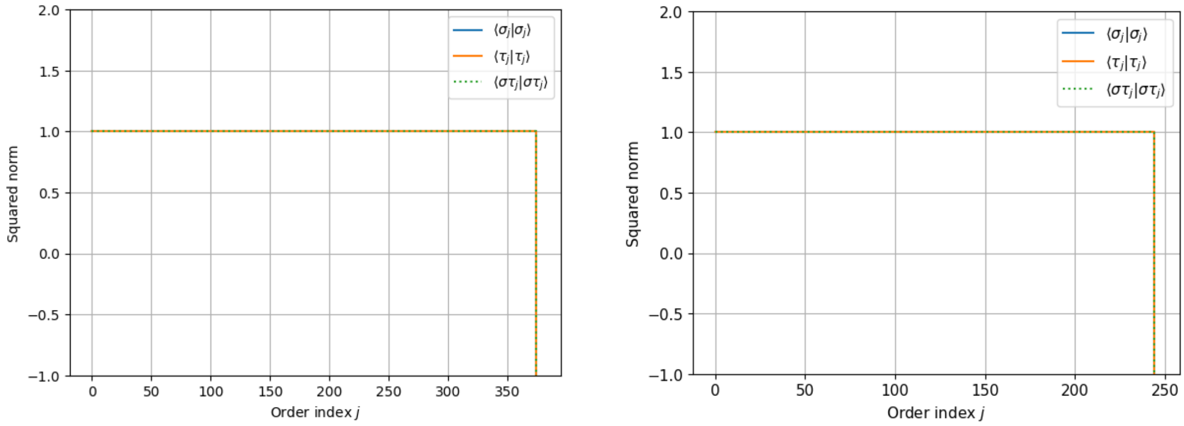

Figure 6.6: The squared norm of σ_j, taken with three different inner products. The functions in the left figure were orthogonalised using the inner product: $\langle\tau_i|\tau_j\rangle$, and in the right with the inner product: $\langle\sigma\tau_i|\sigma\tau_j\rangle$. The figures have been cut off at -1 on the y-axis to clarify the value of the squared norm before it blows up. In the figure we joined the km subscript together, to just a single index i or j.

For the basis orthogonalised with the $\langle\tau_i|\tau_j\rangle$ inner product, the squared norm becomes negative for $j = 376$. For the combined inner product, this occurs at $j = 245$. After such a norm occurs, the algorithm cannot continue, and the orthonormal basis cannot be extended. Therefore we choose to use the $\langle\tau_i|\tau_j\rangle$ inner product for orthonormalisation.

Other orthogonalisation issues

For all smaller orders than the one where the squared norm became negative, a basis has been computed. However, the quality of the basis has not been investigated yet. As described in [6], we expect that the basis functions look similar to the spherical harmonic functions after orthogonalisation. In this section we give an example where this is not the case, even though the squared norm of the function remains equal to 1. The example we choose uses the combined inner product during orthogonalisation. This is done as it is the clearest example we found. The example illustrates that similar issues can occur when using the $\langle\tau_i|\tau_j\rangle$ inner product.

Recall from Figure 6.6, that the squared norm of the basis functions derived with the combined inner product, became negative for $j = 245$. If we take $k_{\max} = 14$, the maximum order is $14(14 + 2) = 224 < 245 + 1$. (The $+1$ is to take into account the zero-based indexing of python.) So all basis functions are numerically orthonormal w.r.t. the combined inner product. We now plot the basis function for $k = 14, m = 14$, using the basis of the combined inner product, the $\langle\tau_i|\tau_j\rangle$ inner product, and of the spherical harmonics.

In the Figure 6.7 we see that the basis vector $\tau_{14,14}$ that is found using the combined inner product, does not look similar to Y_{14}^{14}, while the basis vector found with $\langle\tau_i|\tau_j\rangle$ does look similar. Therefore it is reasonable to believe that the basis function found with the combined inner product is incorrect, and might not follow the properties of Theorem 6.2.

We conclude that even when the norm of the basis function is equal to 1, the quality of the basis function is not guaranteed. Therefore, one should pay attention whether expanding a basis with a new basis function actually improves the basis or not.

Solving orthogonalisation issues

The question of the need of an orthogonal basis was already raised in the introduction of this chapter. In Sections 7.4 and 8.5 we investigate this option and see that this allows us to use higher order basis functions, and yields good results when Bayesian inference is applied.

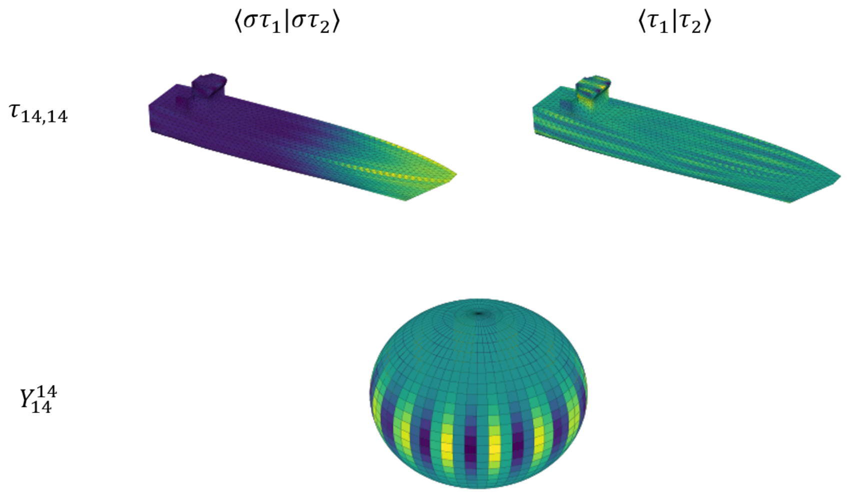

Figure 6.7: Basis vectors of different bases for $k = 14$, $m = 14$. The top left figure is the basis vector from NDD basis functions τ_{km} orthogonalised with the combined inner product $\langle \sigma\tau_i | \sigma\tau_j \rangle$. The top right is from the bases orthogonalised using the $\langle \tau_i | \tau_j \rangle$ inner product. The bottom figure simply shows the Spherical Harmonic function Y_{14}^{14} on a sphere.

In future work, if one does prefer to use an orthogonal basis, one could perform more research the loss of orthogonality and quality of the basis. Ideas are, using another orthogonalisation method, using a smaller mesh.

Now that an orthogonal basis has been found, and some properties have been investigated, we need to find the coefficients of the basis vectors. In Chapter 7 a few methods are introduced, to find the c_{km} based on a measurement vector. This measurement vector is based on the Benchmark case introduced in Chapter 3.

7

Determining Coefficients of the New Basis and Mapping to the DSHE

In Chapter 6 we derived an orthogonal basis to describe the CD σ and the NDD τ on an arbitrary surface. In this chapter we discuss how to determine the corresponding coefficients c_{km}, and whether the found alternative sources, indeed model the magnetic field well.

As described in the introduction of Chapter 6, one of the goals of the new basis is to be able to easily map between it, and the DSHE. Therefore, we also go into how to find the DSHE coefficients a_{km}, once the c_{km} are known.

Recall from Section 5.5.1 that the bases for σ and τ are piecewise constant. This makes many of the computations in the previous chapter easier. As the relation between a_{km} and σ in Equation (6.22) is analytical and holds for any σ, we investigate the effects of computing this integral more precisely in Section 7.1. It turns out that this leads to a better approximation of the magnetic field outside of the BS.

Furthermore, in [6, Sec. 4.6] it is suggested that the DSHE coefficients should only be computed up to the order that we have computed the c_{km} coefficients, say $k_{\max,\sigma}$. However, the contribution of a basis vector σ_{km} to the coefficient $a_{k'm'}$ with $k' > k_{\max,\sigma} \geq k$ is not zero. So the truncation of the DSH expansion at the order $k_{\max,\sigma}$, leads to an approximation of the truncated σ expansion. Therefore, for the order $k_{\max,\sigma}$ approximation of σ, we compute the DSHE up to the order $k_{\max,\mathrm{DSHE}} = k_{\max,\sigma} + 40$. (Here, the number 40 follows from trial and error, and is not an analytical result.) A more detailed explanation, and numerical results to back the argument, are given in Section 7.2.

In Chapter 8 noise and regularisation of the method is introduced. To avoid confusing the errors caused by the mapping to the DSHE, with the errors caused by the noise, we do not map our approximation of σ to the DSHE to compute $\mathbf{H}_{\mathrm{ind}}$ on the error planes. Note however, that this mapping to the DSHE is a key part of the method investigated in this thesis.

7.1. Determining c_{km} Using Measurements of $\mathbf{H}$

Recall from Section 5.5 that we could compute a piecewise constant approximation of σ by using measurements of ϕ and measurements of $\mathbf{H}$. The same holds when we determine the c_{km} coefficients of the multipolar basis. In this chapter we focus on using $\mathbf{H}$, as this is the measurement available in reality. This section goes into the method, of how to build a matrix vector equation that with inversion, gives the coefficients c_{km} based on measurements of the magnetic field.

In Section 5.5 the matrix was built up from the contribution per basis vector, to the magnetic field at a certain measurement location. This is done now as well, but the basis vectors χ_{e_j} are replaced by the σ_{km}'s from Chapter 6. As the σ_{km}'s have two indices, we flatten the indices by indexing them with $j = 1, 2, \ldots, k_{\max}(k_{\max}+2)$. Now the matrix entry a_{ij} is the contribution of the basis vector $\sigma_{k(j)m(j)}$ to the measurement at location $\mathbf{r}_i$ in direction $\mathbf{e}_i$. We get:

$$\begin{aligned} a_{ij} &= \int_{\tilde{\mathbf{r}}\in S} \frac{1}{4\pi} \frac{(\mathbf{r}_i - \tilde{\mathbf{r}})\cdot \mathbf{e}_i}{||\mathbf{r}_i - \tilde{\mathbf{r}}||_2^3} \sigma_{k(j)m(j)}(\tilde{\mathbf{r}})\,\mathrm{d}S \\ &= \sum_{l=1}^{N_e} \int_{\tilde{\mathbf{r}}\in e_l} \frac{1}{4\pi} \frac{(\mathbf{r}_i - \tilde{\mathbf{r}})\cdot \mathbf{e}_i}{||\mathbf{r}_i - \tilde{\mathbf{r}}||_2^3} \sigma_{k(j)m(j)}(\tilde{\mathbf{r}})\,\mathrm{d}S \\ &= \sum_{l=1}^{N_e} \sigma_{k(j)m(j)}(\mathbf{r}_{e_l}) \int_{\tilde{\mathbf{r}}\in e_l} \frac{1}{4\pi} \frac{(\mathbf{r}_i - \tilde{\mathbf{r}})\cdot \mathbf{e}_i}{||\mathbf{r}_i - \tilde{\mathbf{r}}||_2^3}\,\mathrm{d}S. \end{aligned} \tag{7.1}$$

Here we used that σ_{km} is piecewise constant on each element e_l, and $\mathbf{r}_{e_l}$ is the centre of the element e_l. We approximate this equation by

$$a_{ij} = \sum_{l=1}^{N_e} \frac{1}{4\pi} \frac{(\mathbf{r}_i - \mathbf{r}_{e_l})\cdot \mathbf{e}_i}{||\mathbf{r}_i - \mathbf{r}_{e_l}||_2^3}\, \sigma_{k(j)m(j)}(\mathbf{r}_{e_l})\, w_l. \tag{7.2}$$

Note that this approximation can cause large errors when the measurement location is close to the surface S. Solving this issue is outside of the scope of this Thesis. In future work, the integral might be computed more precisely with a numerical approach, or an analytical based on [8, pp. 243-246].

Our vector $\mathbf{x}$ contains the flattened version of the coefficients: $c_{k(j)m(j)}$ for $j = 1, 2, \ldots, k_{\max}(k_{\max}+2)$. The measurement vector $\mathbf{b}$ contains the measurements $\mathbf{H}(\mathbf{r}_i)\cdot\mathbf{e}_i$.

Solving $A\mathbf{x} = \mathbf{b}$ now yields the coefficients c_{km} as needed.

7.1.1. Results

We want to compare the new method where we find the c_{km} coefficients, to the method from Chapter 5 where we directly solve for a piecewise constant σ. We start by plotting $\sigma = \sum_{k,m} c_{km}\sigma_{km}$ on S in Figure 7.1. We also repeat Figure 5.4.

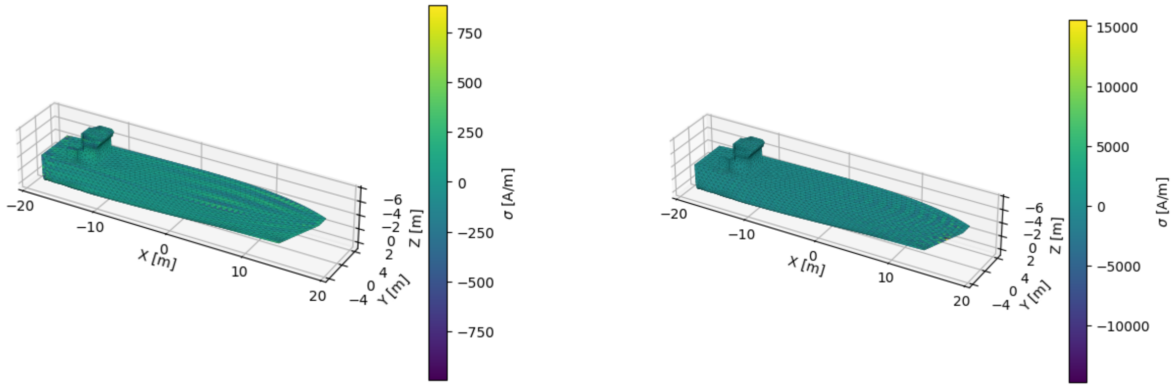

(a) $\sigma = \sum_{k,m} c_{km}\sigma_{km}$ **(b)** Repetition of Figure 5.4a

Figure 7.1: The equivalent charge distribution $\sigma = \sum_{k,m} c_{km}\sigma_{km}$ with $k_{\max} = 18$ on the surface S, the outside of the Albatros ferry, and a repetition of Figure 5.4a. The CD σ of the left figure was found using the method described in Section 7.1. The $N_{\text{meas}} = 1410$ measurements were taken on the box shaped surface of Figure 3.1. The used magnetic background field was $\mathbf{B}_0 = (23.360, 0, 41.234)$ μT.

If we compare Figure 7.1a to Figure 7.1b, we see that the extreme values within the plot have become slightly lower, and the solution seems smoother in general as well. To qualitatively say whether this is therefore a 'better' solution, is not possible from this figure alone. Furthermore, we see a close resemblance to a spherical harmonic basis function on the top of the ship (the wavy pattern). Whether such a CD would occur in a natural setting, or is due to numerical errors causing an unreasonably large c_{km} is also difficult to say. We do note that this might still not be a 'good' σ, even if it does predict the magnetic field well.

To check whether it predicts the magnetic field $\mathbf{H}_{\text{ind}}$ well, we plot the magnetic field on the error plane partially within the BS, and compare it with the results from in Section 5.6.1. The result is given in Figure 7.2.

Comparing the columns from Figure 7.2, shows that the new method yields a good approximation of the magnetic field $\mathbf{H}_{\text{ind}}$ on the error plane.

To compare the two methods thoroughly, and see whether convergence occurs for increasing $k_{\max}$, we vary this $k_{\max}$ and compute the NRMSE according to Equation (5.51). This NRMSE is computed and compared for varying N_{meas} to the NRMSE computed with the σ from Section 5.6.1. The result is given in Figure 7.3.

In Figure 7.3 we see a clear convergence of the solution, for increasing $k_{\max}$, when $N_{\text{meas}} = 1410$ measurements are used. The convergence is not monotone though. A reason for this, could be the quality loss of the higher order basis vectors, as discussed in Section 6.4.1. Proving this reasoning, is outside of the scope of this thesis though.

For high $k_{\max}$, the NRMSE of the solution gets quite close to that of the CD found with the direct computation discussed in Section 5.5.3. This means that we have found a method that has computationally lower costs, is probably less sensitive to overfitting, and yields similar quality solutions as the method discussed in Section 5.5.3.

For $N_{\text{meas}} = 150$, the convergence is not as clear. Note that for $k_{\max} \geq 12$, we need to determine more than $k_{\max}(k_{\max} + 2) = 168$ c_{km} coefficients. It is logical therefore, that the coefficients found in such case are not of good quality, and lead to a large NRMSE. We even see that for $k_{\max} \leq 10$, the NRMSE of the different N_{meas}'s are somewhat close to each other.

7.2. Mapping to DSHE

Now that we have found a good approximation of σ, we want to check the quality of the mapping to the DSHE coefficients. We repeat the mapping from any σ to the DSHE coefficients (see Equation (6.6)):

$$a_{k'm'}[\sigma] = \int_S \tau^0_{k'm'}(\mathbf{r})\, \sigma(\mathbf{r})\, \mathrm{d}S.$$

Recall that our σ_{km}, and σ in general, were piecewise constant on each element of the ships hull. By plugging in Equation (5.42), we get:

$$\begin{aligned} a_{k'm'}[\sigma] &= \int_S \left[\tau^0_{k'm'}(\mathbf{r}) \sum_{j=1}^{N_e} \sigma_{e_j} \chi_{e_j}(\mathbf{r}) \right] \mathrm{d}S \\ &= \sum_{j=1}^{N_e} \sigma_{e_j} \int_{e_j} \tau^0_{k'm'}(\mathbf{r})\, \mathrm{d}S. \end{aligned} \tag{7.3}$$

Equation (7.3) holds for all piecewise constant σ, so also for all σ_{km} derived in Chapter 6. So if we compute the integral $\int_{e_j} \tau^0_{k'm'}(\mathbf{r})\mathrm{d}S$ for each element, up to some order $k_{\max,0}$, we can then map from the multipolar basis on S, to the DSHE by a simple matrix vector multiplication. For ease of notation, we swap the j for an n in the following equation. The elements of the matrix are defined by

$$a_{ij} = \sum_{n=1}^{N_e} \sigma_{k(j)m(j)}(\mathbf{r}_{e_n}) \int_{e_n} \tau^0_{k'(i)m'(i)}(\mathbf{r})\mathrm{d}S, \tag{7.4}$$

the vector $\mathbf{x}$ contains the c_{km} coefficients of the multipolar basis on S, and the vector $\mathbf{b}$ contains the $a_{k'm'}$ coefficients of the DSHE.

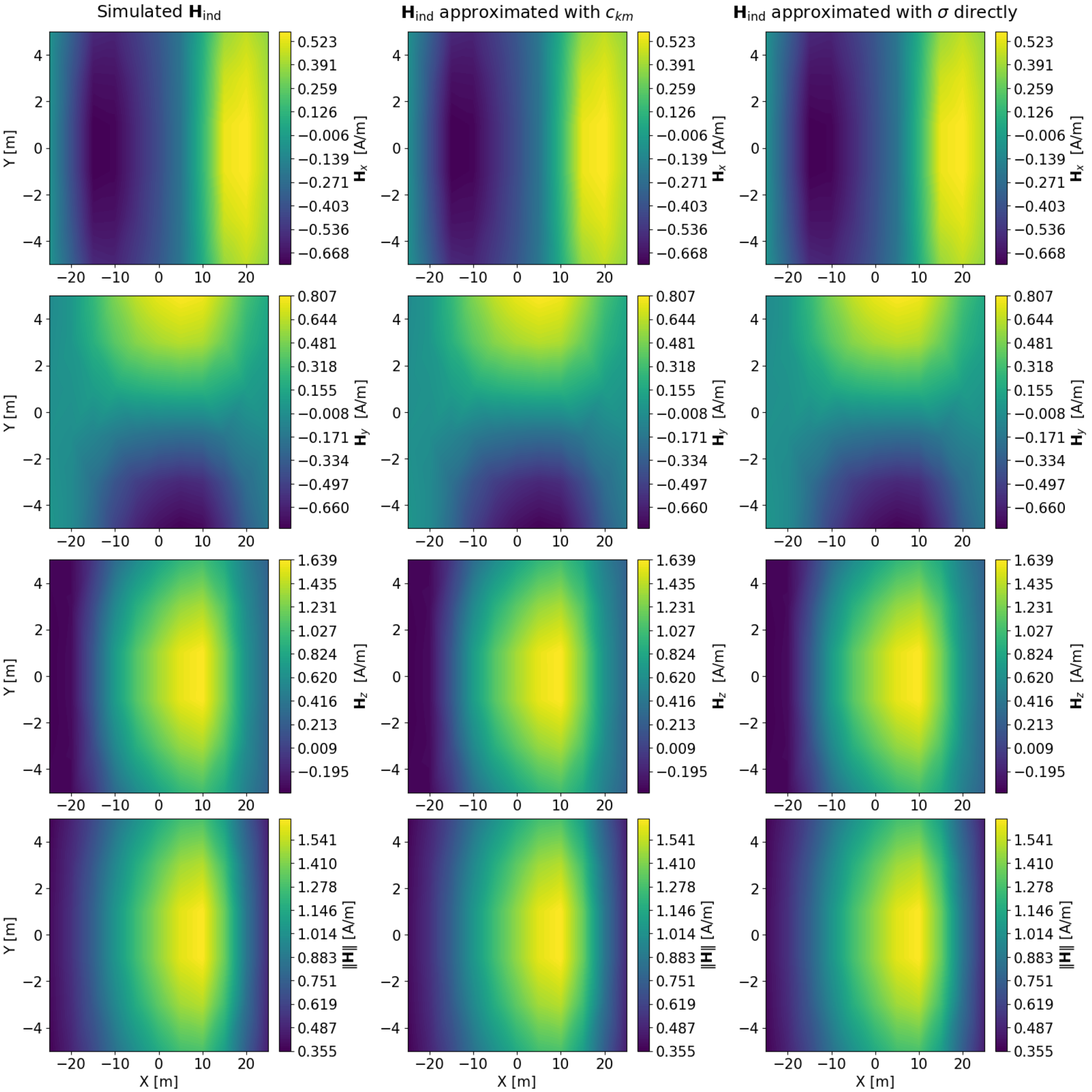

Figure 7.2: Induced magnetic field $\mathbf{H}_{\text{ind}}$ computed with two different σ's, compared to the simulated data computed with the MoM. The CD σ of the second column was computed via the orthogonal basis vectors σ_{km} with $k_{\max} = 18$. The CD of the third was computed by computing the piecewise constant σ using the method in Section 5.6.1. The $N_{\text{meas}} = 1410$ measurements were taken on hte box shaped surface of Figure 3.1. The rows show the different components of $\mathbf{H}_{\text{ind}}$, and its norm. The used magnetic background field was $\mathbf{B}_0 = (23.360, 0, 41.234)\,\mu\text{T}$. The magnetic field was evaluated on the error plane partially within the BS and below the ship like in Figure 3.2.

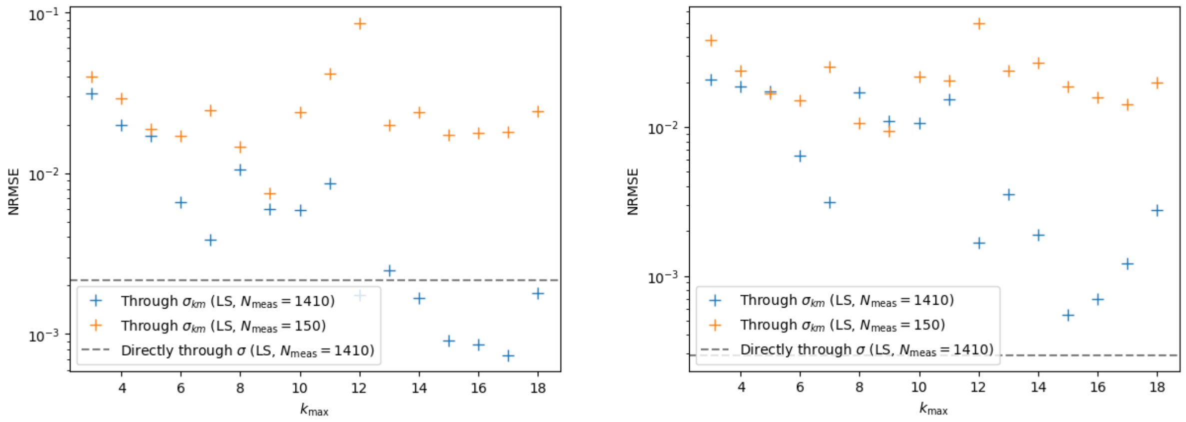

(a) NRMSE on the error plane partially within the BS.

(b) NRMSE on the error plane outside of the BS.

Figure 7.3: The NRMSE of the magnetic field $\mathbf{H}_{\mathrm{ind}}$ according to Equation (5.51), plotted against the varied order of approximation k_{max}. The CD σ was computed via the orthogonal basis vectors σ_{km}. The $N_{\mathrm{meas}} = 150$ or 1410 measurements were taken on the box of Figure 3.1. The used magnetic background field was $\mathbf{B}_0 = (23.360, 0, 41.234)\ \mu\mathrm{T}$. The NRMSE was computed on the error planes below the ship like in Figure 3.2. We also plot the NRMSE on the error plane below the ship, of the piecewise constant σ found using the method in Section 5.5.3 using $N_{\mathrm{meas}} = 1410$ measurements on the box shaped surface from Section 3.1.2. For $N_{\mathrm{meas}} = 150$, we sample the measurement points and compute the NRMSE 30 times. The mean value is given in the figures.

Even though the function $\tau^0_{k'm'}(\mathbf{r})$ is fully defined on each coordinate on S, and the matrix only needs to be derived once, we choose to approximate the integral by multiplying the centre value by the weight of the element. That is:

$$a_{ij} = \sum_{n=1}^{N_e} \sigma_{k(j)m(j)}(\mathbf{r}_{e_n}) \tau^0_{k'(i)m'(i)}(\mathbf{r}_{e_n}) w_n. \tag{7.5}$$

It turns out that this approximation works good in the cases within this thesis. In future research, especially when considering higher orders of the DSHE, it may make sense to compute the integral more precisely. At these higher orders, a greater variance will occur in τ^0_{km} per element, and the approximation might cause larger errors.

An important thing to note, is that the contribution of a basis function σ_{km} to the coefficient $a_{k'm'}$, with $k' > k$ is not zero. (Recall from the decay demand in Equation (6.3) that the exact opposite holds.). Therefore, it makes sense, to compute the $a_{k'm'}$ to a higher maximum order $k_{\mathrm{max},0}$, than the order up to which we computed the c_{km}: k_{max}. If this were not done, a lot of information stored in the basis vectors σ_{km} would be lost in the mapping to the DSHE.

In this thesis, we choose to continue this computation by 40 extra orders, after k_{max}. That means, $k_{\mathrm{max},0} = k_{\mathrm{max}} + 40$.

In Figure 7.4 it is very clear that truncating the DSHE at the same order as the multipolar basis on S, indeed loses a lot of information. The NRMSE is much bigger in that case. However, when we compute the DSHE up to the order $k_{\mathrm{max},0} = k_{\mathrm{max}} + 40$, the NRMSE is comparable to that of the magnetic field, computed using σ_{km} like in Section 7.1. For higher k_{max}'s, the found DSHE performs almost as good as the CD found directly according to the method from Section 5.5.3.

That the DSHE needs a higher order, than the multipolar basis on S, tells us that the shape of S holds a lot of information about the magnetisation as well. This makes sense, as we took the outer surface of the Albatros as S, and of course the shape of the Albatros has a big influence on the magnetisation of the ship. Alternatively, if we were modelling a dipole's magnetic field with a charge distribution on S, we would need many more terms of σ_{km} expansion, than we need of the DSHE.

For clarity, we do not use the DSHE in the rest of this thesis. We always compute the magnetic field directly from the c_{km} coefficients of the multipolar basis. We emphasise that we can easily map these

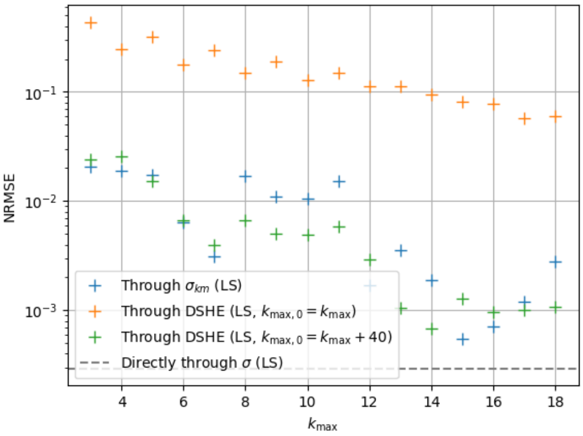

Figure 7.4: The NRMSE of the magnetic field $\mathbf{H}_{\mathrm{ind}}$ according to Equation (5.51), plotted against the varied order of approximation k_{max}. The CD σ was computed via the orthogonal basis vectors σ_{km}. The magnetic field was computed either using the σ_{km} basis functions, or its corresponding DSHE up to the same order k_{max}, or upto the order $k_{\mathrm{max}} + 40$. The $N_{\mathrm{meas}} = 1410$ measurements were taken on the box of Figure 3.1. The used magnetic background field was $\mathbf{B}_0 = (23.360, 0, 41.234)\ \mu\mathrm{T}$. The NRMSE was computed on the error plane outside of the BS and below the ship like in Figure 3.2. We also plot the NRMSE on the error plane below the ship, of the piecewise constant σ found using the method in Section 5.5.3 using $N_{\mathrm{meas}} = 1410$ measurements on the box shaped surface from Section 3.1.2.

coefficients to the DSHE, and obtain a similar error in the approximated magnetic field outside of the BS.

7.3. Introducing Noise

One of the reasons that we introduced the lower dimensional basis, is that it is less susceptible to noise. In the Figure 7.5 we show what happens to the NRMSE when adding noise to our measurements, both for the piecewise constant σ from Section 5.5.3, and the one built up of the multipolar basis on S.

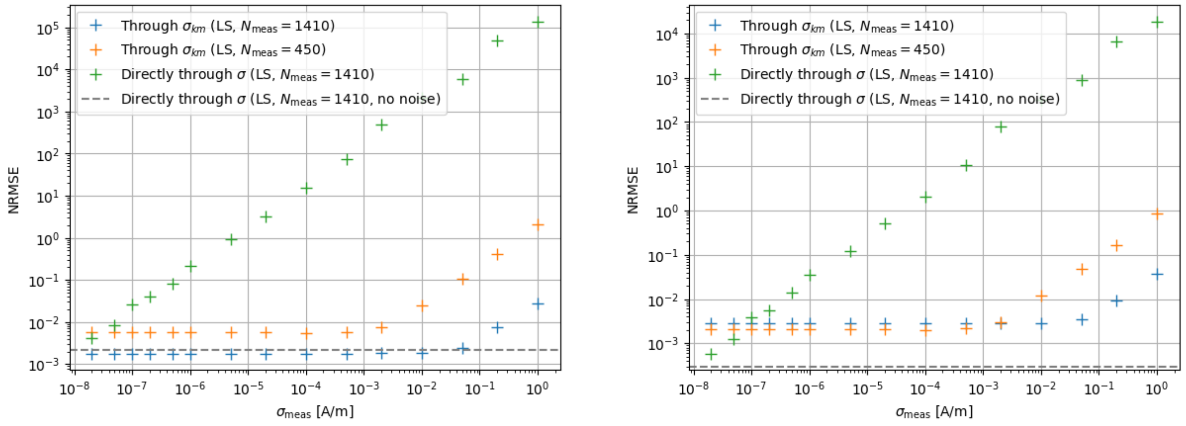

(a) NRMSE on the error plane partially within the BS.

(b) NRMSE on the error plane outside of the BS.

Figure 7.5: The NRMSE of the magnetic field $\mathbf{H}_{\mathrm{ind}}$ according to Equation (5.51), plotted against the varied measurement noise standard deviation σ_{meas}. The CD σ was computed via the orthogonal basis vectors σ_{km} with $k_{\mathrm{max}} = 18$, or by computing the piecewise constant σ using the method in Section 5.5.3. The $N_{\mathrm{meas}} = 450$ or 1410 measurements were taken on the box shaped surfaces of Figure 3.1. The used magnetic background field was $\mathbf{B}_0 = (23.360, 0, 41.234)\ \mu\mathrm{T}$. The NRMSE was computed on the error planes below the ship from Figure 3.2. We also plot the NRMSE on the error plane besides the ship, of the piecewise constant σ found using the method in Section 5.5.3 with no noise and $N_{\mathrm{meas}} = 1410$ measurements on the box shaped surface from Section 3.1.2.

As predicted, the lower dimensional basis, yields much better results when noise is added to the measurement vector $\mathbf{b}$.

The orange points in the figures, yield the results of using the multipolar basis on S, with only 450

measurements. The reason we chose $N_{\text{meas}} = 450$, is that for $k_{\max} = 18$, we need to determine $18 \times (18+2) = 360$ coefficients. We have not tested whether the system that we solve is full rank, but it probably is close to full rank, as there are significantly more measurements than unknowns.

Since the system of the orange points, is not as overdetermined as the blue points, the noise has a larger effect on the found coefficients. Around $\sigma_{\text{meas}} = 10^{-3}$ A/m, the NRMSE starts increasing. Typically, magnetic field measurements have a precision of 10 nT ≈ 0.008 A/m. If we take a 1% NRMSE as the minimum quality of our solution, this puts the orange points for such a noise, right at the edge of the minimum quality.

If we decrease N_{meas} even more, the NRMSE probably gets too big. Furthermore, changing the measurement locations might decrease the stability of the system we are inverting. Measurements too close to the surface S cannot be approximated well by the approximation performed in Equation (7.2). Measurements far away, or only at one side of the surface, might cause skewed solutions that only yield good predictions close to the measurements. We investigate these issues in Section 7.3.1, and propose a solution that is implemented in Chapter 8.

7.3.1. Varying the Measurement Locations

We now investigate the effect of changing the measurement locations. Besides the box at at least 1 m from the ship, we add a smaller box at at least 0.1 m, and the seabed introduced in Chapter 3. To check the quality of the predictions made using measurements at the seabed, we add two extra evaluation planes that are placed besides the ship, instead of underneath it. See Figure 7.6 for the measurement locations, and the new error planes.

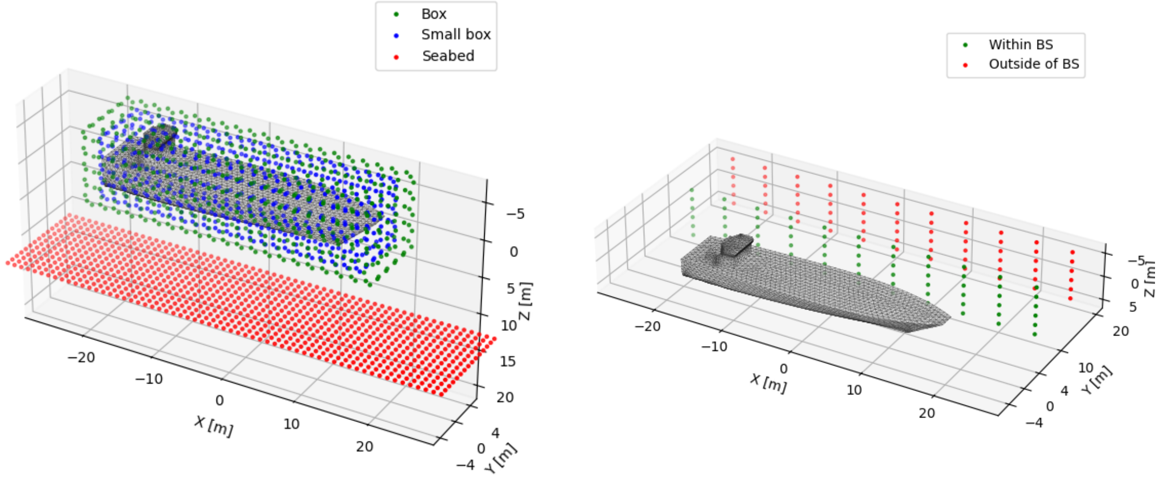

(a) The simplified geometry of the Albatros, and the simulation points used to find a source model of the ship. The green and red points are the same as in Figure 3.1. The blue points are on a box, that is at least at a distance of 0.1 m of the ship in all directions.

(b) The simplified geometry of the Albatros, and simulation points used to validate the found source model of the ship if the model was built using measurements on the seabed. The planes are the same size and shape as the ones in Figure 3.2.

Figure 7.6

We now again, vary the measurement noise, and compute the NRMSE. The NRMSE of the predictions made with the directly computed σ from 1410 measurements on the box from Chapter 3 is also given for comparison. Figure 7.7 shows the results for the small box, and the box from Chapter 3.

First of all, we see that the NRMSE of the model built with the measurements on the small box, is significantly larger, than that built with the measurements on the slightly larger box. This is probably caused by the approximations performed in Equation (7.2). Making this approximation more accurate is outside the scope of this thesis, but is recommended for future work.

Figure 7.8 shows the NRMSE of the model built with measurements on the seabed. The NRMSE was computed either on the error planes below the ship, from Chapter 3, or besides the ship like in Figure

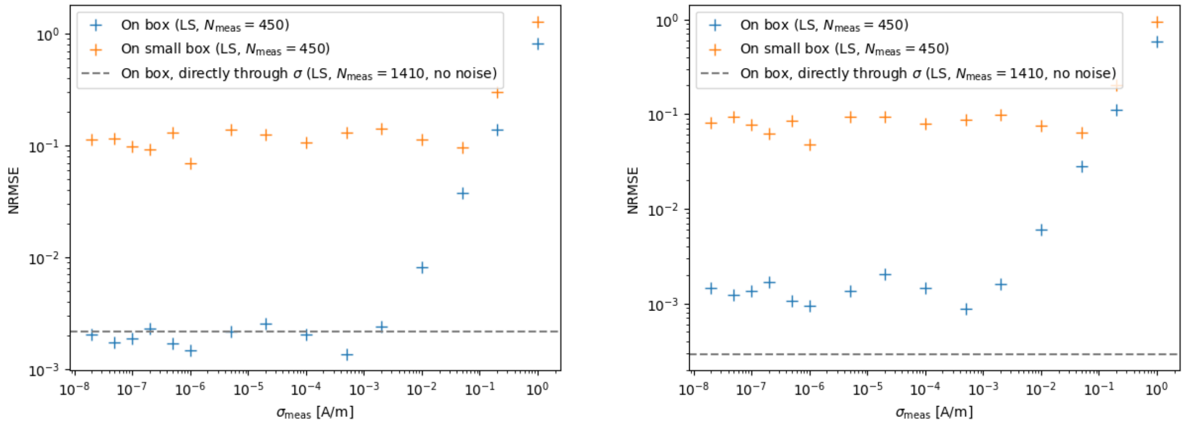

(a) NRMSE on the error plane partially within the BS.

(b) NRMSE on the error plane outside of the BS.

Figure 7.7: The NRMSE of the magnetic field $\mathbf{H}_{\text{ind}}$ according to Equation (5.51), plotted against the varied measurement noise standard deviation σ_{meas}. The CD σ was computed via the orthogonal basis vectors σ_{km} with $k_{\max} = 18$. The $N_{\text{meas}} = 450$ measurements were taken on the small and regular box shaped surfaces of Figure 7.6a. The used magnetic background field was $\mathbf{B}_0 = (23.360, 0, 41.234)$ μT. The NRMSE was computed on the error planes below the ship from Figure 3.2. We also plot the NRMSE on the error plane besides the ship, of the piecewise constant σ found using the method in Section 5.5.3 with no noise and $N_{\text{meas}} = 1410$ measurements on the box shaped surface from Section 3.1.2.

7.6b.

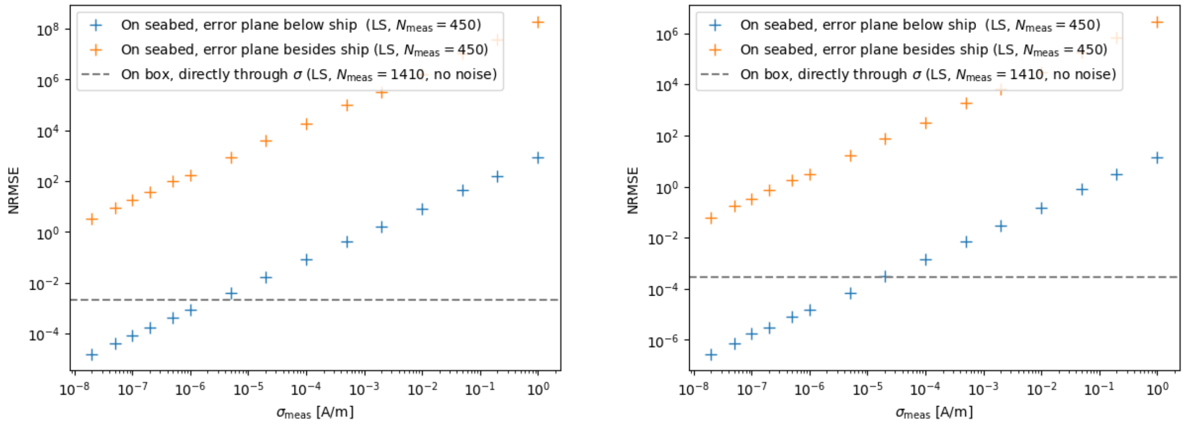

(a) NRMSE on the error plane partially within the BS.

(b) NRMSE on the error plane outside of the BS.

Figure 7.8: The NRMSE of the magnetic field $\mathbf{H}_{\text{ind}}$ according to Equation (5.51), plotted against the varied measurement noise standard deviation σ_{meas}. The CD σ was computed via the orthogonal basis vectors σ_{km} with $k_{\max} = 18$. The $N_{\text{meas}} = 450$ measurements were taken on the seabed of Figure 7.6a. The used magnetic background field was $\mathbf{B}_0 = (23.360, 0, 41.234)$ μT. The NRMSE was computed on the error planes besides the ship from Figure 7.6b, or below the ship like in Figure 3.2. We also plot the NRMSE on the error plane besides the ship, of the piecewise constant σ found using the method in Section 5.5.3 with no noise and $N_{\text{meas}} = 1410$ measurements on the box shaped surface from Section 3.1.2.

Clearly, the NRMSE on the error plane besides the ship is far too large, even for very small measurement noise. The NRMSE on the error planes close to the measurement points (so below the ship), is small. This tells us, that the model is overfit on the measurement data. The magnetic field generated by the found model, is probably quite non-typical for a ship.

Whether the model is or is not typical for a ship, can probably be seen from the c_{km} coefficients. If the background field is in a certain direction, we can probably expect a certain combination of coefficients to be larger. This means that the coefficients are not fully independent, and although the coefficients c_{km} live in $\mathbb{R}^{k_{\max}(k_{\max}+2)}$, the real solutions have a high probability of being found in a lower dimensional space. This is exactly what regularisation methods like Bayesian inference use, to find solutions with noisy or few measurements. Chapter 8 goes into these regularisation methods.

7.4. Non-Orthogonal Bases

In this section, we look into the option of using a non-orthogonal basis to find σ. First, we describe the differences between the orthogonal and non-orthogonal bases and introduce what non-orthogonal basis we use in this thesis. We show that we can continue the non-orthogonal basis to a higher order $k_{\max}$, but that these new basis functions do not improve the approximation of the magnetic field monotonously. We look into why the approximation does not improve monotonously, and link it to the limitations of the orthogonal basis as well. Finally, in Section 8.5 we look at applying Bayesian inference to the non-orthogonal basis.

Comment about notation

While referring to the orthogonal and non-orthogonal basis and their coefficients, we use the same notation for both: σ_{km} and c_{km}. This is done to improve the readability of the document. Note, that this does not mean that the bases and their coefficients are equal. They are explicitly unequal (except for the specific case where S is a spherical surface and the initial basis is already orthogonal).

7.4.1. Comparison to Orthogonal Basis

Our starting point of this section, is Equation (6.23). We repeat it below:

$$a_{k'm'}[\sigma] = a_{k'm'}[\tau] = \sum_{k=1}^{\infty} \sum_{m=-k}^{k} c_{km} \frac{\langle \sigma^0_{k'm'} \,|\, \sigma_{km} \rangle}{\alpha}.$$

Note that the summation over k runs from 1 to ∞. The truncation performed in Equation (6.26), is due to the decay property of the orthogonal basis, so this truncation is not allowed for a general non-orthogonal basis.

On the other hand, if we approximate σ with basis functions σ_{km} with $k \leq k_{\max}$, we can still truncate the sum to $k_{\max}$. Furthermore, to obtain a good NRMSE with the DSHE, we expect that we need to derive the $a_{k'm'}$ coefficients to the same order as we needed for the orthogonal basis. So in total, the orthogonal basis does not save much computational cost during the mapping from the multipolar basis on S, to the DSHE.

Another main difference between the orthogonal and non-orthogonal bases, is that the found coefficients c_{km} cannot be reused when we extend the basis to a higher $k_{\max}$. We need to re-compute all coefficients, when the basis is changed in size.

Finally, besides not being orthogonal, we can choose to normalise the basis or not. Our non-orthogonal basis is based on the initial basis vectors σ^0_{km} and τ^0_{km}. Recall from Equations (6.9) and (6.10) that these basis functions contain a r^k factor. As the surface S is not spherical, this means that for high orders of k the initial basis vectors span many orders of magnitudes. For example, for $k = 18$, at $r = 4$, we have $r^k \approx 6.9 \times 10^{10}$, while at $r = 18$ we have $r^k \approx 3.9 \times 10^{22}$. This large range cannot solved by normalising the basis functions, but we can make sure all the ranges are centred around 1.

We normalise the initial basis as follows, to find the non-orthogonal basis that is used in this chapter:

$$\sigma_{km} = \frac{\sigma^0_{km}}{||\sigma^0_{km}||}, \tag{7.6}$$

$$\tau_{km} = \frac{\tau^0_{km}}{||\tau^0_{km}||}. \tag{7.7}$$

Here the norm is still defined as in Equation (6.17).

7.4.2. Quality of a Larger Non-Orthogonal Basis

In Section 6.4.1, we saw that orthogonalisation issues occur around $k_{\max} = 18$. The idea of using a non-orthogonal basis, is that we avoid these issues, and are able to get to higher order approximations,

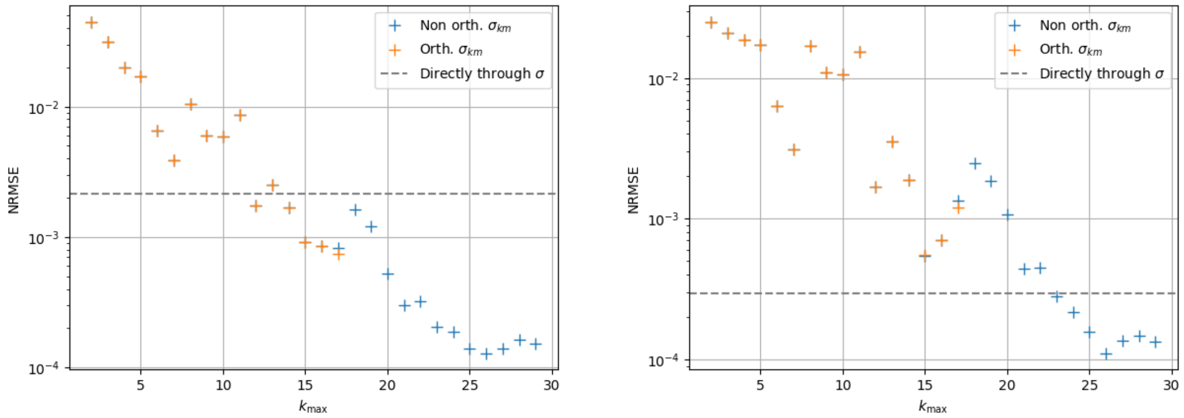

(a) NRMSE on the error plane partially within the BS.

(b) NRMSE on the error plane outside of the BS.

Figure 7.9: The NRMSE of the magnetic field $\mathbf{H}_{\text{ind}}$ according to Equation (5.51), plotted against the varied order of approximation $k_{\max}$. The CD σ was computed via the non-orthogonal basis vectors σ_{km}. The $N_{\text{meas}} = 1410$ measurements were taken on the box of Figure 3.1. The used magnetic background field was $\mathbf{B}_0 = (23.360, 0, 41.234)\,\mu\text{T}$. The NRMSE was computed on the error planes below the ship like in Figure 3.2. We also plot the NRMSE on the error plane below the ship, of the piecewise constant σ found using the method in Section 5.5.3 using $N_{\text{meas}} = 1410$ measurements on the box shaped surface from Section 3.1.2.

with smaller errors. Figure 7.9 shows the NRMSE of the benchmark problem defined in Chapter 3, for increasing $k_{\max}$. We add no noise, and compare the orthogonal and non-orthogonal bases.

In Figure 7.9 we see that the orthogonal and non-orthogonal basis perform equally as good for $k_{\max} \leq 18$.

Something that stands out, is that the orthogonalisation issues of the of the orthogonal basis, occur around the same order where the non-orthogonal basis increases in the NRMSE (see the bump in the NRMSE around $k_{\max} = 18$ in Figure 7.9). This leads us to question whether the issue is not the orthogonalisation process, but these specific basis functions and the way they are approximated on S. In future research, one could investigate what happens when the meshing on S is made more dense, or σ and τ are taken piecewise linear instead of piecewise smooth.

For the non-orthogonal basis, we can increase $k_{\max}$ even more, and see an improvement in the NRMSE for growing $k_{\max}$. The improvements begin to plateau for $k_{\max} > 25$, suggesting that the new basis vectors do not carry a lot of new information. To investigate this, we check whether a new basis function σ_{km} can be built up from all basis vectors $\sigma_{k'm'}$ before it (so with $k' < k$ or $k' = k$ and $m' < m$). We do this by building a matrix that contains all basis vectors up to the km-'th one:

$$A = \begin{bmatrix} \sigma_{1,-1} \\ \sigma_{1,0} \\ \vdots \\ \sigma_{k,m-1} \end{bmatrix}. \tag{7.8}$$

Note that this equation is for illustration purposes, and if $m = -k$ the last basis vector in A is $\sigma_{k-1,k-1}$. The vector $\mathbf{b}$ contains all entries of the basis vector σ_{km}. We now compute $\mathbf{x} = \arg\min_{\mathbf{x}} ||A\mathbf{x} - \mathbf{b}||_2$ and plot the relative residual:

$$\text{residual} = \frac{||A\mathbf{x} - \mathbf{b}||_2}{||\mathbf{b}||_2}. \tag{7.9}$$

This residual tests how linearly independent the new vector is, with respect to the old vectors. It can be seen as a measure for how much information is added to the basis, by adding the new basis vector.

For the orthogonal base, we perform this computation for $k \leq 18$, and for the non-orthogonal base we perform the computation for $k \leq 30$. The result is given in Figure 7.10.

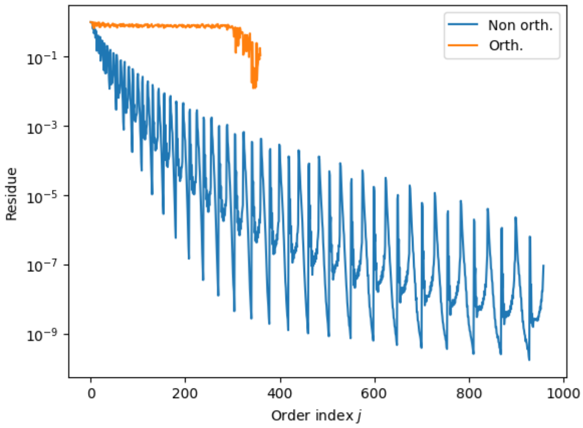

Figure 7.10: The relative residual that checks whether a new basis vector σ_{km} can be built from the previous basis vectors. This is done both for the orthogonal basis from Chapter 6 as well as the non-orthogonal basis computed introduced in Section 7.4. The residual is computed with equation 7.9.

There are three things to note about Figure 7.10. First, we see that for j less than approximately 300, the relative residual of a new basis vector of the orthogonal basis is 1. What this means, is that $||A\mathbf{x} - \mathbf{b}||_2 = ||\mathbf{b}||_2$. If a new vector is orthogonal to all previous vectors, the least squares solution to $A\mathbf{x} = \mathbf{b}$ is $\mathbf{x} = \mathbf{0}$. Then indeed, we have $||A\mathbf{x} - \mathbf{b}||_2 = ||\mathbf{b}||_2$. (The reasoning in the other direction leans on orthogonality properties that are outside of the scope of this thesis.) So we conclude that the basis vectors, for the most part, are indeed orthogonal to each other, but lose some orthogonality in the higher orders.

Secondly, we look at the residual of the non-orthogonal basis. Since the vectors are not orthogonalised, of course this residual is not 1. A new vector might contain a new direction in the solution space, but a part of it can be expressed by the previous basis vectors. It turns out, that although the initial basis vectors are projections of the orthogonal DSHE functions, the part of the new basis vector that is orthogonal to the previous basis vectors, decreases in size as j increases.

This result is not surprising, but it does explain that the orthogonal parts of the vectors, are containing increasing numerical errors, and that the NRMSE of Figure 7.9 does not decrease as steeply after $k_{\max} \approx 25$.

Finally, we note that a pattern is present in the residue of the non-orthogonal basis. The pattern starts at $j = 1$ and repeats when the order index represents a new order k, so at $j = k(k+2)+1$ for $k = 1, 2, \ldots, 30$. That is $j = 4, 9, 16, \ldots, 784, 841, 900$. The residue appears to peak at the onset of each new order k, which is consistent with the introduction of a new spatial frequency in the basis vectors. However, the residue does not decrease monotonously when the other basis vectors within that order are incorporated. Investigating why this pattern occurs, is outside of the scope of this thesis.

Introducing noise

In Section 8.5 we show that adding noise has approximately the same effect on the non-orthogonal basis, as it does on the orthogonal basis. That is, the non-orthogonal basis also needs a regularisation method to deal with noise and badly distributed measurements. In this section, we also implement Bayesian inference as it is introduced in the start of Chapter 8.

8

Dealing with Noise using Bayesian Inference

In Chapter 7 we saw that the model is sensitive to noise, and if we want to decrease N_{meas} even more than in Chapter 7, the NRMSE probably gets too big. More importantly, we saw that if measurements are used that are not spread out well, the model overfits to those measurements, and leads to large errors in other regions. We concluded that this overfitting, might be solved by decreasing the solution space with a regularisation method like Bayesian inference.

In Bayesian inference, regularisation can be added to an underdetermined system, while doing it in a way that is motivated by physics. In this chapter we first introduce Bayesian inference theoretically, and then explain how this relates to our matrix vector problem. As we'll see in Section 8.1, a singular matrix appears that needs to be inverted. This issue is be solved by performing a Principle Component Analysis (PCA) to reduce the order of the model. Lastly we introduce the Unscented Transform, which helps us pick the samples we need for Bayesian inference.

8.1. Bayesian Inference

In Bayesian inference, we are looking for unknown parameters in a vector $\mathbf{x}$, which in our case are the coefficients c_{km}. Furthermore, we need some known parameters in a vector $\mathbf{b}$, which in our case is the measurement vector $\mathbf{b}$.

As the name suggests, Bayesian inference is based on Bayes theorem. For a given measurement vector $\mathbf{b}$, we want to find the parameters $\mathbf{x}$, for which the posterior probability density $p(\mathbf{x}|\mathbf{b})$ is maximal. This is the Maximum A Posteriori estimate. By Bayes theorem we have

$$p(\mathbf{x}|\mathbf{b}) = \frac{p(\mathbf{b}|\mathbf{x})p(\mathbf{x})}{p(\mathbf{b})}. \tag{8.1}$$

If we assume the prior $p(\mathbf{x})$ and the measurement information $p(\mathbf{b}|\mathbf{x})$ to be Normally distributed. We then have that $p(\mathbf{b}) = \int_{\mathbb{R}} p(\mathbf{b}|\mathbf{x}')p(\mathbf{x}')\mathrm{d}\mathbf{x}'$ is Normally distributed as well. Now by [21, pp. 65-66] the Maximum A Posteriori estimate is defined by:

$$\begin{aligned} \mathbf{x}_{\text{MAP}} &= \arg\min_{\mathbf{x}} (A\mathbf{x} - \mathbf{b})^T S_{\mathbf{b}|\mathbf{x}}^{-1} (A\mathbf{x} - \mathbf{b}) + (\mathbf{x} - \overline{\mathbf{x}})^T S_{\mathbf{x}}^{-1} (\mathbf{x} - \overline{\mathbf{x}}) \\ &= (A^T S_{\mathbf{b}|\mathbf{x}}^{-1} A + S_{\mathbf{x}}^{-1})^{-1} (A^T S_{\mathbf{b}|\mathbf{x}}^{-1} \mathbf{b} + S_{\mathbf{x}}^{-1} \overline{\mathbf{x}}). \end{aligned} \tag{8.2}$$

Here $S_{\mathbf{b}|\mathbf{x}}$ is the covariance matrix of the measurements $\mathbf{b}$, $S_{\mathbf{x}}$ the covariance matrix of the unknown parameters $\mathbf{x}$, and $\overline{\mathbf{x}}$ their mean. Furthermore, $(A^T S_{\mathbf{b}|\mathbf{x}}^{-1} A + S_{\mathbf{x}}^{-1})^{-1} = S_{\mathbf{x}|\mathbf{b}}$ is the posterior covariance matrix, and $A^T S_{\mathbf{b}|\mathbf{x}}^{-1} \mathbf{b} + S_{\mathbf{x}}^{-1} \overline{\mathbf{x}}$ the posterior information vector.

The measurements are assumed to be independent, and contain measurement noise and errors of mean 0 and standard deviation $\sigma_{\mathbf{b}} = \sigma_{\text{meas}}$. This yields $S_{\mathbf{b}|\mathbf{x}} = \sigma_{\mathbf{b}}^2\,\text{Id}$. Determining $S_{\mathbf{x}}$ and $\overline{\mathbf{x}}$ is less straight forward, as it is not obvious what the mean, variance and covariance of the parameters $\mathbf{x}$ are.

To solve this issue, we find parameters for which we can reasonably assume a distribution. We take samples of these parameters, and use a model or data to determine the distribution of the unknown parameters $\mathbf{x}$.

In the simplest case, we only vary the background field $\mathbf{B}_0$. We assume it has a normal distribution with mean $(0, 1, 0)$ μT and standard deviation 20 μT. (In a more realistic case, the relative magnetic permeability $\mu_{r,\text{ind}}$ of the ships material are varied as well, or the permanent magnetisation can be modelled in some way. More details on this are given in Section 8.2.3.) Then the MoM of TNO is used to compute the magnetic field at any necessary points. As we are performing a forward computation, we can take as many measurements as needed at any location. Because of this, and the fact that the measurements are without noise, the measurement vectors can be used to find the unknown parameters c_{km} for each sample by solving $A\mathbf{x} = \mathbf{b}$ with a least squares solver (or using another regularisation method).

Now using the found samples of c_{km}, we can find their average $\overline{\mathbf{x}}$, and their covariance matrix $S_{\mathbf{x}}$. This allows us to compute the MAP estimate $\mathbf{x}_{\text{MAP}}$ for a given measurement vector $\mathbf{b}$ using Equation (8.2). A schematic overview of finding and using the Prior is given in Figure 8.1

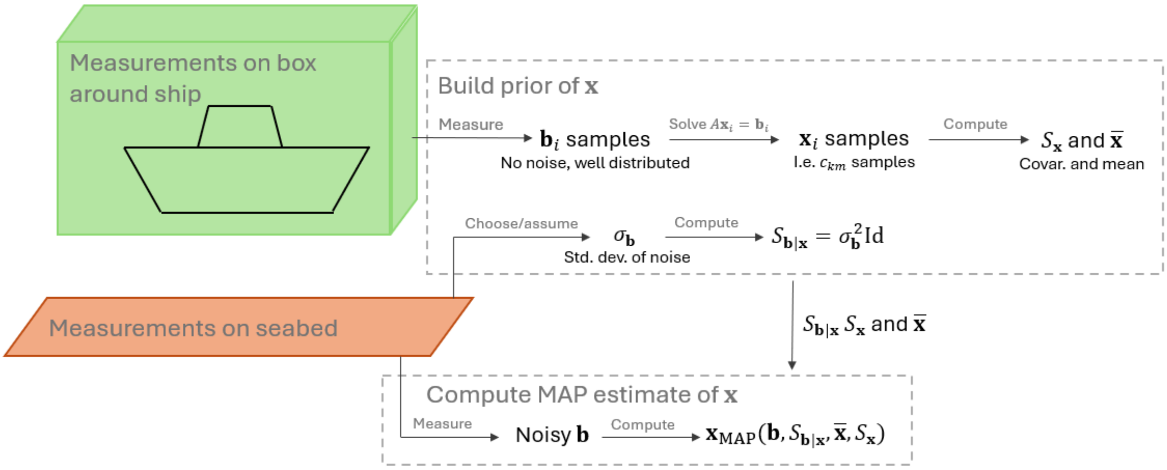

Figure 8.1: A schematic overview of how to find and use a prior in Bayesian inference. The green box and the orange parallelogram represent the measurement surfaces from Figure 3.1. The measurements on the green box are used to build the prior. Then we compute $\mathbf{x}_{\text{MAP}}$ using measurements on the seabed.

8.2. Issues and Details of Bayesian Inference

There are multiple issues and details that need to be clarified for the method described in Section 8.1. The first, and most important issue, is that the covariance matrix $S_{\mathbf{x}}$ is singular, and we are performing an inversion of it in Equation (8.2). This is solved using a Principle Component Analysis. Another detail that needs clarification, is how the samples are taken to find $S_{\mathbf{x}}$ and $\overline{\mathbf{x}}$. This is done using an Unscented Transform. The last issue regards how our model can be made more realistic, by taking into account the relation between the background field $\mathbf{B}_0$, and the coefficients $\mathbf{x}$, varying the magnetic permeability of the ship, and adding a permanent magnetisation to the ship.

In this section these solutions and details are explained.

8.2.1. Singularity of $S_{\mathbf{x}}$: Principle Component Analysis

In Equation (8.2), an inversion of $S_{\mathbf{x}}$ occurs. As the MoM is a linear model, when we only vary the 3-dimensional background field $\mathbf{B}_0$, the found samples of $\mathbf{x}$ are all linear combinations of three basis vectors. Therefore the covariance matrix $S_{\mathbf{x}}$ has rank 3. If the order of approximation is $k_{\max}$, then c_{km} (i.e. $\mathbf{x}$) is $k_{\max}(k_{\max}+2)$ long, and $S_{\mathbf{x}}$ is shaped $k_{\max}(k_{\max}+2) \times k_{\max}(k_{\max}+2)$. Therefore, for any reasonable $k_{\max}$, $S_{\mathbf{x}}$ is not invertible. In Section 8.2.3 five more dimensions to vary are introduced besides the background field $\mathbf{B}_0$. This causes in increase in the rank of $S_{\mathbf{x}}$, however $S_{\mathbf{x}}$ is then still not full rank.

Furthermore, since the entries of A depend on the positions of the measurements, it can occur that the system $A\mathbf{x} = \mathbf{b}$ is rank-deficient. This can even be the case when there are many more measurements in $\mathbf{b}$, than coefficients in $\mathbf{x}$. If this is the case, $A^T S_{\mathbf{b}|\mathbf{x}}^{-1} A$ is also singular.

A first idea to solve the inversion of the rank deficient $S_{\mathbf{x}}$ and $A^T S_{\mathbf{b}|\mathbf{x}}^{-1} A + S_{\mathbf{x}}$, is to replace it by a Moore-Penrose pseudo-inverse. A Moore-Penrose pseudo-inverse reduces the dimensions in which a solution is found, to the dimensions with eigenvalues that are not close to zero. Although this is in line with what we want, it turns out that this pseudo-inverse does not yield good results. The unpredictability of the use of this pseudo-inverse can be explained by the fact that the inversion of $S_{\mathbf{x}}$ occurs twice in Equation (8.2), of which one is within another inversion. To reason whether we expect a good result using this pseudo inverse is not straightforward. Therefore we try another method of dimension reduction, that behaves more predictably: Principle Component Analysis (PCA).

PCA is used when many parameters are redundant, and the dimensionality needs to be reduced [3, pp. 118-120]. This is exactly the case, as our vector $\mathbf{x}$ is $k_{\max}(k_{\max}+2)$ long, but appears to be a combination of just $r \ll k_{\max}(k_{\max}+2)$ basis vectors.

Instead of finding $\mathbf{x}_{\mathrm{MAP}}$, we find $\mathbf{z}_{\mathrm{MAP}} \in \mathbb{R}^r$. A precise derivation is given in Appendix A.4. The derivation yields

$$\mathbf{x}_{\mathrm{MAP}} = \overline{\mathbf{x}} + V_0\, \mathbf{z}_{\mathrm{MAP}}, \tag{8.3}$$

$$\begin{aligned} \mathbf{z}_{\mathrm{MAP}} &= \arg\min_{\mathbf{z}} (A_{\mathbf{z}}\mathbf{z} - \mathbf{b}_{\mathbf{z}})^T S_{\mathbf{b}|\mathbf{z}}^{-1} (A_{\mathbf{z}}\mathbf{z} - \mathbf{b}_{\mathbf{z}}) + \mathbf{z}^T \Lambda_0^{-1} \mathbf{z} \\ &= (A_{\mathbf{z}}^T S_{\mathbf{b}|\mathbf{z}}^{-1} A_{\mathbf{z}} + \Lambda_0^{-1})^{-1} \, (A_{\mathbf{z}}^T S_{\mathbf{b}|\mathbf{z}}^{-1} \mathbf{b}_{\mathbf{z}}), \end{aligned} \tag{8.4}$$

where V_0 are the eigenvectors of $S_{\mathbf{x}}$ that have a non-zero eigenvalue, Λ_0 is the diagonal matrix containing these non-zero eigenvalues, $A_{\mathbf{z}} = AV_0$, $\mathbf{b}_{\mathbf{z}} = \mathbf{b} - A\overline{\mathbf{x}}$, and $S_{\mathbf{b}|\mathbf{z}} = S_{\mathbf{b}|\mathbf{x}}$.

MAP estimate vs least squares estimate of $\mathbf{z}$

In some cases, the eigenvalues within Λ_0 can be very large. In the limit case ($\lambda_i \to \infty$), the MAP estimate $\mathbf{z}_{\mathrm{MAP}}$ is equal to the least squares estimate $\mathbf{z}_{\mathrm{LS}}$ of the equation $A_{\mathbf{z}}\mathbf{z} = \mathbf{b}_{\mathbf{z}}$. Appendix A.5 gives a proof of this claim.

An example of this is when we only vary the background field $\mathbf{B}_0$, using a small mean and large variance. We found that indeed the MAP and LS estimates are (almost) equal to each other. It is outside of the scope of this thesis to derive when the eigenvalues are large enough such that this is, or is not the case. Therefore, we stick to using the MAP estimate $\mathbf{z}_{\mathrm{MAP}}$ in our algorithms.

8.2.2. Sampling Method: The Unscented Transform

Let us say we have N variables that we assume to behave according to specific Normal distributions. As discussed at the end of Section 8.1, an example of these variables are the three components of the background field $\mathbf{B}_0$ and the relative magnetic permeability $\mu_{r,\mathrm{ind}}$. In that case $N = 4$, and the transformation from these parameters to the unknown parameters $\mathbf{x}$ is non-linear in $\mu_{r,\mathrm{ind}}$. To approximate the covariance matrix $S_{\mathbf{x}}$ and mean $\overline{\mathbf{x}}$ of the unknown parameters $\mathbf{x}$, we need to take samples of the N variables and perform computations to find samples of $\mathbf{x}$. One could take many random samples, and derive the properties of the Normal distribution of $\mathbf{x}$ that way. However, [15] introduces the Unscented Transform, a method that does not take random samples, but selects them according to a deterministic algorithm. This way, for N variables, one only needs to take $2N+1$ samples to find the mean and covariance matrix of the distribution of the unknown variables $\mathbf{x}$.

Using the unscented transform saves computational time. Without the unscented transform, one would need many samples to fully transfer the distribution of $\mathbf{B}_0$ and $\mu_{r,\text{ind}}$ to the prior $S_\mathbf{x}$. With the unscented transform we need only $2N+1=9$.

This is especially saves computational time when one is investigating which measurement locations lead to the best prior $S_\mathbf{x}$, and thus to the best $\mathbf{x}_\text{MAP}$ estimates. Every time one wants to try out a new combination of measurement locations, $S_\mathbf{x}$ needs to be computed through new samples. For each new new relative magnetic permeability, or measurement location, the MoM needs to be rerun. By using the unscented transform, we need only 3 relative magnetic permeabilities $\mu_{r,\text{ind}}$ per $S_\mathbf{x}$, and thus save a lot of time, compared to taking many samples. (Once the measurement locations are decided, another sampling method could also be used, as $S_\mathbf{x}$ only needs to be computed once.) In this Section, the method is described according to [15].

As stated, we start with an N-dimensional random variable $\mathbf{y}$. Which in the example above consists of the three components of the background field $\mathbf{B}_0$ and the relative magnetic permeability $\mu_{r,\text{ind}}$. For these variables we assume a mean $\overline{\mathbf{y}}$ and a covariance matrix $S_\mathbf{y}$. In our case, there is no correlation between the variables, so the covariance matrix is the diagonal matrix containing the variation of the variables. The $2N+1$ samples that are taken, and their corresponding weights, are given by:

$$\begin{aligned} \mathbf{y}_0 &= \overline{\mathbf{y}} & W_0 &= \tfrac{\kappa}{N+\kappa} \\ \mathbf{y}_i &= \overline{\mathbf{y}} + \left(\sqrt{(N+\kappa)S_\mathbf{y}}\right)_i & W_i &= \tfrac{1}{2(N+\kappa)} \\ \mathbf{y}_{i+N} &= \overline{\mathbf{y}} - \left(\sqrt{(N+\kappa)S_\mathbf{y}}\right)_i & W_{i+N} &= \tfrac{1}{2(N+\kappa)}. \end{aligned} \tag{8.5}$$

κ can be tuned to reduce errors. However, as we assumed all variables in $\mathbf{y}$ to be Gaussian, we take $N+\kappa=3$ as prescribed by [15]. For example, if $N=4$, we get $\kappa=-1$. We now compute the samples $\mathbf{x}_i$ as described in Section 8.1, and compute $\overline{\mathbf{x}}$ and $S_\mathbf{x}$ as follows:

$$\overline{\mathbf{x}} = \sum_{i=0}^{2N} W_i \mathbf{x}_i, \tag{8.6}$$

$$S_\mathbf{x} = \sum_{i=0}^{2N} W_i (\mathbf{x}_i - \overline{\mathbf{x}})(\mathbf{x}_i - \overline{\mathbf{x}})^T. \tag{8.7}$$

8.2.3. Realistic Modelling

In this section three ways are discussed, to improve the realism of the modelling.

Adding the background field $\mathbf{B}_0$ to the variable vector $\mathbf{x}$

The components of the background field $\mathbf{B}_0$ do not need to be computed, as they are known. In general, when modelling the induced magnetic field, one would subtract the background field from the measurements, to focus solely on the induced component. However, in Bayesian inference we are very interested in the covariance between all components in the variable vector $\mathbf{x}$. In particular, the c_{km} coefficients are highly correlated with the background field $\mathbf{B}_0$. Therefore, we extend the variable vector $\mathbf{x}$ with the three components of the background field, and correspondingly extend the covariance matrix $S_\mathbf{x}$ to account for the correlations between these components and the c_{km} coefficients.

Varying the relative magnetic permeability $\mu_{r,\text{ind}}$

Besides a varying background field, the relative magnetic permeability is also a variable. The MoM assumes that the permeability is constant on the entire geometry. This can already be critiqued, as the permeability can vary per steel plate on the ship, but we do not discuss this in this thesis. If we continue with the assumption that the permeability is constant on the entire geometry, the exact permeability is still not known, and might vary over time, due to the current circumstances (like temperature and background field), or hysteresis. Therefore the relative magnetic permeability is also varied, and samples are taken according to the Unscented Transform. As the permeability is unknown in reality, this variable is not added to the variable vector $\mathbf{x}$.

Modelling the permanent magnetisation

Lastly, as stated in Section 2.4, we are interested in the permanent magnetisation of a ship. The permanent magnetisation is very hard to model, as it is not known how it comes into existence exactly. One theory is that the permanent magnetisation is a combination of all induced magnetisations that the ship has had in the past. Therefore, a reasonable way to model the permanent magnetisation, is by computing an induced field $\mathbf{B}_{\text{ind,perm}}$ with the MoM, using a new magnetising permeability $\mu_{r,\text{perm}}$ and background field $\mathbf{B}_{0,\text{perm}}$. In this case we only use the induced field, and ignore the background field, as the background field occurred in the past. The measured magnetic field becomes:

$$\mathbf{B} = \mathbf{B}_0 + \mathbf{B}_{\text{ind}} + \mathbf{B}_{\text{ind,perm}}. \tag{8.8}$$

Similarly to $\mu_{r,\text{ind}}$, we also do not add $\mu_{r,\text{perm}}$ and $\mathbf{B}_{0,\text{perm}}$ to the variable vector $\mathbf{x}$, as they are not known in reality.

The permanent magnetic permeability that we use is $\mu_{r,\text{perm}} = 2000$. The 'background field' that we use is differently oriented in the yz-direction, instead of xz-direction like the one used for the induced magnetic field. We use $\mathbf{B}_{0,\text{perm}} = (0, 23.360, -24.740)\,\mu$T or $\mathbf{H}_{0,\text{perm}} = \mathbf{B}_{0,\text{perm}}/\mu_0 = (0, 18.589, -19.688)$ A/m.

[7] used this method to model the permanent magnetisation in their prior, and got good results when they applied it to physical measurements. There are theories that the permanent magnetisation can also be caused by large forces that occur during the production of the ship or other circumstances. These kinds of magnetisations have not been included in our prior, but could be interesting in future research.

Table 8.1 shows the means and standard deviations used to build the prior, when we vary $\mathbf{B}_0$, $\mathbf{B}_{0,\text{perm}}$, $\mu_{r,\text{ind}}$ and $\mu_{r,\text{perm}}$.

Parameter	Mean	Standard deviation
$\mathbf{B}_{0,\mathbf{x}}$	$0\,\mu\text{T}$	$20\,\mu\text{T}$
$\mathbf{B}_{0,\mathbf{y}}$	$1\,\mu\text{T}$	$20\,\mu\text{T}$
$\mathbf{B}_{0,\mathbf{z}}$	$0\,\mu\text{T}$	$20\,\mu\text{T}$
$\mu_{r,\text{ind}}$	200	10
$\mathbf{B}_{0,\text{perm},\mathbf{x}}$	$0\,\mu\text{T}$	$20\,\mu\text{T}$
$\mathbf{B}_{0,\text{perm},\mathbf{y}}$	$0\,\mu\text{T}$	$20\,\mu\text{T}$
$\mathbf{B}_{0,\text{perm},\mathbf{z}}$	$-1\,\mu\text{T}$	$20\,\mu\text{T}$
$\mu_{r,\text{perm}}$	2000	500

Table 8.1: The means and standard deviation of the parameters that are varied to build the prior $S_{\mathbf{x}}$.

8.3. Comparison to Least Squares

In this section, we see if the overfitting issues, of using measurements on the seabed, can be solved using Bayesian inference. We apply Bayesian inference, and compute the NRMSE on the error planes besides the Albatros, like in Figure 7.6b. We compare it to the NRMSE found by using a LS solver. Finally, we also decrease the number of measurements N_{meas}, to see if this is indeed possible when using Bayesian inference. The result is given in Figure 8.2.

Note that the measurement noise starts at $\sigma_{\text{meas}} = 10^{-6}$, instead of $\sigma_{\text{meas}} = 10^{-8}$. This is done, as the inversion of $S_{\mathbf{b}|\mathbf{x}}$ causes large numerical instabilities when σ_{meas} becomes too small. Furthermore, suppose we let $\sigma_{\text{meas}} \to 0$, then Bayesian inference simplifies to a least squares solver. The derivation for this is similar to that in Appendix A.5, and is given in Appendix A.6.

After applying Bayesian inference, the NRMSE has become much smaller again. Even when using $N_{\text{meas}} = 150$ measurements, and high levels of noise, the NRMSE stays below 10%. Such an NRMSE is very reasonable for the fact that we used badly distributed measurements, far from the error planes. Bayesian inference thus works very well to prevent overfitting on measurements in a specific region. It also lowers the dimension of the solution space, allowing us to use less measurement data.

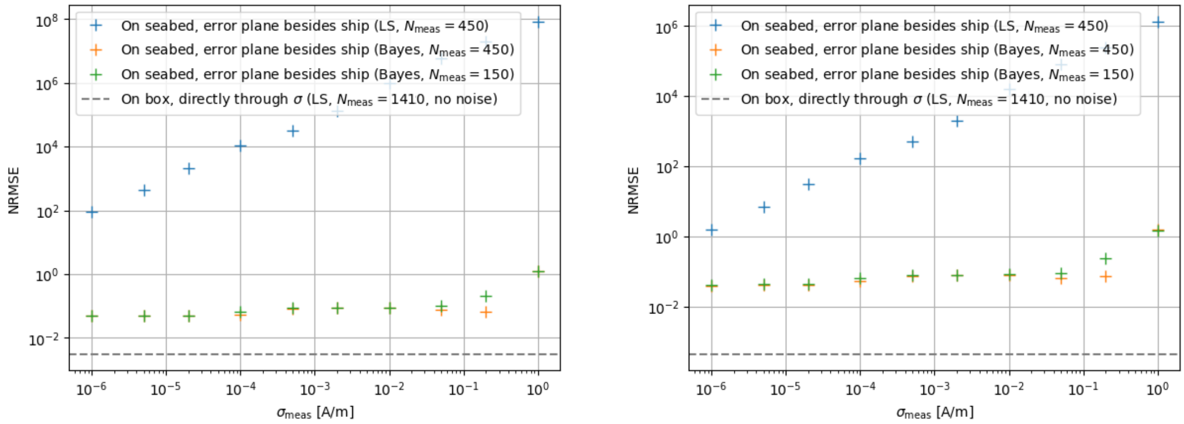

(a) NRMSE on the error plane partially within the BS.

(b) NRMSE on the error plane outside of the BS.

Figure 8.2: The NRMSE of the magnetic field $\mathbf{H} = \mathbf{H}_{\text{ind}} + \mathbf{H}_{\text{ind,perm}}$ according to Equation (5.51), plotted against the varied measurement noise standard deviation σ_{meas}. The CD σ was computed via the orthogonal basis vectors σ_{km} using a least squares solver, or Bayesian inference with PCA and $k_{\max} = 18$. We used the 10 first basis vectors during the PCA of the prior $S_{\mathbf{x}}$. The Bayesian inference prior was built using measurements on the box shaped surface from Section 3.1.2. The $N_{\text{meas}} = 150$ or 450 measurements were taken on the seabed of Figure 7.6a. The used magnetic background fields were $\mathbf{B}_0 = (23.360, 0, 41.234)\ \mu\text{T}$ and $\mathbf{B}_{0,\text{perm}} = (0, 23.360, -24.740)\ \mu\text{T}$. The NRMSE was computed on the error planes besides the ship from Figure 7.6b. We also plot the NRMSE of the piecewise constant σ found using the method in Section 5.5.3 with no noise and $N_{\text{meas}} = 1410$ measurements on the box shaped surface from Section 3.1.2.

8.4. Drawbacks of Bayesian Inference

Using a prior creates bias in the found solutions. The bias is based on the assumptions made when building the samples. The prior we used, is fully based on the Albatros. Finding the source model of an unknown ship in a detection setting, might pose to be a bigger challenge. An extreme illustration of this, is given in Appendix B.1. Here the prior is built, by only varying the background magnetic field $\mathbf{B}_0$ (so there is not permanent magnetisation, and the magnetic permeability is also kept constant). In that case, the solution space its dimension is reduced to 3, and the entire computation of $\mathbf{x}$ basically becomes a linear mapping from the background field $\mathbf{B}_0$, to the corresponding coefficients c_{km} within the 3-dimensional solution space. If we then do not follow the assumptions used when building the prior, by removing the ship and its induced field, the found solution will be completely wrong.

This overfitting on the assumptions of the prior, is a natural and logical effect of Bayesian inference. We therefore do not see it as an issue that needs to be solved. However, it should be noted, that the samples used to build a prior, should include all situations that are reasonable to occur in practice. That is, all variables that occur in practice, should be included in the variables of the unscented sampling.

One could argue that a simpler or simplified regularisation method, such as Tikhonov regularisation, might prevent such overfitting. A simpler method might also be easier to implement. During this thesis, we shortly looked into implementing Tikhonov Regularisation, which is a specific case of Bayesian inference. During Tikhonov Regularisation, one parameter needs to be chosen. There are many ways to choose this parameter, of which some are computationally expensive and not feasible within an application like this thesis. In Appendix B.2 we try to apply Tikhonov regularisation with a computationally cheap plug-in parameter. We find that the regularisation improves the NRMSE compared to the least squares solver, but is outperformed by Bayesian inference when the noise gets to reasonable levels. In future research, it might make sense to try to find a better Tikhonov parameter, which might solve this issue. One could also use the current (or improved) method, to complement Bayesian inference when it is not yielding good results. For example when the assumptions made in the prior, are not satisfied in the measurements.

8.5. Adding Noise to the Non-Orthogonal Basis

Finally, we look at how the non-orthogonal basis deals with noise, and whether it works as good as the orthogonal basis when using Bayesian Inference. In Section 7.4 we showed that the NRMSE can be decreased more by increasing the order of approximation $k_{\max}$ of the non-orthogonal basis. However, to keep the comparison between the orthogonal and non-orthogonal bases simple, we stick to $k_{\max} = 18$ for both bases in this section. Comparing the results of Bayesian inference with a lower $k_{\max}$ to that with a higher $k_{\max}$ is outside of the scope of this thesis, is recommended to investigate in future work.

We first 'naively' compute the least squares solutions and regular Bayesian inference solution with PCA. The measurements are taken on the seabed surface from Figure 3.1, and the error is evaluated on the error planes from Figure 7.6b. The result is given in Figure 8.3.

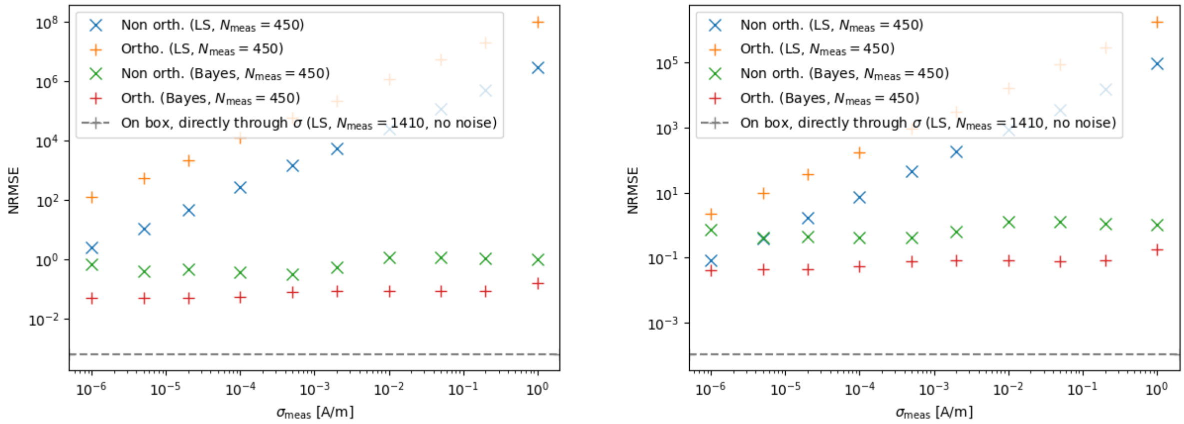

(a) NRMSE on the error plane partially within the BS.

(b) NRMSE on the error plane outside of the BS.

Figure 8.3: The NRMSE of the magnetic field $\mathbf{H} = \mathbf{H}_{\text{ind}} + \mathbf{H}_{\text{ind,perm}}$ according to Equation (5.51), plotted against the varied measurement noise standard deviation σ_{meas}. The CD σ was computed via the non-orthogonal or orthogonal basis vectors σ_{km} using a least squares solver, or Bayesian inference with PCA and $k_{\max} = 18$. For the orthogonal basis we used the 10 first basis vectors during the PCA of the prior $S_{\mathbf{x}}$. For the non-orthogonal we used the first 7 only. The Bayesian inference prior was built using measurements on the box shaped surface from Section 3.1.2. The $N_{\text{meas}} = 450$ measurements were taken on the seabed of Figure 7.6a. The used magnetic background fields were $\mathbf{B}_0 = (23.360, 0, 41.234)\ \mu\text{T}$ and $\mathbf{B}_{0,\text{perm}} = (0, 23.360, -24.740)\ \mu\text{T}$. The NRMSE was computed on the error planes besides the ship from Figure 7.6b. We also plot the NRMSE of the piecewise constant σ found using the method in Section 5.5.3 with no noise and $N_{\text{meas}} = 1410$ measurements on the box shaped surface from Section 3.1.2.

We see that the non-orthogonal basis yields better results when using a least squares solver. However, the error is still much to large. Therefore we indeed need extra regularisation when noise is added or when measurements are badly distributed, just like the orthogonal basis needs this.

When we "naively" apply Bayesian inference with PCA to the non-orthogonal basis (i.e. letting the NumPy function `numpy.linalg.matrix_rank` determine the rank without extra settings), the NRMSE is significantly worse than when using the orthogonal basis. If we zoom in, it turns out that the PCA in the orthogonal case uses the 10 largest eigenvalues, while the non-orthogonal case only uses the 7 largest. Plotting the eigenvalues in Figure 8.4 shows why. See Appendix A.7 for an explanation why we expect $S_{\mathbf{x}}$ to be rank 10, regardless of the used basis.

We see that for the non-orthogonal basis, a very big jump occurs in the magnitude of the eigenvalues after the 7'th eigenvalue. For the orthogonal basis, this jump occurs after the 10'th eigenvalue. The larger error in the non-orthogonal basis can be explained by the fact that Bayesian inference pushes the solution towards the solution space consisting of these 7 (instead of 10) eigenvectors. We conclude that cutting off the PCA at this 7'th eigenvector results in a too small solution space. Thus we want to increase it in size.

There is no clear point where the eigenvalues should be cut off, if not after the 7'th. After some trial and error, we landed on extending the PCA upto the 110'th eigenvalue and vector. Figure 8.5 shows the NRMSE of the orthogonal and non-orthogonal basis, for using the PCA upto the 10'th and 110'th vector:

A first point to make about Figure 8.5, is that taking more eigenvectors does not improve the NRMSE of the orthogonal basis. This is in accordance with Appendix A.7, as we stated that $S_{\mathbf{x}}$ is rank 10. No extra information can thus be obtained from the other eigenvectors.

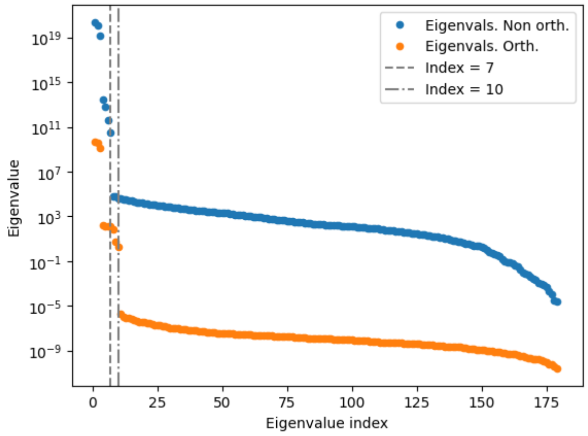

Figure 8.4: The first 180 eigenvalues of the covariance matrices $S_{\mathbf{x}}$ of the orthogonal basis and non-orthogonal basis. Vertical lines are added at the 7'th and 10'th indices.

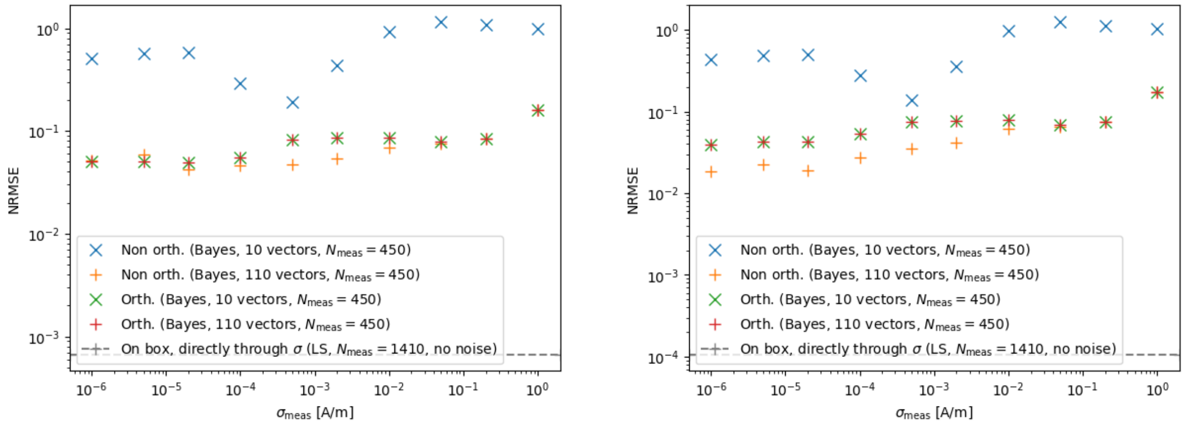

(a) NRMSE on the error plane partially within the BS.

(b) NRMSE on the error plane outside of the BS.

Figure 8.5: The NRMSE of the magnetic field $\mathbf{H} = \mathbf{H}_{\text{ind}} + \mathbf{H}_{\text{ind,perm}}$ according to Equation (5.51), plotted against the varied measurement noise standard deviation σ_{meas}. The CD σ was computed via the non-orthogonal or orthogonal basis vectors σ_{km} using Bayesian inference with PCA and $k_{\text{max}} = 18$. We used either 10 or 110 basis vectors during the PCA of the prior $S_{\mathbf{x}}$. The Bayesian inference prior was built using measurements on the box shaped surface from Section 3.1.2. The $N_{\text{meas}} = 450$ measurements were taken on the seabed of Figure 7.6a. The used magnetic background fields were $\mathbf{B}_0 = (23.360, 0, 41.234)\,\mu\text{T}$ and $\mathbf{B}_{0,\text{perm}} = (0, 23.360, -24.740)\,\mu\text{T}$. The NRMSE was computed on the error planes besides the ship from Figure 7.6b. We also plot the NRMSE of the piecewise constant σ found using the method in Section 5.5.3 with no noise and $N_{\text{meas}} = 1410$ measurements on the box shaped surface from Section 3.1.2.

A second point is that the NRMSE already improves slightly around $\sigma_{\text{meas}} = 10^{-3}$ A/m when 10 vectors are used instead of 7. When we increase to 110 vectors however, the error improves a lot. In a large part of the figures the NRMSE is smaller for the non-orthogonal basis than that of the orthogonal basis. Especially slightly below and around the typical noise level of 10 nT ≈ 0.008 A/m.

However, there are two drawbacks to using the non-orthogonal basis and the previous results. First of all, for small (and large) measurement noises Bayesian inference is quite instable when we use the non-orthogonal basis. The NRMSE varies greatly for each taken sample of measurement locations and noise vectors. Figure 8.6 shows the minimum, maximum and mean NRMSE of the different samples using Bayesian inference with 110 eigenvectors.

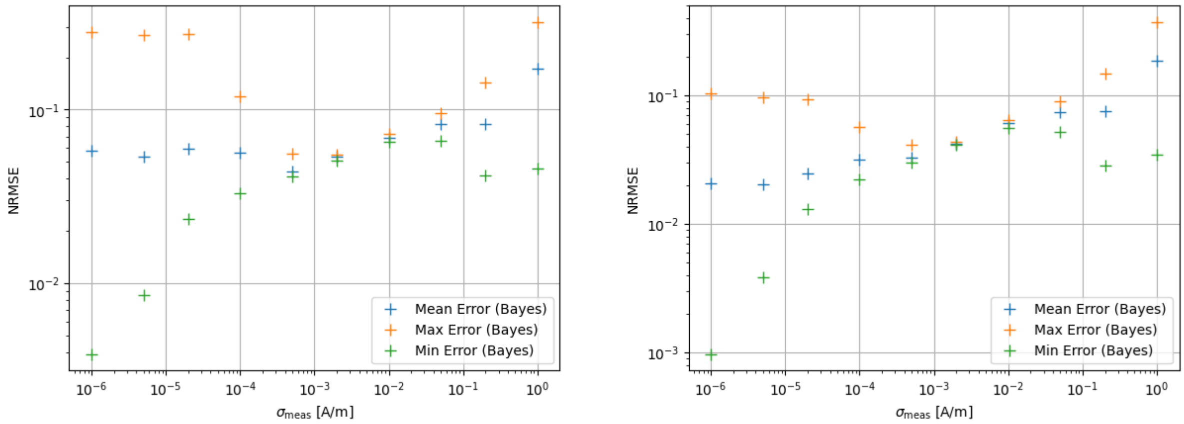

(a) NRMSE on the error plane partially within the BS for the non-orthogonal basis.

(b) NRMSE on the error plane outside of the BS for the non-orthogonal basis.

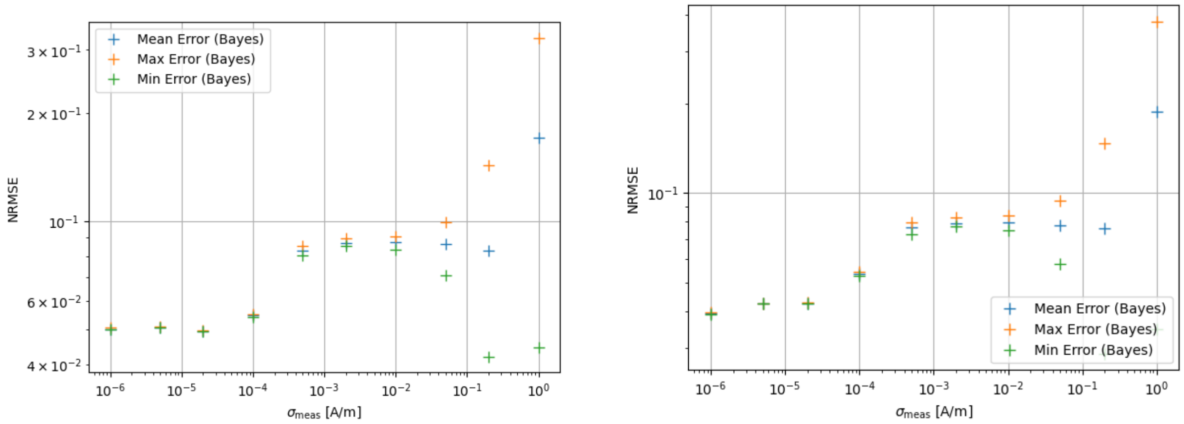

(c) NRMSE on the error plane partially within the BS for the orthogonal basis.

(d) NRMSE on the error plane outside of the BS for the orthogonal basis.

Figure 8.6: The NRMSE of the magnetic field $\mathbf{H} = \mathbf{H}_{\text{ind}} + \mathbf{H}_{\text{ind,perm}}$ according to Equation (5.51), plotted against the varied measurement noise standard deviation σ_{meas}. The CD σ was computed via the non-orthogonal and orthogonal basis vectors σ_{km} using Bayesian inference with PCA and $k_{\max} = 18$. We used the first 110 basis vectors during the PCA of the prior $S_{\mathbf{x}}$. The Bayesian inference prior was built using measurements on the box shaped surface from Section 3.1.2. The $N_{\text{meas}} = 450$ measurements were taken on the seabed of Figure 7.6a and sampled 40 times. The mean, minimum, and maximum NRMSE of the 40 samples are given in the figure. The used magnetic background fields were $\mathbf{B}_0 = (23.360, 0, 41.234)\ \mu\text{T}$ and $\mathbf{B}_{0,\text{perm}} = (0, 23.360, -24.740)\ \mu\text{T}$. The NRMSE was computed on the error planes besides the ship from Figure 7.6b. We also plot the NRMSE of the piecewise constant σ found using the method in Section 5.5.3 with no noise and $N_{\text{meas}} = 1410$ measurements on the box shaped surface from Section 3.1.2.

We see that indeed, the difference between minimum and maximum NRMSE per σ_{meas} is very big for the non-orthogonal basis. It is very small for the orthogonal basis. Investigating why this difference occurs, is outside of the scope of this thesis. We note that around the expected measurement noise of 0.008 A/m, the minimum and maximum do not lay far apart. Therefore we are able to use this data to draw conclusions about the non-orthogonal basis.

A second drawback about the non-orthogonal basis, is that the eigenvalues themselves do not give a clear point at which the cut-off should take place during PCA. This was already clear from Figure 8.4. In Figure 8.7 we plot the NRMSE for different cut-off points.

We see that the errors change a lot, when we go from 10 to 70, or from 90 to 110 eigenvectors. However, the NRMSE stays the same, when we increase the number of eigenvectors from 70 to 90, or from 110 to 130. Determining where to cut the PCA is therefore not straightforward.

As we expect the analytical rank of $S_{\mathbf{x}}$ to be 10 (as derived in Appendix A.7), we suspect that the key eigenvectors are 'hidden' between all others. Especially, since the NRMSE does not always improve when we add eigenvectors, but at some point seems to make a big jump.

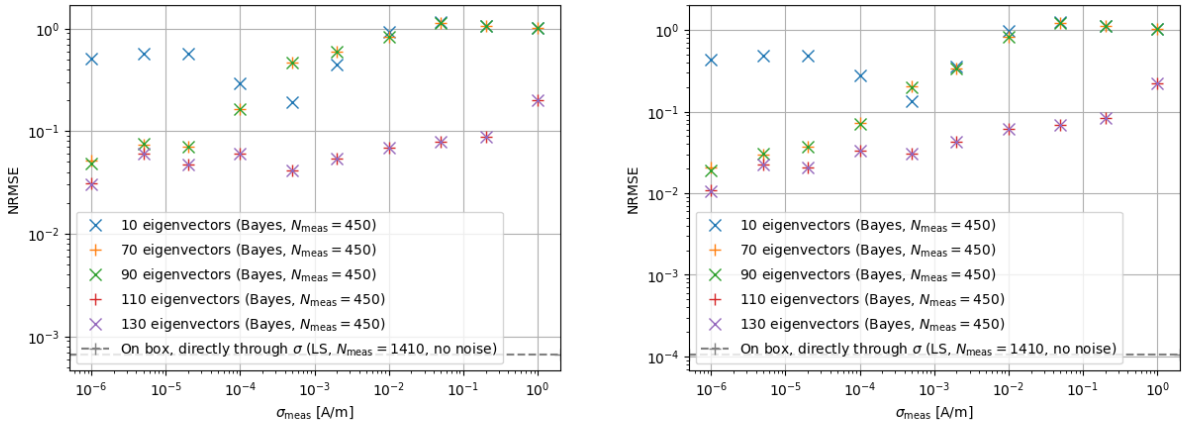

(a) NRMSE on the error plane partially within the BS.

(b) NRMSE on the error plane outside of the BS.

Figure 8.7: The NRMSE of the magnetic field $\mathbf{H} = \mathbf{H}_{\mathrm{ind}} + \mathbf{H}_{\mathrm{ind,perm}}$ according to Equation (5.51), plotted against the varied measurement noise standard deviation σ_{meas}. The CD σ was computed via the non-orthogonal basis vectors σ_{km} using Bayesian inference with PCA and $k_{\mathrm{max}} = 18$. We varied the number of basis vectors that were used during the PCA of the prior $S_{\mathbf{x}}$. The Bayesian inference prior was built using measurements on the box shaped surface from Section 3.1.2. The $N_{\mathrm{meas}} = 450$ measurements were taken on the seabed of Figure 7.6a. The used magnetic background fields were $\mathbf{B}_0 = (23.360, 0, 41.234)\ \mu\mathrm{T}$ and $\mathbf{B}_{0,\mathrm{perm}} = (0, 23.360, -24.740)\ \mu\mathrm{T}$. The NRMSE was computed on the error planes besides the ship from Figure 7.6b. We also plot the NRMSE of the piecewise constant σ found using the method in Section 5.5.3 with no noise and $N_{\mathrm{meas}} = 1410$ measurements on the box shaped surface from Section 3.1.2.

In future research, a more detailed analysis could be performed, which of these eigenvectors are of importance. This might stabilise the use of Bayesian inference with a non-orthogonal basis as well. While we are unable to pinpoint the 10 eigenvectors, a cut-off index should be added to the optimisation scheme, balancing between the model order parameter k_{max} and the residual in the data fit.

Overall Comparison

Overall, using a non-orthogonal basis yields smaller errors, and is easier to work with, than the orthogonal basis. We can skip the orthogonalisation process that is sensitive to numerical errors, and are able to compute the basis up to higher orders k_{max}. When applying Bayesian inference to the non-orthogonal basis, instabilities occur for small σ_{meas}'s. however, for reasonable noise levels, say $\sigma_{\mathrm{meas}} \approx 0.008$ A/m, these issues are not present. In that case the non-orthogonal basis outperforms the orthogonal basis.

9

Conclusions and Recommendations

In this thesis, we have investiged the following research question and sub-questions:

Can we find an alternative magnetic source model of a ship that is defined on the ships outer surface, using a basis that is convenient to map to the DSHE?

1. How well does the method introduced in [6] perform on finding a source model on more complex shapes like the ferry ship Albatros?
2. Does Bayesian inference, as introduced in [7], make the method usable in cases where there are only a few, badly distributed, and/or noisy measurements available?
3. How well does the mapping from the source model expansion to the DSHE outside of the BS perform?
4. Why do we use orthogonal basis functions for the source model on the arbitrary surface, and how does the method perform if we use another non-orthogonal basis?

In this final chapter, we go over the answers, and which parts have been left unanswered or in need of improvement. As the questions are mainly answered in Chapters 6, 7 and 8, we first repeat the conclusions from Chapters 2 up to 5. These chapters mainly contain the theoretical basis and motivation for the new method. After this discussion, we answer each of the sub-questions, by referring to the parts of the thesis that answer these questions. After this we go over some other points of improvement. Finally we give a general answer to the main research question.

Motivation for the multipolar basis on S

Chapter 2 is purely theoretical, and Chapter 3 introduces the benchmark case of the Albatros ferry. In Chapter 4 we find that the DSHE is indeed not a good model for the magnetic field close to the ship, and its coefficients cannot be computed with measurements close to the ship. This chapter yields the motivation of finding a source model that does hold within the BS.

In Chapter 5 such source models are introduced. Both the charge distribution (CD) σ, and the normal dipole distribution (NDD) τ are described. We focus on computations with the CD σ as both the forward and backwards computation of this source is more stable than that of τ. The found σ predicts the magnetic field well, both inside and outside the BS, when we use many measurements that are outside of the arbitrary surface on which σ is defined.

We were unable to derive σ using measurements of the magnetic field on the surface S. Furthermore, the system solved to find σ was heavily overdetermined. This lead to bad results when we used less measurements, and the σ we found often looked non-physical due to very high variance within the solution. The same issues would occur if we added noise to the measurements. Furthermore, since the system is very large, the computational costs of both forward and backward computations are high. Lowering the dimension of the solution space, can resolve these issues, and leads us to the multipolar basis on S.

Sub-Question 1

For the first research question, we investigate how well the method performs using measurements without noise, and without regularisation. We then do introduce some noise, or change the number or locations of measurements. We see what the limitations are when no regularisation is used.

In Section 7.1 we see that the orthogonal multipolar basis works well to describe the equivalent source σ. The NRMSE is below 1% for orders $k_{\max} \geq 12$ and $N_{\text{meas}} = 1410$ measurements that are well distributed around S. The approximation of σ shows converging behaviour for increasing $k_{\max}$, as the NRMSE then decreases (although not monotonously). On the other hand, we did run into the orthogonalisation issues that were described in [6] and [7]. Because of this, we cannot increase the order of approximation $k_{\max}$ to above 18, in order to obtain even smaller errors.

Note, that the magnetised object in this thesis, is the outer shell of the Albatros ship. Therefore, we are modelling a magnetisation on, or close to S, with a CD on S. We expect that the method works well for complex objects with magnetised cores as well, but this has not been verified.

When we decrease the number of measurements to $N_{\text{meas}} = 150$, the system becomes under determined for high $k_{\max}$. We see a slight decrease in the NRMSE for the first few increases in $k_{\max}$, but for $k_{\max} \geq 10$ this decreasing trend stops. This makes senses as we are determining $k_{\max}(k_{\max}+2) > 120$ coefficients with 150 measurements, thus overfitting to the measurement data already starts. Thus, regularisation is needed to obtain good results when we do not have many measurements.

In Section 7.3 we introduce noise. If the noise level is below 0.001 A/m, and N_{meas} above 450, the NRMSE stays below 1% if the measurements are well distributed. That is, if the system is over determined, and the noise levels are not too high, the method described in Section 7.1 works well. Lowering N_{meas} even more, would make the NRMSE too large.

In Section 7.3.1 we investigate the effect of changing the measurement locations. First, we find that our current implementation does not work well for measurements very close to the surface S. This is probably due to the approximation of the integral in Equation (7.2). We recommend to perform a more accurate computation of the integral in future research. Either with a numerical approach, or an analytical based on [8, pp. 243-246].

The section also investigates the effect of taking badly distributed measurements. The benchmark case uses measurements on the seabed. That is, only below the ship. We see that these measurements give a very bad NRMSE.

Sub-Question 2

Both the issues caused by using too little, or badly distributed measurements, can be solved by using Bayesian inference. This method and its results are described in Chapter 8. In Section 8.3 we see the regularisation method works very well for measurements on the seabed. The NRMSE stays below 10% for noise levels higher than expected in reality. It also stays below 10% when we use just 150 measurements on the seabed.

Bayesian inference creates a bias in the found solutions. This is the expected, and wanted behaviour. But it calls for caution. One should be careful that the assumptions made during the build of the prior, are true for the measurements in reality as well. Bayesian inference is also a slightly more complicated regularisation method. One could argue that similar results might be obtained using Tikhonov regularisation. We tried Tikhonov regularisation, but found that choosing the right regularisation parameter is not straightforward. This could be interesting to research in future work.

Sub-Question 3

One of the goals of the multipolar expansion on S, is that it maps easily to the DSHE outside of the BS. In both [6] and [7], it is suggested that the DSHE should only be computed up to the order $k_{\max}$ that was used for the CD expansion using the σ_{km} basis functions. We found however, that in order to describe the $k_{\max}$-'th order approximation of σ using the DSHE, we need a far higher $k_{\max,\text{DSHE}}$. Taking $k_{\max,\text{DSHE}} = k_{\max,\sigma} + 40$ gave us good results. We claimed that the DSHE needing a higher order than the multipolar basis makes sense. It means that the shape of the Albatros holds some information about the magnetisation, and this information is captured within the basis functions on S.

We note that when we compute the contribution of each basis function σ_{km}, to a DSHE coefficient $a_{k'm'}$, an approximation is performed in Equation (7.5). We have not run intro issues of this approximation yet, but expect they might come up for high orders of k'. At this point, the function τ^0_{km} will have high variance across S, and cannot be approximated well by a piecewise constant version. If one wants to use such high orders in future work, we recommend the integral more precisely.

Sub-Question 4

Finally, we investigated the need of the orthogonality for the basis vectors σ_{km}. [6] and [7] both recommend stabilising the orthogonalisation process, to improve the errors of their solutions. In Chapter 5 we noted that many of the properties of the orthogonal basis σ_{km}, also hold for any other basis.

In Section 7.4, we introduce the normalised version of the initial basis σ^0_{km} as such a non-orthogonal basis. Because no orthogonalisation issues occur, we could use the basis up to higher orders. We investigated using it up to order 30 instead of 18, which indeed decreased the errors even more.

From approximately order $k_{\max} = 25$ and up, the NRMSE did not improve. We expect this is due to the discretisation of the basis functions σ_{km} on S. We expect that the error would decrease even more, if we make the mesh smaller, or make the σ_{km} and τ_{km} piecewise linear instead of piecewise constant.

Another thing to note, is that the orthogonalisation issues of the orthogonal basis, occurred around the same order $k_{\max}$, where the non-orthogonal basis its NRMSE increased slightly. We suspect that the orthogonalisation issues were worsened, by "bad quality" initial basis vectors σ^0_{km} around that point, as the NRMSE using the non-orthogonal basis also increased there. What this "bad quality" means, and if this is indeed the case is outside of the scope of this thesis, but could be investigated in future work.

In Section 8.5 we apply Bayesian inference to the non-orthogonal basis up to order $k_{\max} = 18$. During Bayesian inference, a principle component analysis is performed, to invert the singular matrix $S_{\mathbf{x}}$. $S_{\mathbf{x}}$ should have rank 10, and for the orthogonal basis, it is easy to see which 10 eigenvectors and eigenvalues lead to this rank. For the non-orthogonal basis, it is harder to see as after the first 7 eigenvalues, many eigenvalues have approximately the same size. If we include the first 110 vectors (instead of 10), the inversion is still much more stable, than if we were to blindly invert $S_{\mathbf{x}}$.

In Section 8.5 we noted that for the non-orthogonal basis, we still expect $S_{\mathbf{x}}$ to be rank 10. Discrete jumps in the NRMSE, when we increase the number of eigenvectors, suggest that the important eigenvectors are "hidden" between the others. In future research, we recommend doing a more in depth analysis, on which eigenvectors are of importance. Making the computation of $\mathbf{x}_{\mathrm{MAP}}$ more stable.

For very low levels of noise, Bayesian inference can cause instabilities. The inversion of $S_{\mathbf{b}|\mathbf{x}} = \sigma^2_{\mathrm{meas}}\mathrm{Id}$ might cause this, but we have not verified this hypothesis. Investigating why these instabilities are bigger when we use a non-orthogonal basis, vs the orthogonal basis, is outside of the scope of this thesis, but could be done in future work. We suspect they might also be linked to the three important eigenvectors that are "hidden" among the first 110 eigenvectors of $S_{\mathbf{x}}$.

It is important to note that these instabilities become much smaller between noise standard deviations of 0.001 A/m and 0.01 A/m. The NRMSE at these noise levels is around 4 to 7%. These noise levels are levels that can be expected in practice. Furthermore, we find that the NRMSE using this inversion, is significantly better than the one found with the orthogonal basis. We emphasise that for the orthogonal basis, using the first 110 vectors during the inversion of $S_{\mathbf{x}}$, does not improve the NRMSE compared to using just the first 10. This means that the non-orthogonal basis yields better results overall, and Bayesian inference works well to regularise the system consisting of non-orthogonal basis functions.

Overview of Points of Improvement

Throughout answering the sub-questions, we have mentioned many points of improvement. Some other points have also been discussed in the body of this thesis. We now give an overview of the most important points.

1. To make the method usable for measurements closer to the surface S, the approximation done in Equation (7.2) should be performed more precisely. Especially for the elements close to certain measurements. An analytical expression exists for this contribution [8, pp. 243-246], but we have not implemented it. A more precise numerical computation is an option as well.

2. One should always be cautious of the bias introduced by Bayesian inference. The assumptions made during the build of the prior, should also hold during the application of the prior. In settings where this is difficult, one might try to implement Tikhonov regularisation.
3. To decrease the NRMSE of the solution, we recommend looking into the construction of the initial basis functions σ^0_{km} (and τ^0_{km}). They could be defined more precisely, by making the mesh on S, smaller, or by making the functions piecewise linear (or even quadratic) instead of piecewise constant.
4. The covariance matrix $S_{\mathbf{x}}$ is expected to be rank 10, but for the non-orthogonal basis the last three important eigenvectors are ”hidden” between the first 110 eigenvectors. We recommend performing a more in-depth analysis to find which eigenvectors are the once that are of importance. This might also improve the stability of Bayesian inference applied to the non-orthogonal basis for low levels of noise.
5. The simplified geometry representing the Albatros, only consists of the outer shell of the ship. This might make finding an alternative source, on the surface S, easier compared to an object with a magnetised core. We expect the method to work well in such a case as well, but this has not been proved.

Conclusion and Main Research Question

From the sub-questions, we conclude that the method described in this thesis, yields a good and usable alternative magnetic source model. The thesis focussed on using the charge distribution (CD) σ as a source model. Both the orthogonal, and non-orthogonal basis functions can describe this σ well. The found bases deal well with noise, if enough measurements are used that are well distributed. When the number of measurements is decreased, the noise is increased, or the measurements are not well distributed, Bayesian inference can be used to regularise the problem. We found that, besides some stability issues, the non-orthogonal basis outperforms the orthogonal basis, and recommend using it in future work. Finally, we found that mapping the orthogonal basis on S, to the DSHE works well, if we compute the DSHE coefficients up to a higher order (say 40 orders higher) than was used in the expansion on S. We expect the same holds for the non-orthogonal basis.

References

[1] L. M. de Bruin. “Calculating magnetic signatures using the method of moments in Julia”. In: (2024).

[2] D. Calvetti, L. Reichel, and A. Shuibi. “L-curve and curvature bounds for Tikhonov regularization”. In: *Numerical Algorithms* 35.2 (2004), pp. 301–314.

[3] D. Calvetti and E. Somersalo. *An introduction to Bayesian scientific computing: ten lectures on subjective computing*. Vol. 2. Springer Science & Business Media, 2007.

[4] A. Chulliat et al. “The US/UK World Magnetic Model for 2025-2030: Technical Report”. In: (2025).

[5] O. Costin et al. “On the domain of convergence of spherical harmonic expansions”. In: *Communications in Mathematical Physics* 389.2 (2022), pp. 875–897.

[6] G. Derenty-Camenen et al. “Extended spherical harmonic expansion using multipolar bases of equivalent magnetic sources on arbitrary surfaces”. In: *COMPEL-The international journal for computation and mathematics in electrical and electronic engineering* 43.6 (2024), pp. 1239–1258.

[7] G. Derenty-Camenen et al. “Identification of an arbitrary-surface harmonic magnetic model from close measurements”. In: *IEEE Transactions on Magnetics* 61.1 (2024), pp. 1–4.

[8] É. Durand. *Électrostatique (1): Les distributions*. FeniXX, 1964.

[9] L. C. Evans. *Partial differential equations*. Vol. 19. American mathematical society, 2022.

[10] W. C. Gibson. *The method of moments in electromagnetics*. Chapman and Hall/CRC, 2021.

[11] D. Gilbarg et al. *Elliptic partial differential equations of second order*. Vol. 2. 1. Springer, 1998.

[12] G. H. Golub and C. F. Van Loan. *Matrix computations*. JHU press, 2013.

[13] D. J. Griffiths. *Introduction to Electrodynamics*. Vol. 4. Camebridge University Press, 2017.

[14] J. D. Jackson. *Classical Electrodynamics*. 3rd. New York: Wiley, 1998. ISBN: 978-0471309321.

[15] S. J. Julier and J. K. Uhlmann. “New extension of the Kalman filter to nonlinear systems”. In: *Signal processing, sensor fusion, and target recognition VI*. Vol. 3068. Spie. 1997, pp. 182–193.

[16] R. Kress, V. Maz’ya, and V. Kozlov. *Linear integral equations*. Vol. 82. Springer, 1989.

[17] M. Legris. “Identification de l’état magnétique d’un système ferromagnétique à partir de mesures du champ proche”. PhD thesis. Institut National Polytechnique de Grenoble-INPG, 1996.

[18] R. K. Lennartsson et al. “Fused passive acoustic and electric detection of divers”. In: *2010 International WaterSide Security Conference*. IEEE. 2010, pp. 1–8.

[19] A. Morandi, M. Fabbri, and P. L. Ribani. “A modified formulation of the volume integral equations method for 3-D magnetostatics”. In: *IEEE transactions on magnetics* 46.11 (2010), pp. 3848–3859.

[20] J. A. Stratton. *Electromagnetic theory*. John Wiley & Sons, 2007.

[21] A. Tarantola. *Inverse problem theory and methods for model parameter estimation*. SIAM, 2005.

[22] A. Vijn. “Development of a Closed-Loop Degaussing System”. PhD thesis. TU Delft, 2021.

[23] M. Woloszyn and J. Tarnawski. “Magnetic signature reproduction of ferromagnetic ships at arbitrary geographical position, direction and depth using a multi-dipole model”. In: *Scientific Reports* 13.1 (2023), p. 14601.

[24] M. Woloszyn and J. Tarnawski. “Magnetic signature reproduction of ferromagnetic ships at arbitrary geographical position, direction and depth using a multi-dipole model”. In: *Scientific Reports* 13.1 (2023), p. 14601.

A

Deferred Proofs and Derivations

A.1. Proof of Integral over $\frac{1}{\sqrt{x^2+y^2}}$

In this section we proof that equation (5.46) holds.

Proof. We start by splitting the integral into four parts:

$$\int_{[-a,a]^2} \frac{1}{\sqrt{x^2+y^2}} \mathrm{d}x\mathrm{d}y = 4\int_{[0,a]^2} \frac{1}{\sqrt{x^2+y^2}} \mathrm{d}x\mathrm{d}y. \tag{A.1}$$

Which is allowed by symmetry of $\frac{1}{\sqrt{x^2+y^2}}$. Now let $x = au$ and $y = av$, then $\mathrm{d}x\mathrm{d}y = a^2\mathrm{d}u\mathrm{d}v$, $\sqrt{x^2+y^2} = a\sqrt{u^2+v^2}$, and $x = y = a$ yields $u = v = 1$. This yields

$$\begin{aligned}\int_{[0,a]^2} \frac{1}{\sqrt{x^2+y^2}} \mathrm{d}x\mathrm{d}y &= \int_{[0,1]^2} \frac{a^2}{a\sqrt{u^2+v^2}} \mathrm{d}u\mathrm{d}v \\ &= a\int_{[0,1]^2} \frac{1}{\sqrt{u^2+v^2}} \mathrm{d}u\mathrm{d}v.\end{aligned} \tag{A.2}$$

We now solve the inner integral:

$$\begin{aligned}\int_{[0,1]} \frac{1}{\sqrt{u^2+v^2}} \mathrm{d}u &= \left[\ln(u+\sqrt{u^2+v^2})\right]_0^1 \\ &= \ln(1+\sqrt{1+v^2}) - \ln(y) \\ &= \ln\left(\frac{1+\sqrt{1+v^2}}{v}\right),\end{aligned} \tag{A.3}$$

and are left with the known integral:

$$\int_{[0,1]} \ln\left(\frac{1+\sqrt{1+v^2}}{v}\right) \mathrm{d}v = 2\ln(1+\sqrt{2}). \tag{A.4}$$

We end up with

$$\int_{[-a,a]^2} \frac{1}{\sqrt{x^2+y^2}} \mathrm{d}x\mathrm{d}y = 4(2a)\ln(1+\sqrt{2}). \tag{A.5}$$

□

A.2. Proof of Inner Product

In this section, we proof that the inner product, introduced in equation (6.15), is indeed an inner product. The proof follows the structure of [17]. That the inner products in equations (6.16) and (6.24) are inner products, follows from this by symmetry of the inner product.

Proof. We start by showing that the inner product is symmetric.

Recall that we can find τ_i and σ_i using equations (5.16) and (5.17). Now as we have $\sigma(\mathbf{r}) = \partial_{\mathbf{n}}\phi(\mathbf{r}) - \partial_{\mathbf{n}}\phi_{in}^{\sigma}(\mathbf{r})$ and $\tau(\mathbf{r}) = \phi(\mathbf{r}) - \phi_{in}^{\tau}(\mathbf{r})$, we can also let τ_i and σ_i be boundary conditions of some harmonic function u_i, that is defined in the volume V_S. I.e. $\nabla^2 u_i = 0$, with $u_i(\mathbf{r}) = \tau_i(\mathbf{r})$, and $\partial_{\mathbf{n}} u_i(\mathbf{r}) = \sigma_i(\mathbf{r})$ for all $\mathbf{r} \in S$. We can write:

$$\langle\sigma_1|\sigma_2\rangle = \alpha \int_S \tau[\sigma_1](\mathbf{r})\sigma_2(\mathbf{r})dS \tag{A.6}$$

$$= \alpha \int_S u_1(\mathbf{r})\partial_{\mathbf{n}} u_2(\mathbf{r})dS. \tag{A.7}$$

Now by Green's first identity, and the fact that the u_i's are harmonic, we get:

$$\langle\sigma_1|\sigma_2\rangle = \alpha \int_{V_S} \nabla u_1(\mathbf{r}) \cdot \nabla u_2(\mathbf{r}) + u_1(\mathbf{r})\nabla^2 u_2(\mathbf{r})\ dV_S = \alpha \int_{V_S} \nabla u_1(\mathbf{r}) \cdot \nabla u_2(\mathbf{r})\, dV_S. \tag{A.8}$$

Which is symmetric. Next, we prove that the inner product is linear:

$$\langle\sigma_1|\lambda\sigma_2\rangle = \alpha \int_S \tau[\sigma_1](\mathbf{r})\lambda\sigma_2(\mathbf{r})dS = \lambda\alpha \int_S \tau[\sigma_1](\mathbf{r})\sigma_2(\mathbf{r})dS = \lambda\langle\sigma_1|\sigma_2\rangle. \tag{A.9}$$

The final property to prove is positive definiteness. We start by proving the inner product is positive, using equation (A.8):

$$\langle\sigma_1|\sigma_1\rangle = \alpha \int_{V_S} \nabla u_1(\mathbf{r}) \cdot \nabla u_1(\mathbf{r})\, dV_S = \alpha \int_{V_S} ||\nabla u_1(\mathbf{r})||_2^2\, dV_S \geq 0. \tag{A.10}$$

Lastly, we show that $\langle\sigma_1|\sigma_1\rangle = 0$ if and only if $\sigma_1(\mathbf{r}) = 0$ for all $\mathbf{r} \in S$.

$$\begin{aligned} &\langle\sigma_1|\sigma_1\rangle = 0 \\ &\qquad \iff \alpha \int_{V_S} ||\nabla u_1(\mathbf{r})||_2^2\, dV_S = 0. \end{aligned} \tag{A.11}$$

Now since u_1 is a harmonic function, we know ∇u_1 is continuous, and thus we know $\nabla u_1(M) = 0 \quad \forall M \in V_S$. We get:

$$\begin{aligned}
&\langle\sigma_1|\sigma_1\rangle = 0\\
&\qquad\iff \forall\mathbf{r}\in V_S \quad \nabla u_1(\mathbf{r}) = \mathbf{0}\\
&\qquad\iff \exists c\in\mathbb{R} \quad \text{s.t.} \quad \forall\mathbf{r}\in \mathrm{V_S} \quad \mathrm{u_1}(\mathbf{r}) = \mathrm{c}.
\end{aligned} \tag{A.12}$$

Now as we choose $\int_S \tau\, dS = 0 \quad \forall\,\tau$, and $u_1 = \tau_1$, we get $u_1(\mathbf{r}) = c = 0$. ☐

A.3. Proof of Norm of $\nabla(rY_1^{-1})$

In this section we prove that $\nabla(rY_1^{-1})\cdot\nabla(rY_1^{-1})$ = 1.

Proof. We first find a more precise expression for $\nabla(rY_1^{-1})$. We use that $Y_1^{-1}(\theta,\varphi) = -\sin\theta\,\sin\varphi$, based on the definition in equation (4.10).

We start by expanding the gradient in polar coördinates, and applying it to $rY_1^{-1}(\theta,\varphi)$:

$$\begin{aligned}
\nabla(rY_1^{-1}) &= \left(\hat{r}\,\partial_r + \hat{\theta}\frac{1}{r}\partial_\theta + \hat{\varphi}\frac{1}{r\sin\theta}\partial_\varphi\right)\left(rY_1^{-1}(\theta,\varphi)\right)\\
&= -\sin\theta\,\sin\varphi\;\hat{r} - \cos\theta\,\sin\varphi\;\hat{\theta} - \cos\varphi\;\hat{\varphi}.
\end{aligned} \tag{A.13}$$

This result allows us to now determine the square norm of $\nabla(rY_1^{-1})$:

$$\begin{aligned}
\nabla(rY_1^{-1})\cdot\nabla(rY_1^{-1}) &= \sin^2\theta\sin^2\varphi + \cos^2\theta\sin^2\varphi + \cos^2\varphi\\
&= \sin^2\varphi + \cos^2\varphi = 1,
\end{aligned} \tag{A.14}$$

as needed. ☐

A.4. Derivation of PCA for Bayesian Inference

The issue that the Principle Component Analysis (PCA) should solve, is the inversion of $S_\mathbf{x}$ in equation (8.2). The covariance matrix $S_\mathbf{x}\in\mathbb{R}^{n\times n}$ is namely of rank $r \ll n = k_{\max}(k_{\max}+2)$. This section follows the structure of [3, pp. 118-120], and proves that we can find $\mathbf{x}_{\mathrm{MAP}}$ through equations (8.3) and (8.4).

Proof. We write the eigenvalue decomposition for the symmetric covariance matrix $S_\mathbf{x}$:

$$S_\mathbf{x} = V\Lambda V^T, \tag{A.15}$$

where $V = [V_0 V_1]$ and $\Lambda = \begin{bmatrix}\Lambda_0 & 0\\ 0 & 0\end{bmatrix}$, with Λ_0 a diagonal matrix with non-zero eigenvalues corresponding to the eigenvectors in V_0.

Now, as V contains n orthogonal eigenvectors, V spans $\mathbb{R}^n$, so we can write:

$$\mathbf{x} - \overline{\mathbf{x}} = V_0\mathbf{z} + V_1\mathbf{w}, \tag{A.16}$$

with $\mathbf{z}\in\mathbb{R}^r$ and $\mathbf{w}\in\mathbb{R}^{n-r}$. Now since the eigenvectors in V_0 and V_1 are orthogonal, we can multiply equation (A.16) by V_0^T and V_1^T to get:

$$\begin{bmatrix}\mathbf{z}\\ \mathbf{w}\end{bmatrix} = \begin{bmatrix}V_0^T\\ V_1^T\end{bmatrix}(\mathbf{x} - \overline{\mathbf{x}}). \tag{A.17}$$

Now since $\mathbf{x} \sim \mathcal{N}(\overline{\mathbf{x}}, S_{\mathbf{x}})$, we now have

$$\begin{bmatrix} \mathbf{z} \\ \mathbf{w} \end{bmatrix} \sim \mathcal{N}\left(0, \begin{bmatrix} V_0^T S_{\mathbf{x}} V_0 & V_0^T S_{\mathbf{x}} V_1 \\ V_1^T S_{\mathbf{x}} V_0 & V_1^T S_{\mathbf{x}} V_1 \end{bmatrix}\right). \tag{A.18}$$

Filling in $S_{\mathbf{x}} = V \Lambda V^T = [V_0 V_1] \begin{bmatrix} \Lambda_0 & 0 \\ 0 & 0 \end{bmatrix} [V_0 V_1]^T$ yields:

$$\begin{aligned} V_0^T S_{\mathbf{x}} V_0 &= V_0^T [V_0 V_1] \begin{bmatrix} \Lambda_0 & 0 \\ 0 & 0 \end{bmatrix} [V_0 V_1]^T V_0 \\ &= [\mathrm{Id}\ 0] \begin{bmatrix} \Lambda_0 & 0 \\ 0 & 0 \end{bmatrix} [\mathrm{Id}\ 0]^T \\ &= [\mathrm{Id}\ 0] \begin{bmatrix} \Lambda_0 \\ 0 \end{bmatrix} = \Lambda_0, & \text{(A.19)} \\ V_1^T S_{\mathbf{x}} V_0 &= V_1^T [V_0 V_1] \begin{bmatrix} \Lambda_0 & 0 \\ 0 & 0 \end{bmatrix} [V_0 V_1]^T V_0 \\ &= [0\ \mathrm{Id}] \begin{bmatrix} \Lambda_0 \\ 0 \end{bmatrix} = 0, & \text{(A.20)} \\ V_0^T S_{\mathbf{x}} V_1 &= 0, & \text{(A.21)} \\ V_1^T S_{\mathbf{x}} V_1 &= 0. & \text{(A.22)} \\ & & \text{(A.23)} \end{aligned}$$

So equation (A.18) simplifies to

$$\begin{bmatrix} \mathbf{z} \\ \mathbf{w} \end{bmatrix} \sim \mathcal{N}\left(0, \begin{bmatrix} \Lambda_0 & 0 \\ 0 & 0 \end{bmatrix}\right). \tag{A.24}$$

From the above we conclude that $\mathbf{w} = 0$ with probability 1, and $\mathbf{z} \sim \mathcal{N}(0, \Lambda_0)$, with Λ_0 the diagonal matrix containing the non-zero eigenvalues corresponding to the eigenvectors in V_0. Therefore we can rewrite equation (A.16) to:

$$\mathbf{x} = \overline{\mathbf{x}} + V_0 \mathbf{z}. \tag{A.25}$$

Now, we want to determine the MAP estimate of $\mathbf{z}$. The original equation we were solving is $A\mathbf{x} = \mathbf{b}$. We plug equation (A.25) into the original problem to get $AV_0\mathbf{z} = \mathbf{b} - A\overline{\mathbf{x}}$. We now define $A_{\mathbf{z}} = AV_0$ and $\mathbf{b}_{\mathbf{z}} = \mathbf{b} - A\overline{\mathbf{x}}$. Since $A\overline{\mathbf{x}}$ is fixed and equal to the mean $\overline{\mathbf{b}}$, the covariance matrix of $\mathbf{b}_{\mathbf{z}}$ is $S_{\mathbf{b}|\mathbf{z}} = S_{\mathbf{b}|\mathbf{x}}$, and the mean $\overline{\mathbf{b}_{\mathbf{z}}} = 0$. Lastly, as derived in equation (A.24) the covariance matrix of $\mathbf{z}$ is $S_{\mathbf{z}} = \Lambda_0$.

Applying equation (8.2) to the problem $A_{\mathbf{z}}\mathbf{z} = \mathbf{b}_{\mathbf{z}}$ using the above means and covariance matrices, we get:

$$\begin{aligned} \mathbf{z}_{\mathrm{MAP}} &= \arg\min_{\mathbf{z}} (A_{\mathbf{z}}\mathbf{z} - \mathbf{b}_{\mathbf{z}})^T S_{\mathbf{b}|\mathbf{z}}^{-1} (A_{\mathbf{z}}\mathbf{z} - \mathbf{b}_{\mathbf{z}}) + \mathbf{z}^T \Lambda_0^{-1} \mathbf{z} \\ &= (A_{\mathbf{z}}^T S_{\mathbf{b}|\mathbf{x}}^{-1} A_{\mathbf{z}} + \Lambda_0^{-1})^{-1} (A_{\mathbf{z}}^T S_{\mathbf{b}|\mathbf{x}}^{-1} \mathbf{b}_{\mathbf{z}}). & \text{(A.26)} \end{aligned}$$

Lastly, by equation (A.25) we get

$$\mathbf{x}_{\mathrm{MAP}} = \overline{\mathbf{x}} + V_0 \mathbf{z}_{\mathrm{MAP}}. \tag{A.27}$$

□

A.5. Proof of Equivalence of MAP and Least Squares Estimate when Λ_0 is Large

In this section, we proof that the MAP and least squares estimate of $\mathbf{z}$ in the system $A_{\mathbf{z}}\mathbf{z} = \mathbf{b}_{\mathbf{z}}$, are equal when the entries of the diagonal covariance matrix of $\mathbf{z}$ Λ_0 go to infinity.

Proof. We start by repeating equation (8.4), which defines the MAP estimate $\mathbf{z}_{\mathrm{MAP}}$:

$$\mathbf{z}_{\mathrm{MAP}} = \arg\min_{\mathbf{z}} (A_{\mathbf{z}}\mathbf{z} - \mathbf{b}_{\mathbf{z}})^T S_{\mathbf{b}|\mathbf{z}}^{-1} (A_{\mathbf{z}}\mathbf{z} - \mathbf{b}_{\mathbf{z}}) + \mathbf{z}^T \Lambda_0^{-1} \mathbf{z}. \tag{A.28}$$

Recall that the least squares estimate of $\mathbf{z}$ is defined by:

$$\mathbf{z}_{\mathrm{LS}} = \arg\min_{\mathbf{z}} (A_{\mathbf{z}}\mathbf{z} - \mathbf{b}_{\mathbf{z}})^T (A_{\mathbf{z}}\mathbf{z} - \mathbf{b}_{\mathbf{z}}). \tag{A.29}$$

Now, as the entries of Λ_0 go to infinity, we have $\Lambda_0^{-1} \to 0$. Therefore the second term in equation (**??**) goes to zero as well.

Now recall that $S_{\mathbf{b}|\mathbf{z}} = S_{\mathbf{b}|\mathbf{x}} = \sigma_{\mathbf{b}}^2 \,\mathrm{Id}$. Therefore we have:

$$\begin{aligned} \mathbf{z}_{\mathrm{MAP}} &= \arg\min_{\mathbf{z}} (A_{\mathbf{z}}\mathbf{z} - \mathbf{b}_{\mathbf{z}})^T \frac{1}{\sigma_{\mathbf{b}}^2} \,\mathrm{Id} (A_{\mathbf{z}}\mathbf{z} - \mathbf{b}_{\mathbf{z}}) \\ &= \arg\min_{\mathbf{z}} (A_{\mathbf{z}}\mathbf{z} - \mathbf{b}_{\mathbf{z}})^T (A_{\mathbf{z}}\mathbf{z} - \mathbf{b}_{\mathbf{z}}) = \mathbf{z}_{\mathrm{LS}}, \end{aligned} \tag{A.30}$$

as needed. ☐

A.6. Proof of Equivalence of MAP and Least Squares Estimate when $\sigma_{\mathbf{b}} \to 0$

In this section, we proof that the MAP and least squares estimate of $\mathbf{x}$ in the system $A\mathbf{x} = \mathbf{b}$, are equal when the standard deviation of the measurement noise $\sigma_{\mathbf{b}}$ goes to zero.

Proof. We start by repeating equation (8.2), which defines the MAP estimate $\mathbf{x}_{\mathrm{MAP}}$:

$$\mathbf{x}_{\mathrm{MAP}} = \arg\min_{\mathbf{x}} (A\mathbf{x} - \mathbf{b})^T S_{\mathbf{b}|\mathbf{x}}^{-1} (A\mathbf{x} - \mathbf{b}) + (\mathbf{x} - \overline{\mathbf{x}})^T S_{\mathbf{x}}^{-1} (\mathbf{x} - \overline{\mathbf{x}}). \tag{A.31}$$

Now, as $S_{\mathbf{b}|\mathbf{x}} = \sigma_{\mathbf{b}}^2 \,\mathrm{Id}$, we can write:

$$\begin{aligned} \mathbf{x}_{\mathrm{MAP}} &= \arg\min_{\mathbf{x}} (A\mathbf{x} - \mathbf{b})^T \frac{1}{\sigma_{\mathbf{b}}^2} (A\mathbf{x} - \mathbf{b}) + (\mathbf{x} - \overline{\mathbf{x}})^T S_{\mathbf{x}}^{-1} (\mathbf{x} - \overline{\mathbf{x}}) \\ &= \arg\min_{\mathbf{x}} (A\mathbf{x} - \mathbf{b})^T (A\mathbf{x} - \mathbf{b}) + \sigma_{\mathbf{b}}^2 (\mathbf{x} - \overline{\mathbf{x}})^T S_{\mathbf{x}}^{-1} (\mathbf{x} - \overline{\mathbf{x}}). \end{aligned} \tag{A.32}$$

Where we multiplied the equation by $\sigma_{\mathbf{b}}^2$. If we now let $\sigma_{\mathbf{b}} \to 0$, we get

$$\mathbf{x}_{\mathrm{MAP}} = \arg\min_{\mathbf{x}} (A\mathbf{x} - \mathbf{b})^T (A\mathbf{x} - \mathbf{b}) = \mathbf{x}_{\mathrm{LS}} \tag{A.33}$$

as needed.

☐

A.7. Rank $S_{\mathbf{x}}$

In this section, we explain why we expect the rank of $S_{\mathbf{x}}$ to equal 10, when we vary $\mathbf{B}_0$, $\mathbf{B}_{0,\mathrm{perm}}$, $\mu_{r,\mathrm{ind}}$ and $\mu_{r,\mathrm{perm}}$. To do this, we go over the different combinations of μ_r's, and deduct how many dimensions each permeability adds to $S_{\mathbf{x}}$. We take this approach, since the total magnetic field $\mathbf{B}$, and thus the c_{km} coefficients are not linearly dependent on the μ_r's, (while they are on the background fields $\mathbf{B}_0$ and $\mathbf{B}_{0,\mathrm{perm}}$).

The first μ_r combination, we take the mean values of both $\mu_{r,\mathrm{ind}}$, and $\mu_{r,\mathrm{perm}}$. As we keep these two variables at their mean, in the unscented transform we do vary all 6 other variables. As the total magnetic field is linearly dependent on all components of the magnetic background fields, it does not matter that we take 2 extra samples per component. Each component adds one dimension to the samples. So in the first μ_r combination, we obtain 6 dimensions within the samples.

Now, we take the mean value for $\mu_{r,\mathrm{ind}}$, and $\mu_{r,\mathrm{perm}} = \overline{\mu_{r,\mathrm{perm}}} + \sqrt{N+\kappa}\,\sigma_{\mu_{r,\mathrm{perm}}}$ for the magnetic permeability modelling the permanent part. As we already took a non-mean value for one of the variables, all other variables are kept at their mean. Therefore, this combination of μ_r's only adds 1 dimension to the samples.

As the magnetic field, and the c_{km} are not linearly dependent on the μ_r's, we can follow the same argument for $\mu_{r,\mathrm{perm}} = \overline{\mu_{r,\mathrm{perm}}} - \sqrt{N+\kappa}\,\sigma_{\mu_{r,\mathrm{perm}}}$. We add another dimension to the samples.

Finally, we can do the same for $\mu_{r,\mathrm{ind}}$, keeping $\mu_{r,\mathrm{perm}}$ on the mean value. This adds two dimensions to the samples.

In total, the samples span a 10-dimensional space. Making $S_{\mathbf{x}}$ rank 10. This holds for any basis, so also for the non-orthogonal basis.

B

Extra Figures and Theory

B.1. Extreme Example of Overfitting of Bayesian Inference

The extreme example given in this section, shows what happens if you ignore the assumptions made when building the prior used in Bayesian inference. In this example, the prior is built by only varying the background magnetic field $\mathbf{B}_0$ (so there is not permanent magnetisation, and the magnetic permeability is also kept constant). We then remove the magnetised object, leading to a zero induced magnetic field, and a constant measurement vector $\mathbf{b}$. In Figure B.1 we see that eventhough the measurement vector is constant, and the induced magnetic field is zero, the approximation of the magnetic field still looks exactly as the one from the benchmark case in Chapter 3.

By varying $\mathbf{H}_{0,\text{perm}}$ and the magnetic permeabilities $\mu_{r,\text{ind}}$ and $\mu_{r,\text{perm}}$, this overfitting can be resolved a bit. However, one should still be cautious of following the assumptions used when building the prior.

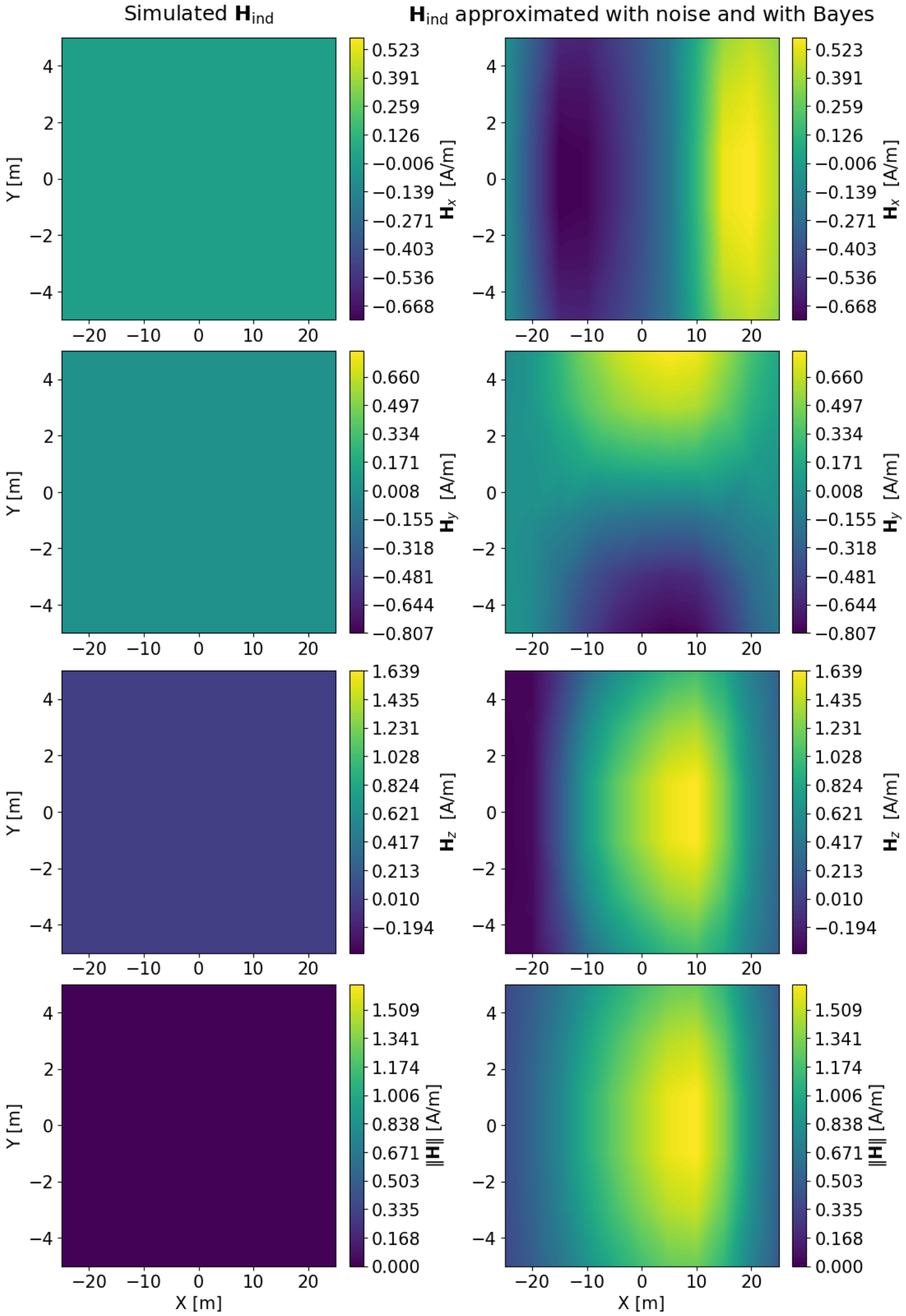

Figure B.1: Induced magnetic field $\mathbf{H}_{\text{ind}}$ computed with Bayesian Inference, where the prior was built by only varying the background field $\mathbf{H}_0$. The measurement vector was a constant vector, that was exactly the background field $\mathbf{H}_0 = (18.589, 0, 32.813)$ A/m. The left column shows the exact induced magnetic field, which is zero, as there is no magnetised object. The magnetic field is evaluated on the error surface partially within the BS, as depicted in Figure 3.2.

B.2. Tikhonov Regularisation

Depending on the number and location of measurement points within the vector $\mathbf{b}$, the level of noise in those measurements, and $k_{\max}$, the system $A\mathbf{x} = \mathbf{b}$ can be unstable or singular. Therefore, inverting A is not straightforward. In this thesis we mainly look at two ways of solving $A\mathbf{x} = \mathbf{b}$: Finding the least squares solution and applying Bayesian Inference. A simpler regularisation method, that is not applied thoroughly, is Tikhonov regularisation. We have applied the method using a plug-in parameter, but this did not yield good results. The method and results are given in this section.

Tikhonov Regularization

Typically, when solving a matrix-vector equation, we want a least squares solution. That is,

$$\mathbf{x}_{LS} = \arg\min_{\mathbf{x}} ||A\mathbf{x} - \mathbf{b}||_2^2. \tag{B.1}$$

The issue with under-determined systems is however, that this yields infinitely many solutions. Furthermore, it is highly unstable if $\mathbf{b}$ contains measurement noise.

Tikhonov Regularization solves this issue for many cases, by adding a penalty on the size of the vector $\mathbf{x}$. This is done as follows:

$$\mathbf{x}_\lambda = \arg\min_{\mathbf{x}} ||A\mathbf{x} - \mathbf{b}||_2^2 + \lambda^2||\mathbf{x}||_2^2. \tag{B.2}$$

This equation can be solved to find

$$\mathbf{x}_\lambda = (A^{\mathrm{T}}A + \lambda^2 I)^{-1}A^{\mathrm{T}}\mathbf{b}. \tag{B.3}$$

Choosing the right λ can be done in multiple ways. A popular method is by finding the corner of the so-called ”L-curve”, however it is computationally expensive [2]. As the optimal λ may vary for every new instance of the system $A\mathbf{x} = \mathbf{b}$, a method that is less computationally heavy is preferred. We tried the following plug-in parameter.

Plug-in regularisation parameter

Recall that we solve the equation $A\mathbf{x} = \mathbf{b}$, with A an $n \times p$ matrix. We now define the matrix $\Omega = (A^T A/n)^+$, where $^+$ is the symbol for the Moore-Penrose inverse. We estimate the vector $\mathbf{x}$ with $\hat{\mathbf{x}} = A^+\mathbf{b}$, and if we don’t know the measurement noise, we estimate its variance σ^2_{meas} by $\hat{\sigma}^2_{\mathrm{meas}} = \frac{||\mathbf{b}-A\mathbf{x}||_2^2}{n-p}$. The plug-in parameter is

$$\lambda^\star = \frac{\hat{\sigma}^2_{\mathrm{meas}}\mathrm{tr}(\Omega)}{\hat{\mathbf{x}}^T\Omega\hat{\mathbf{x}} + 3\hat{\sigma}^2_{\mathrm{meas}}\mathrm{tr}(\Omega^2)/n}. \tag{B.4}$$

Results

We now visualise the error for increasing noise σ_{meas}, and compare it to the error using the least squares solver, and Bayesian inference as regularisation. The magnetic field is taken the same as in Chapter 8.

The measurements of vector $\mathbf{b}$ are taken on the seabed surface of Chapter 3. The error planes are the ones of Figure 7.6b.

We now assume σ_{meas} is known, and use equation (B.4) to choose the parameter in Tikhonov. We get the following figures for the NRMSE:

In Figure B.2 we see that Tikhonov regularisation significantly improves the found solution, compared to the solution found with a least squares solver. However, for larger noise levels, it performs worse than Bayesian Inference. Recall from Section 7.3, that a reasonable magnetometers have a precision of 0.008 A/m. At this point, Bayesian inference significantly outperforms the Tikhonov solution.

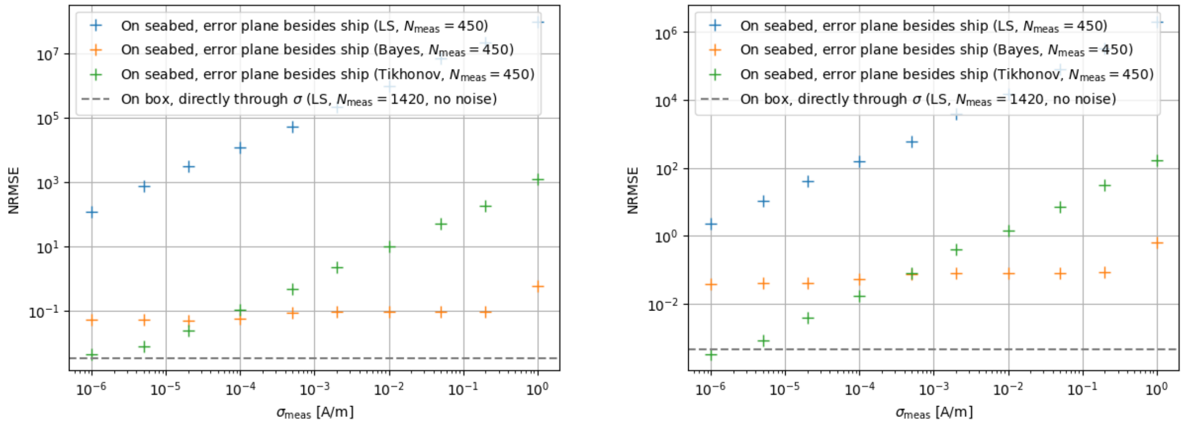

(a) NRMSE on the error plane partially within the BS.

(b) NRMSE on the error plane outside of the BS.

Figure B.2: The NRMSE of the magnetic field $\mathbf{H}$ according to equation (5.51). The CD σ was computed via the basis vectors σ_{km} from Chapter 6, or directly through the method from Section 5.5.3. During the computation of through the σ_{km}, we varied the measurement noise σ_{meas}. The measurements were taken on the seabed of Figure 7.6a. The NRMSE was computed on the error planes besides the ship from Figure 7.6b. The coefficients c_{km} were found using a least squares solver, Bayesian inference or Tikhonov regularisation. The Bayesian inference prior was built using measurements on the box shaped surface from Section 3.1.2. The Tikhonov parameter λ was found using equation (B.4).

That Bayesian inference performs better, can be explained by the fact that its bias is based on physics. Meanwhile, the bias introduced by Tikhonov regularisation, is purely based on the size of the coefficients. In future research, one could try varying the method of finding λ to see if the error gets improved.

C

Code

C.1. Build Initial Basis

```python
class HarmonicBasis:
    """
    Compute harmonic basis functions for equivalent sources on arbitrary surface S.
    """

    def __init__(self, surface, n_subdivisions=20):
        """
        Parameters
        ----------
        surface : SteppedSurface
            The surface object on which to compute the basis functions
        """
        self.surface = surface
        self.mu_0 = 4 * np.pi * 1e-7  # Permeability of free space
        self.points, self.normals, self.weights = self.surface.get_surface_mesh(
            n_subdivisions)
        self.alpha = self.surface.compute_volume()
        self.sigma_km_0 = None
        self.tau_km_0 = None
        self.r_BS = np.max(np.linalg.norm(self.points, axis=1))

    def compute_sigma_km_0(self, k, m):
        """
        Compute  _km basis function on surface points.
        _km = \partial_n (r^k * Y_k^m)

        Parameters
        ----------
        k : int
            Degree of spherical harmonic
        m : int
            Order of spherical harmonic (-k <= m <= k)
        points : ndarray, shape (N, 3)
            Surface points in Cartesian coordinates

        Returns
        -------
        sigma_km : ndarray, shape (N, 3)
            Vector field  _km at each point
        """
        N = len(self.points)
        sigma_km_0 = np.zeros(N)

        for i, point in enumerate(self.points):
            # Convert to spherical coordinates
            x, y, z = point
            r = np.sqrt(x**2 + y**2 + z**2)
```

```
            theta = np.arccos(z / r)
            phi = np.arctan2(y, x)

            # Compute gradient of r^k * Y_k^m
            grad = functions.grad_Y_km(k, m, r, theta, phi)

            sigma_km_0[i] = np.dot(grad, self.normals[i])

        return sigma_km_0

    def compute_tau_km_0(self, k, m):
        """
        Compute  _km basis function on surface points.
        _km = r^k * Y_k^m

        Parameters
        ----------
        k : int
            Degree of spherical harmonic
        m : int
            Order of spherical harmonic (-k <= m <= k)
        points : ndarray, shape (N, 3)
            Surface points in Cartesian coordinates

        Returns
        -------
        tau_km : ndarray, shape (N, 3)
            Vector field  _km at each point
        """
        N = len(self.points)
        tau_km_0 = np.zeros(N)

        for i, point in enumerate(self.points):
            # Convert to spherical coordinates
            x, y, z = point
            r = np.sqrt(x**2 + y**2 + z**2)
            theta = np.arccos(z / r) if r > 0 else 0
            phi = np.arctan2(y, x)

            # Compute r^k * Y_k^m
            tau_km_0[i] = r**k * functions.Y_km(k, m, theta, phi)

        return tau_km_0

    def _compute_all_sigma_tau_0(self, k_max):
        km = k_max*(k_max+2)
        N = len(self.points)

        sigma_km_0 = np.zeros([km,N])
        tau_km_0 = np.zeros([km,N])

        for i, (k, m) in enumerate(self.sigma_indices):
            if i%10==0:
                print('j␣0th␣=␣', i+1, '/', k_max*(k_max+2))
            sigma_km_0[i] = self.compute_sigma_km_0(k, m)
            tau_km_0[i] = self.compute_tau_km_0(k, m)

        self.sigma_km_0 = sigma_km_0
        self.tau_km_0 = tau_km_0
```

C.2. Build Orthogonal Basis

```
class HarmonicBasis:
    def compute_all_sigma_tau(self, k_max, reorth=0, raise_error = True):
        """
        Compute sigma_km^0, and the orthonormalized sigma_km with or without reorthonormalization. Also computes this for tau_km.

        Parameters
        ----------
```

```
        k_max : Maximum order of expansion

        reorth : if True, reorthonormalization is applied.
        """

        km = k_max*(k_max+2)
        N = len(self.points)

        self.sigma_indices = [(k, m) for k in range(1, k_max + 1) for m in range(-k, k + 1)]

        if self.sigma_km_0 is None or self.tau_km_0 is None:
            self._compute_all_sigma_tau_0(k_max)
        print('Re-orthonormalization')

        if np.shape(self.sigma_km_0)[0] > km or np.shape(self.tau_km_0)[0] > km:
            sigma_km_0 = self.sigma_km_0[:km].copy()
            tau_km_0 = self.tau_km_0[:km].copy()
        else:
            sigma_km_0 = self.sigma_km_0.copy()
            tau_km_0 = self.tau_km_0.copy()

        for r in range(0,reorth + 1):
            print('Reorth␣nr', r)
            sigma_km = sigma_km_0
            tau_km = tau_km_0

            for i, (k, m) in enumerate(self.sigma_indices):

                norm_sq = (self.inner_product(sigma_km[i], tau_km[i]))
                if norm_sq < 0 and raise_error == True:
                    print(i, norm_sq, norm_sq**0.5)
                    print(sigma_km[i])
                    print(sigma_km_0[i])
                    raise ValueError("Negative␣norm␣encountered␣during␣orthonormalization.")
                norm = norm_sq**0.5
                if norm > 1e-6:
                    sigma_km[i] = sigma_km[i]/norm
                    tau_km[i] = tau_km[i]/norm
                elif raise_error == True:
                    raise ValueError("Zero␣norm␣encountered␣during␣orthonormalization.")

                for j in range(i+1,km):

                    # Compute inner product
                    inner_prod = self.inner_product(sigma_km[i], tau_km[j])

                    sigma_km[j] = sigma_km[j] - inner_prod * sigma_km[i]
                    tau_km[j] = tau_km[j] - inner_prod * tau_km[i]

                    norm_sq = self.inner_product(sigma_km[j], tau_km[j])

                    if norm_sq<0 and raise_error == True:
                        print(i, j, norm_sq, norm_sq**0.5)
                        print(sigma_km[j])
                        print(tau_km[j])
                        raise ValueError("Negative␣norm␣encountered␣during␣orthonormalization.")

            sigma_km_0 = sigma_km
            tau_km_0 = tau_km


        self.sigma_km = sigma_km
        self.tau_km = tau_km
        return sigma_km, tau_km
```

C.3. Build Non-Orthogonal Basis

```
class NonOrthogonalBasis(HarmonicBasis):
    def compute_all_sigma_tau(self, k_max, reorth=0, raise_error = True):
```

```
        """
        Compute sigma_km^0, and the normalised sigma_km. Also computes this for tau_km.

        Parameters
        ----------
        k_max : Maximum order of expansion

        reorth : if True, reorthonormalization is applied.
        """

        km = k_max*(k_max+2)
        N = len(self.points)

        self.sigma_indices = [(k, m) for k in range(1, k_max + 1) for m in range(-k, k + 1)]

        if self.sigma_km_0 is None or self.tau_km_0 is None:
            self._compute_all_sigma_tau_0(k_max)

        if np.shape(self.sigma_km_0)[0] > km or np.shape(self.tau_km_0)[0] > km:
            sigma_km_0 = self.sigma_km_0[:km].copy()
            tau_km_0 = self.tau_km_0[:km].copy()
        else:
            sigma_km_0 = self.sigma_km_0.copy()
            tau_km_0 = self.tau_km_0.copy()

        self.sigma_km = np.zeros_like(sigma_km_0)
        self.tau_km = np.zeros_like(tau_km_0)

        for j in range(km):
            integrand = sigma_km_0[j] * tau_km_0[j]
            norm = (np.sum(integrand * self.weights)*self.alpha)**0.5
            self.sigma_km[j] = sigma_km_0[j] / norm
            self.tau_km[j] = tau_km_0[j] / norm

        return self.sigma_km, self.tau_km

    def compute_projected_field_coeffs(self, c_km, k_max_prime):
        """
        Project the reconstructed field (from c_km) onto  ^0_{k'm'} basis to get a_{k'm'}.

        Parameters
        ----------
        c_km : ndarray
            Source coefficients from inverse problem
        sigma_indices : list of (k, m)
            Indices associated with c_km
        k_max_prime : int
            Max degree of output projection.

        Returns
        -------
        a_kpmp : ndarray
            Projected coefficients a_{k'm'}
        projected_indices : list of (k', m')
            Index list for a_kpmp
        """

        a_kpmp = []
        sigma_p_indices = [(k, m) for k in range(1, k_max_prime + 1) for m in range(-k, k +
            1)]

        for i, (k_p, m_p) in enumerate(sigma_p_indices):#range(1, k_max_prime + 1):
            sigma_kpmp_0 = self.sigma_km_0[i]
            tau_kpmp_0 = self.tau_km_0[i]

            acc = 0
            for j, (k, m) in enumerate(sigma_p_indices):
                integrand = sigma_kpmp_0 * self.tau_km[j]
                acc += c_km[j] * np.sum(integrand*self.weights) * self.alpha

            a_kpmp.append(acc / self.alpha)
```

```

        return np.array(a_kpmp), sigma_p_indices
```

C.4. Build Matrix to Compute c_{km}

```
class HarmonicBasis:
    def compute_A_matrix(self, sensor_points_measure, sensor_axes, k_max):
        """
        Construct the forward model matrix A that maps source coefficients c_km
        to sensor measurements of the field.

        Each column of A corresponds to the field contribution of a single basis
        function  _{k,m}, computed at all sensor locations via numerical integration.
        Each row corresponds to either a projected measurement along the sensor axis
        or (optionally) individual Cartesian components of the field.

        Parameters
        ----------
        sensor_points_measure : ndarray, shape (M, 3)
            Sensor locations P_i where the field is evaluated.
        sensor_axes : ndarray, shape (M, 3)
            Unit vectors e_i defining the measurement direction of each sensor
            (used if projecting the field onto sensor axes).
        k_max : int
            Maximum degree k of the basis functions  _{k,m}.

        Returns
        -------
        A : ndarray, shape (M, N) or (3M, N)
            Forward model matrix mapping coefficients c_km to measured data.
            If projecting onto sensor axes, shape is (M, N).
            If storing full vector field components, shape is (3M, N).
        sigma_indices : list of (k, m)
            List of (k, m) index pairs corresponding to each column of A.
        """
        # Generate all (k, m) up to k_max
        sigma_indices = [(k, m) for k in range(1, k_max + 1) for m in range(-k, k + 1)]
        N_sensors = sensor_points_measure.shape[0]
        N_basis = len(sigma_indices)
        N_points = self.points.shape[0]

        A = np.zeros((N_sensors*3, N_basis))

        for j, (k, m) in enumerate(sigma_indices):
            sigma_vals = self.sigma_km[j]

            for i, (P_i, e_i) in enumerate(zip(sensor_points_measure, sensor_axes)):
                R = P_i - self.points
                R_norm = np.linalg.norm(R, axis=1)
                if np.min(R_norm**3) < 1e-6:
                    print('Measurement␣surface␣is␣very␣close␣to␣sensor')
                    print(np.min(R_norm))

                kernel = - R / R_norm[:,np.newaxis]**3
                integrand = -(sigma_vals[:,np.newaxis] / (4 * np.pi)) * kernel
                field_i = np.sum(integrand * self.weights[:,np.newaxis], axis=0)

                if b_long:
                    A[i,j] = field_i[0]
                    A[i+N_sensors,j] = field_i[1]
                    A[i+2*N_sensors,j] = field_i[2]
                else:
                    A[i, j] = np.dot(field_i, e_i)
        return A, sigma_indices
```

C.5. Map From c_{km} to a_{km} of DSHE

Both of the following functions, could be replaced by building a matrix before hand, and only performing a matrix vector equation when you want to map the c_{km} to the a_{km}. The matrix entries are given in equation (7.5). As we did not perform this mapping often in this thesis, we did not optimise this computation in python.

```python
class HarmonicBasis:
    def compute_projected_field_coeffs(self, c_km, k_max_prime, sigma_ip = False, k_max_a_km=None):
        """
        Project a reconstructed field onto the ^O_{k'm'} basis to obtain coefficients a_{k'm'}.

        This function takes coefficients c_km (representing a reconstructed field in one basis)
        and projects the corresponding field onto a new set of basis functions ^O_{k'm'}.
        The projection is computed via numerical integration using precomputed weights.

        Parameters
        ----------
        c_km : ndarray
            Coefficient vector representing the reconstructed field in the original basis.
        k_max_prime : int
            Maximum degree k' for the target projection basis ^O_{k'm'}.

        Returns
        -------
        a_kpmp : ndarray
            Coefficients of the field projected onto the ^O_{k'm'} basis.
        projected_indices : list of (k', m')
            List of index pairs corresponding to each entry in a_kpmp.
        """
        if k_max_a_km is None:
            k_max_a_km = k_max_prime

        a_kpmp = np.zeros(k_max_a_km*(k_max_a_km+2))
        sigma_p_indices_a_km = [(k, m) for k in range(1, k_max_a_km + 1) for m in range(-k, k + 1)]

        for i in range(k_max_a_km*(k_max_a_km+2)):
            for j in range(k_max_prime*(k_max_prime+2)):
                if sigma_ip:
                    a_kpmp[i] += c_km[j] * self.inner_product(self.tau_km[j], self.sigma_km_0[i])
                else:
                    a_kpmp[i] += c_km[j] * self.inner_product(self.sigma_km[j], self.tau_km_0[i])

        a_kpmp = a_kpmp / self.alpha
        return a_kpmp, sigma_p_indices_a_km
```

```python
class NonOrthogonalBasis(HarmonicBasis):

    def compute_projected_field_coeffs(self, c_km, k_max_prime):
        """
        Project a reconstructed field onto the ^O_{k'm'} basis to obtain coefficients a_{k'm'}.

        This function takes coefficients c_km (representing a reconstructed field in one basis)
        and projects the corresponding field onto a new set of basis functions ^O_{k'm'}.
        The projection is computed via numerical integration using precomputed weights.

        Parameters
        ----------
        c_km : ndarray
            Coefficient vector representing the reconstructed field in the original basis.
        k_max_prime : int
            Maximum degree k' for the target projection basis ^O_{k'm'}.

        Returns
        -------
        a_kpmp : ndarray
            Coefficients of the field projected onto the ^O_{k'm'} basis.
```

```
        projected_indices : list of (k', m')
            List of index pairs corresponding to each entry in a_kpmp.
        """

        a_kpmp = []
        sigma_p_indices = [(k, m) for k in range(1, k_max_prime + 1) for m in range(-k, k + 1)]

        for i, (k_p, m_p) in enumerate(sigma_p_indices):
            sigma_kpmp_0 = self.sigma_km_0[i]
            tau_kpmp_0 = self.tau_km_0[i]

            acc = 0
            for j, (k, m) in enumerate(sigma_p_indices):
                integrand = sigma_kpmp_0 * self.tau_km[j]
                acc += c_km[j] * np.sum(integrand*self.weights) * self.alpha

            a_kpmp.append(acc / self.alpha)

        return np.array(a_kpmp), sigma_p_indices
```

C.6. Building Prior $S_{\mathbf{x}}$ and $\overline{\mathbf{x}}$

In this section we include the code to build the prior, when we vary $\mathbf{B}_0$, $\mu_{r,\text{ind}}$, $\mathbf{B}_{0,\text{perm}}$ and $\mu_{r,\text{perm}}$. Some parts of the code have been left out, to avoid needing to introduce simple functions and variables. These parts are described in the regular text parts

We start by defining the means and standard deviations. Recall that we used the values in Table 8.1.

```
n_unknown = 8
kappa = 3-n_unknown
covvar_X = np.zeros((n_unknown, n_unknown))
covvar_X[0, 0] = std_dev_B0**2
covvar_X[1, 1] = std_dev_B0**2
covvar_X[2, 2] = std_dev_B0**2
covvar_X[3, 3] = std_dev_muind**2
covvar_X[4, 4] = std_dev_Bperm**2
covvar_X[5, 5] = std_dev_Bperm**2
covvar_X[6, 6] = std_dev_Bperm**2
covvar_X[7, 7] = std_dev_muperm**2
mean_X = np.array([mean_B0_x_z,mean_B0_y,mean_B0_x_z,mean_muind,mean_Bperm_x_y,mean_Bperm_x_y,mean_Bperm_z,mean_muperm])

X = np.zeros((n_unknown*2+1, n_unknown))
X[0,:] = mean_X
W = np.zeros((n_unknown*2+1,))
W[0] = kappa/(kappa + n_unknown)
for i in range(n_unknown):
    X[i+1,:] = mean_X + np.sqrt(kappa + n_unknown) * np.sqrt(covvar_X)[:,i]
    X[i+1+n_unknown,:] = mean_X - np.sqrt(kappa + n_unknown) * np.sqrt(covvar_X)[:,i]
    W[i+1] = 1/(2*(kappa + n_unknown))
    W[i+1+n_unknown] = 1/(2*(kappa + n_unknown))

B_background_samples = X[:,:3]
B_perm_samples = X[:,4:-1]
```

We now setup our orthogonal, or non-orthogonal basis. Furthermore import the magnetic fields produced per μ_r, for each background field direction. For example, let $H_{\mathbf{x},\mathbf{y}}(\mathbf{r}_i, \mu_r)$ be the magnetic field in the $\mathbf{x}$-direction, caused by a magnetic field of 1 T in the $\mathbf{y}$-direction applied to an object with relative magnetic permeability μ_r, measured at the location $\mathbf{r}_i$, then we have:

$$\text{H\_points\_samples} = \begin{bmatrix} H_{\mathbf{x},\mathbf{x}}(\mathbf{r}_1,\mu_r) & H_{\mathbf{y},\mathbf{x}}(\mathbf{r}_1,\mu_r) & H_{\mathbf{z},\mathbf{x}}(\mathbf{r}_1,\mu_r) & H_{\mathbf{x},\mathbf{x}}(\mathbf{r}_2,\mu_r) & \ldots H_{\mathbf{z},\mathbf{x}}(\mathbf{r}_n,\mu_r) \\ H_{\mathbf{x},\mathbf{y}}(\mathbf{r}_1,\mu_r) & H_{\mathbf{y},\mathbf{y}}(\mathbf{r}_1,\mu_r) & H_{\mathbf{z},\mathbf{y}}(\mathbf{r}_1,\mu_r) & H_{\mathbf{x},\mathbf{y}}(\mathbf{r}_2,\mu_r) & \ldots H_{\mathbf{z},\mathbf{y}}(\mathbf{r}_n,\mu_r) \\ H_{\mathbf{x},\mathbf{z}}(\mathbf{r}_1,\mu_r) & H_{\mathbf{y},\mathbf{z}}(\mathbf{r}_1,\mu_r) & H_{\mathbf{z},\mathbf{z}}(\mathbf{r}_1,\mu_r) & H_{\mathbf{x},\mathbf{z}}(\mathbf{r}_2,\mu_r) & \ldots H_{\mathbf{z},\mathbf{z}}(\mathbf{r}_n,\mu_r) \end{bmatrix} \tag{C.1}$$

We take the inner product with the background fields $\mathbf{B}_0$ and $\mathbf{B}_{0,\text{perm}}$ per sample, to create the sample measurement vectors. Furthermore we import or build the matrix `A_samples` that can be inverted to find the c_{km} vector, using the function `basis.construct_A`.

```
H_points_samples = np.zeros([H_points_samples_mu_mean.shape[0], n_unknown*2+1])

H_points_samples[:,:4] = np.dot(H_points_samples_mu_mean,B_background_samples[:4,:].T)/mu_0
H_points_samples[:,n_unknown+1:n_unknown+4] = np.dot(H_points_samples_mu_mean,
    B_background_samples[n_unknown+1:n_unknown+4,:].T)/mu_0
H_points_samples[:,5:n_unknown] = np.dot(H_points_samples_mu_mean,B_perm_samples[5:n_unknown
    ,:].T)/mu_0
H_points_samples[:,n_unknown+5:n_unknown+8] = np.dot(H_points_samples_mu_mean,B_perm_samples[
    n_unknown+5:n_unknown+8,:].T)/mu_0
H_points_samples[:,8] = np.dot(H_points_samples_mu_high,B_perm_samples[8,:].T)/mu_0
H_points_samples[:,-1] = np.dot(H_points_samples_mu_low,B_perm_samples[-1,:].T)/mu_0

n_sensors_measure_samples = points_samples.shape[0]
b_samples = np.zeros((3*n_sensors_measure_samples,n_unknown*2+1))

for i in range(n_unknown*2+1):
    H_points_sample_i = H_points_samples[:,i].reshape(-1,3)
    H_points_sample_i = H_points_sample_i + B_background_samples[i,:]/mu_0
    b_samples_i, sensor_axes_samples = main.construct_b(points_samples, H_points_sample_i,
        b_long_samples)
    b_samples[:,i] = b_samples_i

c_km_samples = np.zeros((k_max*(k_max+2)+3, n_unknown*2+1))
for i in range(n_unknown*2+1):
    c_km_samples[:,i] = np.linalg.lstsq(A_samples, b_samples[:,i], rcond=None)[0]

mean_ckm = np.zeros(c_km_samples[:,0].shape)
cov_mat_ckm = np.zeros((mean_ckm.shape[0], mean_ckm.shape[0]))

for i in range(n_unknown*2+1):
    mean_ckm += W[i]*c_km_samples[:,i]
for i in range(n_unknown*2+1):
    cov_mat_ckm += W[i]*np.outer(c_km_samples[:,i] - mean_ckm, c_km_samples[:,i] - mean_ckm)
```

C.7. Applying Bayesian Inference and PCA

```
def compute_c_km_Bayes(A, b, sigma, cov_mat_ckm, mean_ckm):
    """
    Compute the Bayesian estimate of the coefficient vector c_km.

    This function solves a linear inverse problem using a Gaussian prior
    on the coefficients. It combines the data likelihood and prior information
    to compute the posterior mean of c_km.

    Parameters
    ----------
    A : ndarray
        Forward matrix relating the coefficients to observations.
    b : ndarray
        Observed data vector.
    sigma : float
        Standard deviation of the observational noise.
    cov_mat_ckm : ndarray
        Prior covariance matrix of the coefficient vector c_km.
    mean_ckm : ndarray
        Prior mean vector of the coefficient vector c_km.

    Returns
    -------
    c_km : ndarray
        Posterior mean estimate of the coefficient vector.
    """
    cov_mat_b = sigma**2*np.eye(b.shape[0])
    cov_mat_b_inv = np.linalg.inv(cov_mat_b)
    M = A.T @ cov_mat_b_inv @ A + np.linalg.inv(cov_mat_ckm)
    rhs = A.T @ cov_mat_b_inv @ b + np.linalg.inv(cov_mat_ckm) @ mean_ckm
```

```python
    c_km = np.linalg.solve(M,rhs)
    return c_km
```

```python
def PCA(cov_mat_ckm, rank_extra=0):
    """
    Perform Principal Component Analysis (PCA) on a covariance matrix.

    This function computes the eigenvalue decomposition of the covariance
    matrix and selects a reduced set of principal components based on the
    matrix rank plus an optional extension. The dominant eigenvectors define
    a lower-dimensional subspace used for dimensionality reduction.

    Parameters
    ----------
    cov_mat_ckm : ndarray
        Covariance matrix of the coefficient vector c_km.
    rank_extra : int
        Additional number of components to include beyond the numerical rank
        of the covariance matrix.

    Returns
    -------
    V0 : ndarray
        Matrix whose columns are the selected principal eigenvectors
        (dominant subspace).
    V1 : ndarray
        Matrix whose columns span the remaining (discarded) subspace.
    S0 : ndarray
        Array of selected eigenvalues corresponding to V0.
    """
    eigvals, eigvecs = np.linalg.eigh(cov_mat_ckm)
    idx = np.argsort(eigvals)[::-1]
    eigvals = eigvals[idx]
    eigvecs = eigvecs[:, idx]
    rank = np.linalg.matrix_rank(cov_mat_ckm)
    rank +=rank_extra
    V0 = eigvecs[:, :rank]
    V1 = eigvecs[:, rank:]
    S0 = eigvals[:rank]
    return V0, V1, S0

def compute_ckm_Bayes_PCA(A, b, V0, V1, S0, cov_mat_b, mean_ckm):
    """
    Compute the Bayesian estimate of c_km using a PCA-reduced subspace.

    This function solves the Bayesian inverse problem in a reduced-dimensional
    space defined by the principal components (V0). It improves computational
    efficiency by projecting the problem onto the dominant eigen-subspace of
    the prior covariance.

    Parameters
    ----------
    A : ndarray
        Design (or forward) matrix relating coefficients to observations.
    b : ndarray
        Observed data vector.
    V0 : ndarray
        Matrix of dominant eigenvectors (reduced basis).
    V1 : ndarray
        Matrix of discarded eigenvectors (not used in computation but returned
        by PCA for completeness).
    S0 : ndarray
        Eigenvalues corresponding to V0 (used for prior precision in reduced space).
    cov_mat_b : ndarray
        Covariance matrix of the observational noise.
    mean_ckm : ndarray
        Prior mean vector of the coefficient vector c_km.

    Returns
    -------
    c_km_z : ndarray
```

```
        Posterior mean estimate of c_km reconstructed from the reduced subspace.
    """
    A_z = A @ V0
    cov_mat_b_inv = np.linalg.inv(cov_mat_b)
    M_z = A_z.T @ cov_mat_b_inv @ A_z + np.diag(1.0 / S0)
    b_z = b - A @ mean_ckm
    rhs_z = A_z.T @ cov_mat_b_inv @ b_z
    z_map = np.linalg.solve(M_z, rhs_z)
    c_km_z = V0 @ z_map + mean_ckm
    return c_km_z
```